SEPTEMBER 2019

M.Sc. in Mechanical Engineering

SİNAN TURHAN

REPUBLIC OF TURKEY

GAZİANTEP UNIVERSITY

GRADUATE SCHOOL OF NATURAL & APPLIED SCIENCES

NUMERICAL SIMULATIONS OF EXPERIMENTAL SETUPS USED FOR TESTING RECENT GLAUCOMA DRAINAGE DEVICES ON THE CONTROL OF INTRAOCULAR PRESSURE ABNORMALITIES

M.Sc. THESIS

IN

MECHANICAL ENGINEERING

BY

SİNAN TURHAN

SEPTEMBER 2019

NUMERICAL SIMULATIONS OF EXPERIMENTAL SETUPS USED FOR TESTING RECENT GLAUCOMA DRAINAGE DEVICES ON THE CONTROL OF INTRAOCULAR PRESSURE ABNORMALITIES

M.Sc. Thesis

in

Mechanical Engineering

Gaziantep University

Supervisor

Prof. Dr. Ahmet İhsan KUTLAR

Co-Supervisor

Asst. Prof. Dr. Emre KARA

by

Sinan TURHAN

September 2019

REPUBLIC OF TURKEY
GAZİANTEP UNIVERSITY
GRADUATE SCHOOL OF NATURAL & APPLIED SCIENCES
MECHANICAL ENGINEERING

Name of the Thesis : Numerical Simulations of Experimental Setups Used for Testing Recent Glaucoma Drainage Devices on the Control of Intraocular Pressure Abnormalities

Name of the Student : Sinan TURHAN

Exam Date : 06.09.2019

Approval of the Graduate School of Natural and Applied Sciences

Prof. Dr. A. Necmeddin YAZICI
Director

I certify that this thesis satisfies all the requirements as a thesis for the degree of Master of Science.

Prof. Dr. Melda ÇARPINLIOĞLU
Head of Department

This is to certify that we have read this thesis and that in our consensus opinion it is fully adequate, in scope and quality, as a thesis for the degree of Master of Science.

Asst. Prof. Dr. Emre KARA
Co-Supervisor

Prof. Dr. Ahmet İhsan KUTLAR
Supervisor

Examining Committee Members:	Signature
Prof. Dr. Ahmet İhsan KUTLAR	……..
Asst. Prof. Dr. Fuat YILMAZ	……..
Asst. Prof. Dr. Mustafa Murat YAVUZ	……..

Thereby declare that all information in this document has been obtained and presented in accordance with academic rules and ethical conduct. I also declare that, as required by these rules and conduct, I have fully cited and referenced all material and results that are not original to this work.

Sinan TURHAN

ABSTRACT

NUMERICAL SIMULATIONS OF EXPERIMENTAL SETUPS USED FOR TESTING RECENT GLAUCOMA DRAINAGE DEVICES ON THE CONTROL OF INTRAOCULAR PRESSURE ABNORMALITIES

TURHAN, Sinan
M.Sc. in Mechanical Engineering
Supervisor: Prof. Dr. Ahmet İhsan KUTLAR
Co-supervisor: Asst. Prof. Dr. Emre KARA
September 2019
110 pages

Commonly used glaucoma drainage devices (GDDs) have many disadvantageous circumstances especially in postoperative period. Researchers have investigated glaucoma drainage devices by in-vivo, ex-vivo and in-vitro experimental setups and tried to overcome their disadvantages. In this study, one branch of them, in-vitro experimental setups currently used in testing of GDDs are surveyed. Their disadvantages are discussed. As a result, a new innovative experimental setup is introduced. Then, its numerical simulations are performed using porous media approach in ANSYS Fluent for Ahmed and Molteno implants. Pressure losses of AGV at flow rates 2.5, 5, 10, 20, 25 µl/min are found as 693, 999.6, 1142.8, 1261.8, 1406.3, 1431.5 Pa respectively. Pressure Losses of single plate Molteno device at flow rates 9.1, 21.6, 34.7, 47, 60 are found as 669.6, 1326.3, 2014.9, 2658.2, 3338.5 Pa. Pressure Losses for double plate Molteno device at flow rates 5, 10, 15, 20, 25 µl/min are found as 547.6, 691.4, 835.4, 979.6, 1124 Pa. Geometric models of XEN and ExPress implants are simulated. Pressure loss of XEN implant at physiologic flow rate is found as 12.26 mmHg. Pressure losses of ExPress implant at flow rates 664, 1180, 1575, 1928, 2241 are found as 575.4, 1246.3, 1898, 2582.4, 3265.5. Lastly, CFD results are compared with experimental results in literature.

Key Words: Glaucoma Drainage Device, CFD Analysis, Microfluidic Experimental Setup, Porous Media

ÖZET

GÖZ İÇİ BASINÇ ANORMALLİKLERİNİN KONTROLÜ İÇİN GÜNCEL GLOKOM DRENAJ İMPLANTLARINI TEST İÇİN KULLANILAN DENEY DÜZENEKLERİNİN SAYISAL BENZETİMLERİ

TURHAN, Sinan
Yüksek Lisans Tezi, Makine Mühendisliği
Danışman: Prof. Dr. Ahmet İhsan KUTLAR
İkinci Danışman: Dr. Öğr. Üyesi Emre KARA
Eylül 2019
110 sayfa

Yaygın olarak kullanılan glokom drenaj implantları (GDİ) özellikle ameliyat sonrası koşullarda birçok dezavantaja sahiptir. Araştırmacılar glokom drenaj implantlarının dezavantajlarını in-vivo, ex-vivo ve in-vitro deney düzeneklerinde inceleyip bunların üstesinden gelmeye çalışmışlardır. Bu çalışmada, sadece GDİ'lerin sınanmasında kullanılan in-vitro deney düzenekleri incelenmiş ve eksikleri tartışılmıştır. Bunun sonucunda yenilikçi bir deney düzeneği sunulmuştur. Ahmed ve Molteno implantlarının sayısal benzetimleri ANSYS Fluent'de bulunan poroz ortam modeli kullanılarak gerçekleştirilmiştir. AGV için 2.5, 5, 10, 20, 25 µl/dk debilerindeki basınç kayıpları 693, 999.6, 1142.8, 1261.8, 1406.3, 1431.5 Pa olarak bulunmuştur. Tek plakalı Molteno cihazı için 9.1, 21.6, 34.7, 47, 60 debilerindeki basınç kayıpları 669.6, 1326.3, 2014.9, 2658.2, 3338.5 Pa olarak bulunmuştur. Çift plakalı molteno cihazı için 5, 10, 15, 20, 25 µl/dk debilerindeki basınç kayıpları 547.6, 691.4, 835.4, 979.6, 1124 Pa olarak bulunmuştur. XEN ve ExPress implantları geometrik olarak simüle edilmiştir. XEN implant için fizyolojik debideki basınç kaybı 12.26 mmHg olarak bulunmuştur. ExPress implant için 664, 1180, 1575, 1928, 2241 µl/dk debilerindeki basınç kayıpları 575.4, 1246.3, 1898, 2582.4, 3265.5 Pa olarak bulunmuştur. HAD sonuçları literatürdeki deneysel verilerle karşılaştırılmıştır.

Anahtar Kelimeler: Glokom Drenaj İmplantı, HAD Analizi, Mikroakışkan Test Düzeneği, Poroz Ortam

"Dedicated to my family"

ACKNOWLEDGEMENTS

I would like to thank my supervisor, Prof. Dr. Ahmet İhsan Kutlar for his guidance and support throughout the study. I am thankful for his encouragement and motivation.

I would like to express my gratitude to my co-supervisor, Asst. Prof. Dr. Emre Kara for his great support, encouragements and advices. This thesis would not have taken the shape and progressed without his support.

I also wish to express my sincere appreciation to Prof. Dr. Melda Çarpınlıoğlu, Prof. Dr. M. Yaşar Gündoğdu and Asst. Prof. Dr. Fuat Yılmaz for their support and guidance to improve my skills in the field of fluid mechanics during my study at the Gaziantep University.

I would like to Prof. Dr. Kıvanç Güngör for his medical guidance.

I would like to express my love and gratitude to my family for their support, always best wishes.

This study is supported by the Scientific and Technological Research Council of Turkey (TÜBİTAK) [Grant number 117M971].

TABLE OF CONTENTS

Page

LIST OF TABLES

Page

LIST OF FIGURES

Page

LIST OF SYMBOLS

$\mathbf{C_2}$	Inertial resistance factor
d	Diameter of pipe, mm
$\mathbf{D_h}$	Hydraulic diameter, mm
$\mathbf{h_e}$	Entrance head loss, m
$\mathbf{h_{sc}}$	Head loss due to sudden contraction, m
$\mathbf{h_{se}}$	Head loss due to sudden enlargement, m
K	Loss coefficient
Kn	Knudsen number
l	Length of pipe, mm
$\mathbf{L_{FD}}$	Entrance length, mm
P	Pressure
ΔP	Pressure drop
$\mathbf{\Delta P_e}$	Entrance pressure loss, Pa
Q	Flow rate
r	Radius of pipe, mm
R	Flow resistance
Re	Reynolds number
$\mathbf{S_i}$	Source term for X, Y, Z momentum equation
$\bar{\mathbf{U}}$	Mean velocity of aqueous humor in the pipe, mm/s
$\|\boldsymbol{v}\|$	Magnitude of velocity

Greek Letters

λ	Mean free path
μ	Dynamic viscosity of aqueous humour, kg/m.s
π	Pi number
ρ	Density of aqueous humour, kg/m^3

LIST OF ABBREVIATIONS

AC	Anterior Chamber
AGV	Ahmed Glaucoma Valve
AH	Aqueous Humour
BSS	Balanced Saline Solution
CFD	Computational Fluid Dynamics
ePTFE	Polytetrafluoroethylene
GDD	Glaucoma Drainage Device
GDDA	Glaucoma Drainage Device For Human
GDDH	Glaucoma Drainage Device For Animal
IOP	Intraocular Pressure
mAGV	Modified Ahmed Glaucoma Valve
PLA	Polylactic Acid
PLGA	Poly(lactic-co-glycolic acid)
PMDS	Polydimethylsiloxane
PP	Polypropylene
PBS	Phosphate Buffered Saline
PUR	Polyurethane
SIL	Silicone
µPIV	Micro Particle Image Velocimetry
UDF	User Defined Function
US FDA	United States Food and Drug Administration

CHAPTER I

INTRODUCTION

1.1 A Short Brief of Eye Anatomy and Glaucoma

Glaucoma is an eye disease in which optical nerve is damaged due to abnormal rise of intraocular pressure (IOP) by time. According to World Health Organization, Glaucoma is the second common reason for blindness. In a healthy eye, average IOP is 2000 Pa varying between 1600 and 2666 Pa. However it may increase up to 8000 Pa in glaucomatous eyes [1].

The eye mainly consists of three chambers. These are anterior chamber, posterior chamber and vitreous chamber (or vitreous body) in Figure 1.1.

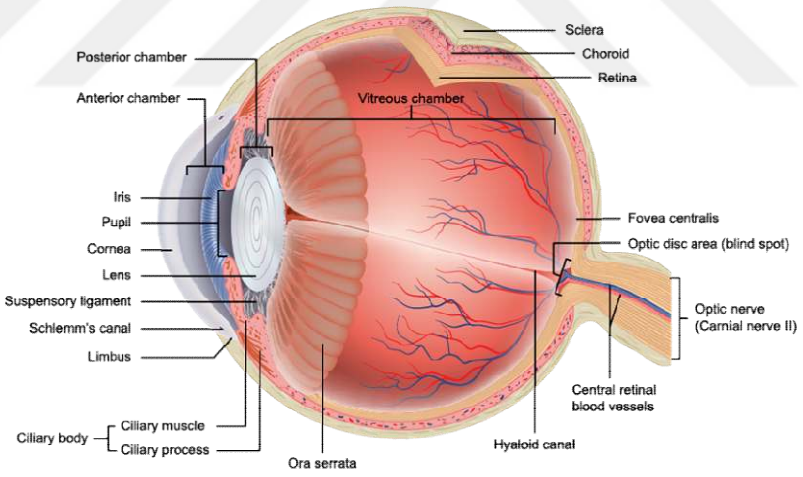

Figure 1.1 Eye anatomy [2].

The posterior and anterior chambers are filled with transperent liquid called as "aqueous humor". Aquous humour supplies nutrients for the cells of lens and carries away metabolic wastes. The physical properties of aqueous humour are very close to those of water. Aqueous humor is produced by ciliary body at flowrate 2-3 µl/min. Then, it flows from posterior chamber through pupil into anterior chamber. When AH flows into AC, it is drained passing through the porous tissue called as the

trabecular meshwork. Then, AH goes to Schlemm's canal. Eventually, Schlemm's canal delivers it into the episcleral blood vessels via aqueous veins.

In most types of glaucoma, eye's drainage system is clogged so the AH cannot be drained. When the fluid is accumulated in AC, it causes abnormal pressure rising and damages optical nerves.

1.2 An Overview on Glaucoma Drainage Devices

IOP can be lowered by some methods such as; surgery (laser treatment, trabeculectomy etc.), medical therapy, and glaucoma drainage devices (GDD). Although none of these methods gives definite results, GDDs are more preferable due to high success rates depending on design developments in the last decade. First successful GDD in history was introduced by Molteno in 1963 [3]. Molteno's implant is comprised of a silicon tube and a plate end of the propylene tube. The tube shunts and discharges the flow by pressure differences on each side of plate. The other non-valved GDD is Baerveldt's device. Baerveldt's implant is comprised of a silicone rubber tube and barium impregnated silicone end plate on which fenestrations allow fibrous bands to diminish bleb profile. After implantation of non-valved GDDs, hypotony occurs (IOP< 5 mmHg) because the bleb formation takes some time postoperatively. To prevent postoperative hypotony, valved GDDs were improved such as Krupin slit valve and Ahmed Glaucoma Valve (AGV). Krupin's valve consists of an anterior chamber tube and a slit valve which regulates the aqueous humour (AH) flow. AGV has the valve at the end of the plate to restrict the flow until the flow pressure is bounded between 8-12 mmHg [4]. In 2002, US FDA offered a new type of GDD. This GDD is called as ExPress implant. It's comprised of a stainless steel, non-valved tube with a disc-like flange. The disk flange end implanted to subconjuctival space and its spur end at anterior chamber. There two types of this implant. These are P50 and P200 models. These GDD's used to be implanted directly into eyes but it caused some complications like hypotony, conjugal erosion, endophthalmitis etc. Because of these complications, it was started to be used with a scleral flap just as trabeculectomy, and finally these complications was achieved considerably. In 2015, researchers improved XEN implant by using Hagen-Poiseuille formula to reduce IOP without causing hypotony. It has straight cylindrical shape with lumen at its centre. The lumen diameter is 45 μm and its

length is 6 mm. In the scope of this thesis, AGV, Molteno, XEN and ExPress implants will be examined numerically with a new experimental setup using Computational Fluid Dynamics (CFD) tools. The properties of mentioned GDDs are summarized in Table 1.1.

Table 1.1 Currently used GDDs and their properties [5-8]

GDD	SHAPE	MATERIAL	ADVANTAGES	DISADVANTAGES
MOLTENO	Round, dog dish shaped	Propylene	Simple Tube&Plate couple	Uncontrolled flow mechanism
				Small reduction in IOP
				Hypotony
BAERVELDT	Kidney shaped	Silicone	Easy to modify	Micromotion
			Flexible	Bulky device
			Low profile	Hypotony
			Fenestrations	Diplopia
				Scar deformation
KRUPIN	Oval	Silicone	Unidirectional slit valve	Bulky device
			Minimal contact with muscles	Valve malfunction
			Flexible	Small surface area
				High profile
AHMED	Pearl shaped	PP&Silicone	Simple valve	Valve malfunction
			Venturi flow	Micromotion
			Easy to implant	Inflammation
			Minimal contact with muscles	High profile
ExPress	Non-valved tube with a disk flange	Stainless Steel	Ease of insertion	Hypotony
			Elimination of iridectomy and sclerostomy	Erosion Needs scleral flap
XEN	Straight tube shaped	Silicone	Simple Tube	Erosion
			Prevents hypotony	Implant migration

CHAPTER II

EXPERIMENTAL STUDIES IN LITERATURE

In 2011, Moon et al. [9] designed a new GDD comprised of three layers and a check valve. They mainly used PMDS (polydimethylsiloxane) material instead of propylene which is more flammatory than PMDS. Bottom layer is the fluidic channel in which fluid flows firstly. Valve seat and membrane act as check valve mechanisms when internal pressure is greater than external pressure, so that membrane is deformed and the flow initiates. They produced two types of GDDs; one is for humans (GDDH) and the other one is for animals (GDDA). They determined cracking pressure of GDDH and GDDA as 20 mmHg and 10-15 mmHg respectively. They examined it via subsequent experimental setup in Figure 2.1.

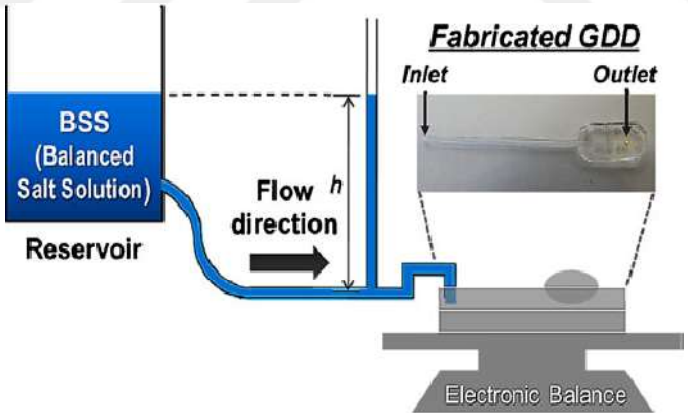

Figure 2.1 The experimental setup for GDDH and GDDA [9].

Because of the symmetry, they made their analysis in 2D and then they converted 2D flowrates to 3D for minimizing computational time. According to test results, mean value and standard deviation of cracking pressure was 18.33±0.66 mmHg (2444±87.79 Pa) which was close to prescribed value of 20 mmHg (2666 Pa) by 5 percent. In addition, they tested whether there were any flowrate when internal

pressure is smaller than external pressure. They applied external pressure at valve orifice 22.5, 45, 67.5 and over 75 mmHg, respectively.

According to test results, GDDH showed good repeatability and consistent cracking pressure. GDDH showed nearly zero flowrates at 17.63 mmHg (2350 Pa) and 8.1±0.2 µl/min at 30 mmHg (4000 Pa). Finally, they repeated procedures for GDDA and applied it on rabbits for in-vivo tests. The cracking pressure for GDDA was found to be 12.46 mmHg (1656 Pa) within the range of prescribed values 10-15 mmHg in-vitro. During in-vivo tests, GDDAs were implanted in rabbits suffered from IOP over 30 mmHg. At the end of these tests, there were shown regulation in IOP entire follow-up period 12 weeks. Hypotony was not encountered under 10 mmHg.

In 2011, Char DeCroos et al. [10] compared classical AGV with PRIME-AGV. They developed a prototype AGV enclosed in a porous membrane of ePTFE (Polytetrafluoroethylene) which provides to develop more vascularized and permeable capsule. They established an experimental setup which consists of a syringe pump, pressure transducer (±0.65 mmHg) and a GDD in saline or 2.5% gelatin in Figure 2.2. They also connected a mercury manometer to calibrate the system.

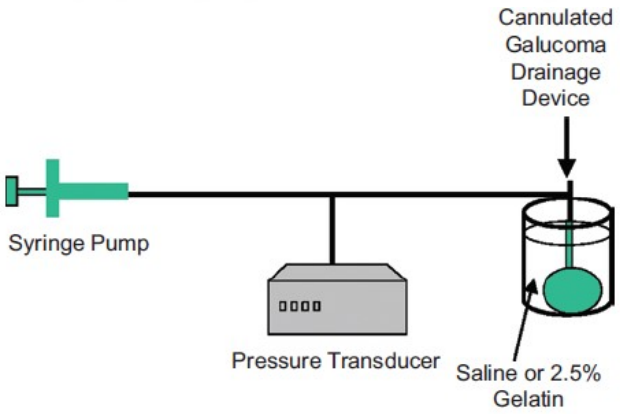

Figure 2.2 The experimental setup for AGV and PRIME-AGV [10].

Firstly, they tested seven AGV and seven PRIME-AGV in saline at variable flow rates (at 1, 2, 5, 10, 20 and 50 µl/min, and $p<0.05$). Then, seven AGVs and seven PRIME-AGVs were tested in 2.5% gelatin solution at the same flow rates. They concluded that AGV with porous membrane added resistance which decreased with increasing flow. They planned to investigate combined effects of the resistance

added by the porous membrane while decreasing the resistance due to a thinner, more vascular capsule.

In 2012, Maleki et al. [11] improved a biodegradable truncated-cone shaped plug filter to prevent postoperative hypotony in nonvalved GDDs. According to their hypothesis, plug filter inserted in a non-valved GDD that attenuates the AH flow and prevents postoperative hypotony until bleb formation progress. When the bleb formation progresses, the plug filter degrades. They used Hagen-Poiseuille equation in plug filter design. They produced two plug filters with different materials; PLGA (with properties 50/50 mole ratio; 42-48 ˚C glass transition temperature; and 3-4 weeks degradation time) and PLA (with properties 100/0 mole ratio; 56-60 ˚C Glass transition temperature; and 5-6 months degradation time), respectively. Glass transition/degradation time of polymers was adjusted by changing their molecular weight and end groups. They coated PLGA with a biocompatible polymer SU-8 to overcome low glass temperature. They inserted it in a Baerveldt GDD and tested it. Their experimental setup consisted of a syringe pump, pressure sensor and data acquisition system as in Figure 2.3.

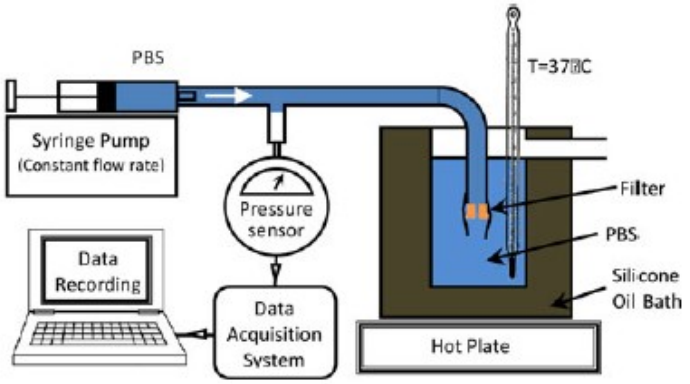

Figure 2.3 The experimental setup for Baerveldt GDD [11].

They used PBS (phosphate buffered saline) solution in 37 ˚C oil bath to imitate the AH. Then, they pumped PBS into the GDD with plug filter at flowrate 2-3 µl/min and read the pressure from monitor. Firstly, they tested whether plug filter to slide in case of clogging. There wasn't seen any sliding with plug filter. They tested PLGA with two holes 40 and 85 µm diameters, respectively, but they could not attain desired results due to large hole size. They attained desired pressures (15-20 mmHg) at 30-40 µl/min. Next, they used plug filters in series. As expected, pressure drop increased a bit. According to these experiments, they determined effective hole

diameter as 44 μm. Then, they pumped PBS at 37 ˚C at flow rate 3 μl/min and observed back pressure of PLGA with two holes. It was seen that pressure was highly increasing after some time later. They made various experiments with different type of cone to overcome this problem. As the result, they succeeded in regulating the pressure more than 15 days with PLA. PLGA filters coated by SU-8 or UV-curing adhesive regulated the pressure up to 45 day that was sufficient for bleb formation.

In 2012, Siewert et al. [12] developed a valved GDD. They designed the GDD to provide AH flow from anterior chamber to suprachoroidal space as a distinct flow pathway from novel GDDs. Firstly they adjust their opening pressure and produced it from two different materials (PUR and SIL) with different wall thicknesses and valve lengths. They built an experimental setup to examine flow characteristics through the developed GDD as in Figure 2.4.

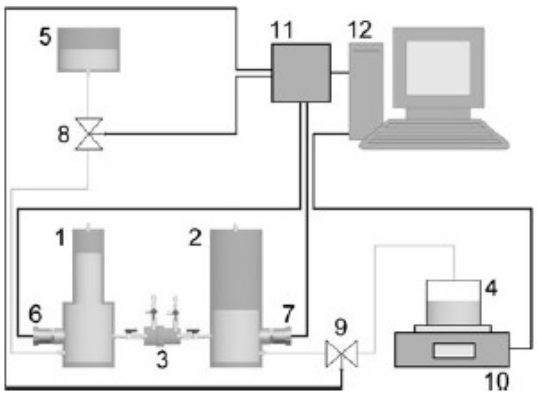

Figure 2.4 The experimental setup [12].

Their experimental setup was different from currently used syringe pump setups. Firstly, their pressure differences between in and out flow of the chamber (3), in which GDD was tested, was constant due to two hydrostatic heads in the pressure chambers (1 and 2). Fluid was flowing from (1) through (3) into (2) and finally into the fluid reservoir (4). The fluid was continuously weighted by a scale (10). Measurements were made by two sensors (6) and (7) in combination with two magnetic valves (8, 9). The valves were manipulating pressure as refilling the chambers from reservoir (5), the valves were opened at when pressure in (1) decreases and pressure in (2) increases. For data recording and system controlling, a personal computer (12) with analog to digital converter (11) was used. They found

difference between opening and closing pressure of SIL material in the light of results. They thought that it was due to an interaction of the valve with the current flow and could have been expected for micro-mechanical PUR valves as well.

In 2012, Schmidt et al. [13] tested a GDD designed by Siewert et al. (in 2010) [14] with a different experimental setup. They designed micro-Particle Image Velocimetry (µPIV) setup to characterize the flow mechanics of the valve. Their experimental setup is illustrated in Figure 2.5.

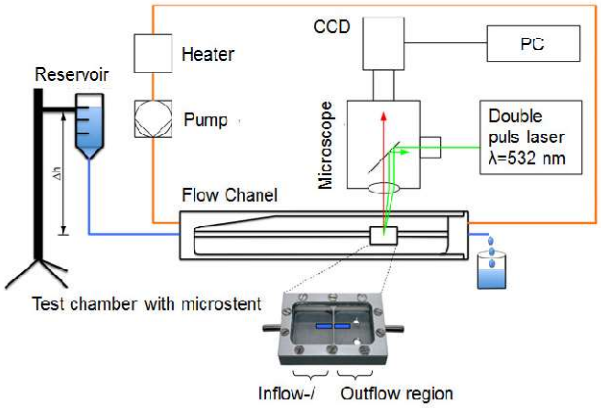

Figure 2.5 µPIV setup [13].

Before the experiment, they matched refractivity of the test fluid (pure water and 1.5 µm rhodamine red-dyed tracer particles) to silicone by potassium thiocyanate. They measured the velocity at valve section at variable pressures differences (1, 4, 16 mmHg). The flow velocity ranged from 10-6 to 2.5x10-2 m/s for different pressures according to experimental result. When they compared these results with detection of valve opening pressure by volumetric flow rate and pressure difference, they attained a good correlation. They could not compare mean flow velocity and volume flow quantitatively based on the presented µPIV because flow velocity measurement was performed in only one direction. They assumed that it was symmetric due to the geometry of the valve. Furthermore, their flowrate measurements inside the microstent failed due to accumulation of tracer particles on the implant surface. Consequently, they inferred that µPIV provided qualitative and quantitative information about current fields and would be a powerful tool for development and evaluation of micro-mechanical valves. And they considered coating the microstent surface including inner lumen with hydrophilic or hydrophobic materials to prevent tracer accumulation and design new GDDs for future work.

In 2013, Paschalis et al. [15] designed a ferrovalve in which ferrofluidics prevented early hypotony. When the ferrofluid was in magnetic field, it acted as a valve and blocked the flow. They used two magnets in this design. First magnet was used for fixation of ferrofluid and the second magnet was used for adjusting opening pressure of the valve. If the second magnet was closer, it's opening pressure was higher and vice-versa. When pressure exceeds opening pressure, flow begins. They tested their design and compared with AGV. The experimental setup consisted of "distilled H_2O" (dH_2O) reservoir and a manometer. Different test pressures were adjusted by changing the height of dH_2O reservoir. The opening and closing pressures had been calibrated as 10 mmHg and 7 mmHg respectively (with a variability ±0.5 mmHg) before the experiment. The experiment was performed at the pressures 7, 12, 16 and 21 mmHg over a period of 30 days. In consequence of the experiment, it was seen that the flow/pressure response of the valve showed increase of flow at higher pressures (1.8 µl/min at 12 mmHg; 4.3 µl/min at 16 mmHg; 7.6 µl/min at 21 mmHg with variations ±0.2 µl/min). They achieved 12.5 mmHg pressure at the AH production rate in normal eyes (~2.5 µl/min). They measured no closing pressure at the outlet tip of the AGV because AGV requires subconjuctival implantation to achieve closing pressure. Because of this result, AGV should not be used extraocularly. On the other hand, they measured 3 mmHg differences between opening and closing pressures in ferrofluidic valve. The ferrovalve gave promising results in-vivo tests.

In 2013, Quang Minh Luong et al. [16] modified an AGV to gain stable IOP for attenuation of the hypertensive phase after capsule formation while avoiding postoperative hypotony. They produced a valve from biodegradable polymer poly (L-lactide-co –ε-caprolactone: PLC 70/30). They used classical syringe pump based experimental setup as it is seen in Figure 2.6 to compare normal AGV and modified AGV (mAGV). They tested three mAGV and three AGV and averaged their data, compared their starting and ending pressures (pressures before and end of the degradation time average 7 weeks). According to their results, average starting and ending pressures of AGV was 13.3±1.5 mmHg and 10.7±1 mmHg, respectively. Average starting and ending pressures of mAGV was 10.7±1.8 mmHg and 1.9±1.8 mmHg.

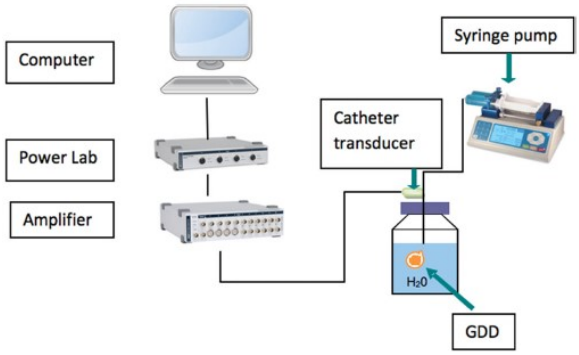

Figure 2.6 The experimental setup for AGV and mAGV [16].

In 2014, Villamarin et al. [17] designed an adjustable glaucoma drainage device. This device has a mechanism comprised of a mechanical disk around a shaft. The mechanical disk position is adjusted by the control unit (CU) which contains a compass at the one end. When disk angle becomes smaller, flow resistance becomes greater. This mechanism provides non-invasive adjusting IOP after implanting. They examined this GDD by in-vitro and ex-vivo experimental setups. In in-vitro setup, they used syringe pump and electronic manometer setup. They used saline solution to imitate AH at a physiological rate of 2 µl/min. They measured pressure at inlet and outlet and found a relationship between pressure values and angular position of the disk. As a result, when the disk position was adjusted correctly, the GDDs prevented hypotony.

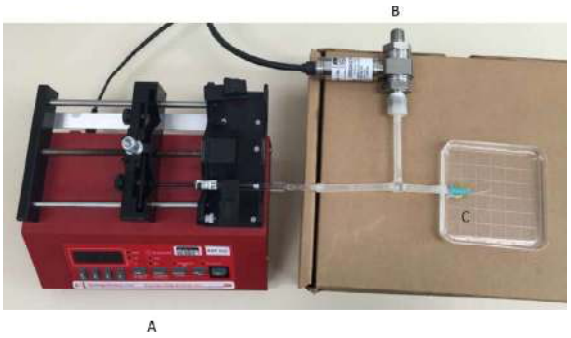

Figure 2.7 The experimental setup for XEN implant [6].

In 2015, Sheybani et al. [6] tested a non-valved GDD, XEN implant, and compared it with Ex-Press and Baerveldt implants. They measured XEN at 5 mmHg initial pressure and 1.2 µl/min flow rate before the experiment. They used syringe pump experimental setup in Figure 2.7. They used distilled water at 21 ˚C whose viscosity is 0.9778 centipoise (cP) and water at 37 ˚C with 0.6904 cP. They made experiment at several flowrates: 25, 50 and 74 µl/min, respectively. They measured these devices

at high rates because the pressures were small when these devices were measured at physiologic flowrates; the measurement device read them as zero. However, they measured XEN implant at nearly physiologic flowrates (1, 2, 5 and 10 µl/min) and the pressures were measured as between 6.28 to 7.85 mmHg for XEN implant thus it can prevent hypotony. According to experimental results, Baerveldt and Ex-Press implants have so low pressure values at physiologic flow rates that are why they cannot prevent hypotony.

CHAPTER III

A NEW MICROFLUIDIC EXPERIMENTAL SETUP FOR TESTING OF GDDs AND ITS MATHEMATICAL MODELLING

Various solutions in literature were offered to cure glaucoma. However, the most effective solution is to use glaucoma drainage devices. There are so many works to test of effectiveness of these devices in literature. However, all of them almost the same experimental methods (syringe pump experimental setups), which have some disadvantages like low precision, low repeatability etc. The lack of a new experimental setup which eliminates disadvantages of old setups is felt every day. Our proposal experimental setup is in Figure 3.1.

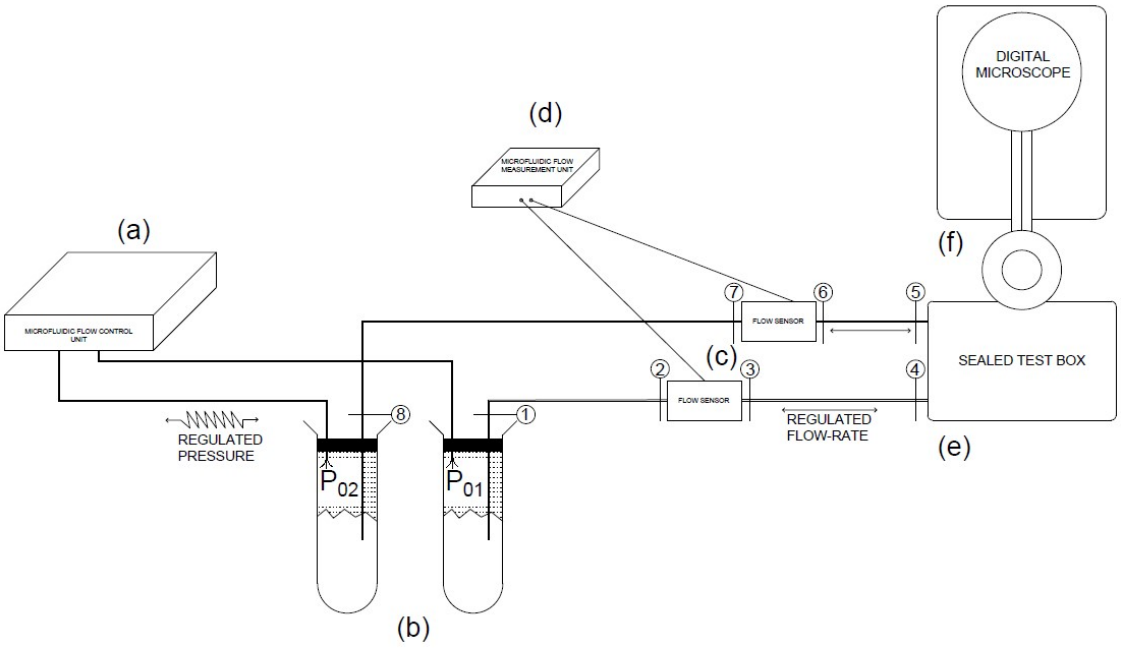

Figure 3.1 The Experimental setup. (a) Microfluidic flow control unit. (b) Reservoirs. (c) Flow sensors. (d) Microfluidic flow measurement unit. (e) Sealed test box. (f) Digital microscope.

This setup will ensure testing of any GDD in a medium which is similar to eye as in-vitro. In this setup, fluid flow is driven with gas pressure produced by microfluidic flow control unit in Figure 3.1(a). Microfluidic flow control unit sends gas into reservoirs in Figure 3.1(b), thus flow initiates. Flow sensors read the flow rate and microfluidic flow control unit regulates the outlet pressure to satisfy set flowrate.

3.1 Flow Characteristics of Microfluidic Experimental Setup

It's easily estimated which model is compatible for any microfluidic fluid flow by calculating Knudsen number. Knudsen number is the ratio of the mean free path to the hydraulic diameter.

$$Kn = \frac{\lambda}{D_h} \tag{3.1}$$

D_h: The hydraulic diameter

λ : The mean free path

Table 3.1 Flow classification according to Knudsen number. [18]

Kn Range	Range description	Recommended Models
Kn→0	Neglect of diffusion	Euler-Equations
Kn≤10^{-3}	Continuum (no-slip)	Navier-Stokes equations with no-slip boundary condition
10^{-3}≤Kn≤10^{-1}	Continuum with slip flow	Burnett equations
10^{-1}≤Kn≤10	Transition to molecular flow	Direct simulation Monte Carlo
Kn>10	Free-molecular flow	Lattice Boltzmann
Kn very large	Extreme range	Molecular Dynamics

The physical properties of aqueous humour are nearly the same those of water. The mean free path of water is $2.5x10^{-10}$ [19]. And our pipe diameter is 0.25 mm. Thus, Knudsen number becomes $1x10^{-6}$. Our Knudsen number is smaller than 10^{-3}, thereby our flow charactreristic is compatible with Navier-Stokes equations with no-slip boundary conditions.

3.1.1 Microfluidic Theory

Flowrate and pressure and microfluidic resistance are related to following equation:

$$P_1 - P_2 = R.Q \tag{3.2}$$

As seen in Figure 3.2, P_1 is the inlet pressure, P_2 is the outlet pressure, R is the resistance and Q is the flowrate in this equation. The flowrate which will differ for each applied pressure is depended on system design. Finally, necessary IOP reduction ($\Delta P = P_1 - P_2$) is desired in GDDs at physiologic flow rate.

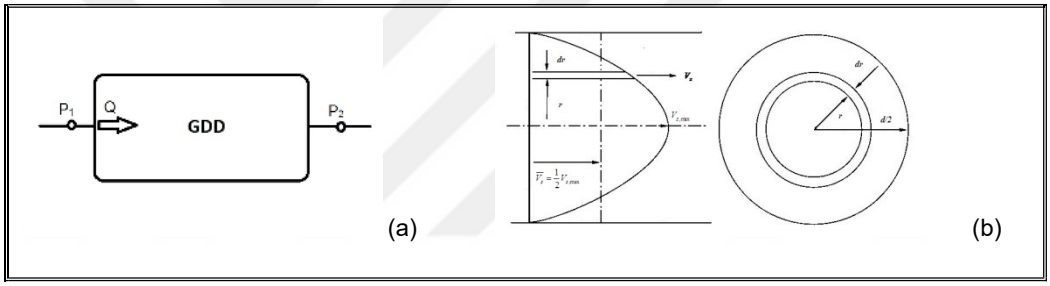

Figure 3.2 (a) Flow through GDD, (b) Viscous flow through the pipe [4]. Navier-Stokes equation for circular pipes in cylindrical coordinates [20].

$$\frac{1}{r}\frac{\partial}{\partial r}\left(r\frac{\partial V_z}{\partial r}\right)=\frac{1}{\mu}\frac{\partial p}{\partial z} \tag{3.3}$$

In this equation, P is the pressure in direction-z, V_z is the velocity in direction-z and r is the radius of the pipe. The equation is modeled for isothermal, incompressible, fully developed laminar flow in constant diameter pipe.

B.C. for maximum velocity: r=0 and $\frac{\partial V_z}{\partial r} = 0$ (3.4)

No slip B.C.: r = d/2 and $V_z = 0$ (3.5)

Thus, we get Hagen-Poiseuille equation:

$$\Delta P = \frac{128\mu l Q}{\pi d^4} \tag{3.6}$$

If we check our assumption for our setup:

Mean flow rate of aqueous humour in human body: 2-3 µl/min

Density of aqueous humour: 1000 kg/m^3

Viscosity of AH: 0.001 kg/m.s

Inside diameter of the pipe: 0.79375 mm

$$\overline{U} = \frac{Q}{A} = \frac{\frac{2.5\ \mu l}{min} x \frac{10^{-6}\ l}{1\ \mu l} x \frac{10^{-3} m^3}{1\ l} x \frac{1\ min}{60 s}}{\frac{\pi (0.00079375)^2}{4}} \tag{3.7}$$

So, $$\overline{U} = 0.0842\ mm/s \tag{3.7a}$$

Thus, we can calculate the Reynolds number;

$$Re_d = \frac{\rho V D}{\mu} \tag{3.8}$$

$$Re_d = \frac{1000 \frac{kg}{m^3} x\ 0.0842 \frac{mm}{s} x \frac{10^{-3} m}{1\ mm} x\ 0.79375\ mm \frac{10^{-3} m}{1\ mm}}{0.001 \frac{Kg}{m.s}} \tag{3.8a}$$

Thus, Re_d = 0.067 (3.8b)

Entrance length [21]:

$$\frac{L_{FD}}{d} = \frac{0.6}{1+0.035Re} + 0.056Re = 0.59 \tag{3.9}$$

Reynolds number is smaller than 2000 and the entrance length is tiny according to pipe length. So our fully developed and laminar flow assumption is correct. Moreover Reynolds number is smaller than unity. This corresponds to a specific flow regime called as creeping flow in which body forces go down, and viscous forces becomes dominant and Navier-Stokes equation becomes;

$$\mu \nabla^2 u = \nabla P \tag{3.10}$$

In this specific case, non-linear Navier-Stokes equation will have been degraded to linear equation. Velocity is merely determined by pressure distribution according to

this degraded equation. In fact, the equation is the same with equation (3.6) Hagen-Poiseuille equation for fully developed laminar flow through a circular pipe.

In following, the experimental setup will be modeled in the light of these pieces of information.

3.2 Modelling of the Experimental Setup

In this section, we try to calculate major and minor losses in the experimental setup according to Figure 3.1.

3.2.1 Losses Involved between Reservoirs and Section 1

In this section, microfluidic flow control unit sends gas into reservoir and flow initiates. Because the gas is not compressible, we can say simply that gas pressure (P_{01}) is equal to sum of total pressure in the section 1 and entrance loss in the pipe.

Entrance loss due to the pipe flow [20];

$$h_e = \mathrm{K}(\bar{u}^2/2g) \tag{3.11}$$

where,

K: loss coefficient

$$\Delta P_e = \rho g h_e = \rho K(\bar{u}^2/2) \tag{3.12}$$

where K: 0.5

$$\bar{U} = Q/A \tag{3.13}$$

Pipe diameter is, 0.79375 mm

Entrance loss: $\Delta P_e = 0.5\ x\ \frac{1000\ x\ 0.0000842^2}{2} = 1.772\ x\ 10^{-6}\ Pa$ (3.14)

3.2.2 Losses between Sections 1-2

In this part, there is only flow in a circular pipe so we basically use Hagen-Poiseuille equation (3.6);

Pipe length between sections 1-2 is 243 mm.

So,

$$= \frac{128\ x\ 0.001x\ 0.243\ x\frac{2.5\mu l 1 min 10^{-9} m^3}{min\ \ 60s\ \ \ 1\mu}}{\pi x 0.00079375^4} \tag{3.15a}$$

$$\Delta P = 1.04\ Pa \tag{3.15b}$$

3.2.3 Losses between Sections 2-3

There is flow through the flow sensor in this part. The sensor's inner diameter is 0.43 mm, and length is 52 mm. There is a sudden contraction at the entrance of the sensor and a sudden expansion at the exit of the sensor as shown in Figure 3.3.

Figure 3.3 Flow through the sensor.

From Hagen-Poiseuille;

$$= \frac{128\ x\ 0.001x\ 0.052\ x\frac{2.5\mu l 1 min 10^{-9} m^3}{min\ \ 60\ \ \ 1\mu}}{\pi x 0.00043^4} \tag{3.16}$$

$$\Delta P = 2.58\ Pa \tag{3.16a}$$

Head loss due to sudden contraction;

$$h_{sc} = \frac{\bar{u}_2^2}{2g}\left(\frac{1}{C_c} - 1\right)^2 \tag{3.17}$$

C_c is related to A_2/A_1 [20].

where,

A_1: Cross-sectional area of the pipe

A_2: Cross-sectional area of sensor

$\bar{u}_2$: Mean velocity in the sensor

$$A_1: \pi {d_1}^2/4,\ d_1 = 0.79375 \text{ mm},\ \text{ so } A_1 = 0.4948 mm^2 \tag{3.18}$$

For sensor;

$$A_2: \pi {d_2}^2/4,\ d_2 = 0.43 \text{ mm},\ \text{ so } A_2 = 0.1452 mm^2 \tag{3.19}$$

$$\text{So, } A_2/A_1 = 0.2935 \text{ and } C_c = 0.630 \tag{3.20}$$

$$\bar{u}_2 = Q / A_2 = \frac{\frac{2.5\mu l}{min}\, x\, \frac{1\, min}{60 s}\, x\, \frac{10^{-9} m^3}{1\, \mu l}}{0.1452\, mm^2\, x\, \frac{10^{-6} m^2}{1\, mm^2}} \tag{3.21}$$

$$\bar{u}_2 = 0.287 \text{ x } 10^{-3} \text{ m/s} \tag{3.21a}$$

Finally,

$$h_{sc} = 1.447 \text{x } 10^{-9} \text{ m} \tag{3.22}$$

Head loss due to sudden expansion;

$$h_{se} = \frac{\bar{u}_2^2}{2g}\left(\frac{A_2}{A_1} - 1\right)^2 \tag{3.23}$$

where:

A_1: Cross-sectional area of the sensor

A_2: Cross-sectional area of pipe

$\bar{u}_2$: Mean velocity in the pipe

$$A_1: \pi {d_1}^2/4,\ d_1 = 0.43 \text{ mm},\ \text{ so } A_1 = 0.1452 mm^2 \tag{3.24}$$

For sensor;

$$A_2: \pi {d_2}^2/4,\ d_2 = 0.79375 \text{ mm},\ \text{ so } A_2 = 0.4948 mm^2 \tag{3.25}$$

$$\bar{u}_2 = 8.42 \text{ x } 10^{-5} \text{ m/s} \tag{3.26}$$

$$\text{So, } h_{se} = 2.09 \text{ x } 10^{-9} \text{ m} \tag{3.27}$$

3.2.4 Losses between section 3-4

Here there takes place flow in a circular pipe so we basically use Hagen-Poiseuille equation (3.6).

Pipe length between section 3-4 is 203 mm.

So,

$$= \frac{128\ x\ 0.001 \quad 0.203\ x \frac{2.5\mu l 1 min 10^{-9} m^3}{min \quad 60s \quad 1\mu l}}{\pi x 0.00079375^4} \tag{3.28a}$$

$$\Delta P = 0.87\ Pa \tag{3.28b}$$

3.2.5 Losses in Glaucoma Drainage Devices

3.2.5.1 Pressure Drops in Ahmed Glaucoma Valve

Experimental pressure drops at various flowrates in AGV are summarized in Table 3.2.

Table 3.2 Pressure drops in AGV [5].

Flow Rate (µl/min)	Pressure Drop (Pa)
1.6	693.27
2.5	999.92
5	1133.24
10	1279.89
20	1386.55
25	1439.88

3.2.5.2 Pressure Drops in Molteno Implant

In the scope of this thesis, single and double plate Molteno devices will be examined. Their approximate flow rates at various pressure differences are shown in Table 3.3 and Table 3.4.

Table 3.3 Flowrates of single plate Molteno device under various pressure differences [22].

Differential Pressure (mmHg)	Flow Rate in Single Plate Molteno Device (µl/min)
5	9.1
10	21.6
15	34.7
20	47
25	60

Table 3.4 Pressure drops of double plate Molteno device at various flowrates [22].

Flow Rate in Double Plate Molteno Device (µl/min)	Pressure Drop (mmHg)
5	4.11
10	5.16
15	6.30
20	7.31
25	8.43

3.2.5.3 Pressure Drop in XEN 45 Implant

The XEN 45 implant was designed to drop IOP and prevent hypotony at physiological flowrate by using Hagen-Poiseuille equation (3.6). It has diameter of 45 µm and a length of 6 mm [5].

At physiologic conditions, temperature is 37 °C and viscosity is 0.0006904 Pa.s [6]

$$\Delta P = \frac{128\ x\ 0.0006904 x\ 0.006\ x \frac{2.5\mu l 1 min 10^{-9} m^3}{min\ \ 60s\ \ \ 1\mu l}}{\pi x 0.000045^4} = 1717.2\ Pa = 12.86\ mmHg \qquad (3.29)$$

3.2.5.4 Pressure Drops in ExPress Implant

Although ExPress implant has models such as P20, P50, P200, in this thesis we will examine only P200 model. The produced flow rates with respect to pressure difference in experimental setup are given in Table 3.5.

Table 3.5 The produced flow rate with respect to pressure difference in experimental setup [23].

Differential Pressure (mmHg)	Flow Rate(µl/min)
5	664
10	1180
15	1575
20	1928
25	2241

3.2.6 Losses in the Sections 5-6, 6-7 and 7-8

Pressure losses at the sections 5-6, 6-7 and 7-8, are the same as sections 1-2, 2-3 and 3-4 respectively.

3.2.7 Pressure Losses at the Pipe Outlet

The pipe outlet loss which is the same equation (3.9) but K=1 (K is equal to unity for whatever the shape of outlet).

$$\text{So, } \Delta P_e = 1\ x\ \frac{1000\ x\ 0.0000842^2}{2} = 3.545\ x\ 10^{-6}\ Pa \qquad (3.30)$$

3.3 Discussion of Experimental Setup

As can be seen from loss calculations, pressure losses taking place at the sudden expansion, sudden contraction, inlet-outlet losses are negligibly small in comparison with the considerable pressure losses at GDD and in pipes. Similarly, the pressure

losses at the pipe bends are also negligible because of microfluidic flow characteristics.

This experimental setup has been designed as analogous to human eye. In the eye, aqueous humour, which is liquid supplying nutrients to eye cells, is produced at ciliary body (at 2-3 µl/min flowrate). Then, it flows from posterior chamber trough pupil into anterior chamber. When AH comes into anterior chamber, it drains passing through the porous tissue called as the trabecular meshwork. And AH flows to Schlemm's canal. Eventually, Schlemm's canal delivers it into the episcleral blood vessels via aqueous veins. This setup simulates all these phases of aqueous humour flow. It's thought that this experimental setup will eliminate the disadvantages (low precision, low repeatability, analogy to eye structure etc.) of experimental setups used in literature.

CHAPTER IV

THREE DIMENSIONAL MODELLING AND MESHING OF THE EXPERIMENTAL SETUP

4.1 Modelling Approach

To simulate the experimental setup, it will be sketched as 3D and four types of glaucoma drainage devices will be tested on it. These glaucoma drainage devices are Ahmed Glaucoma Valve, Molteno implant (both one and double plate), XEN 45 implant and Express implant. Since Ahmed and Molteno Implants have complicated shape, we tested them by using porous media properties acquired from experimental data in literature. However, XEN 45 and ExPress implants have been drawn due to their simple geometry.

In the scope of this thesis, all geometries were drawn in Design Modeler which is modelling program embedded in ANSYS WORKBENCH R18.2 and meshed with ANSYS MESHING. The simulations were performed on Windows 10 with Intel Core i7-7700HQ 2.81 GHz CPU and 16 GB RAM.

4.2 Geometry Construction

In this section general experimental setup was drawn. Then, glaucoma drainage devices added at its tip. Experimental setup consists of reservoir, pipe and sensor. The reservoir has cylindrical shape with 17.2 mm diameter and 110 mm length. The inside diameter of pipe is 1/32 inches. The sensor has 0.43 mm inside diameter and 52 mm length in Figure 4.1.

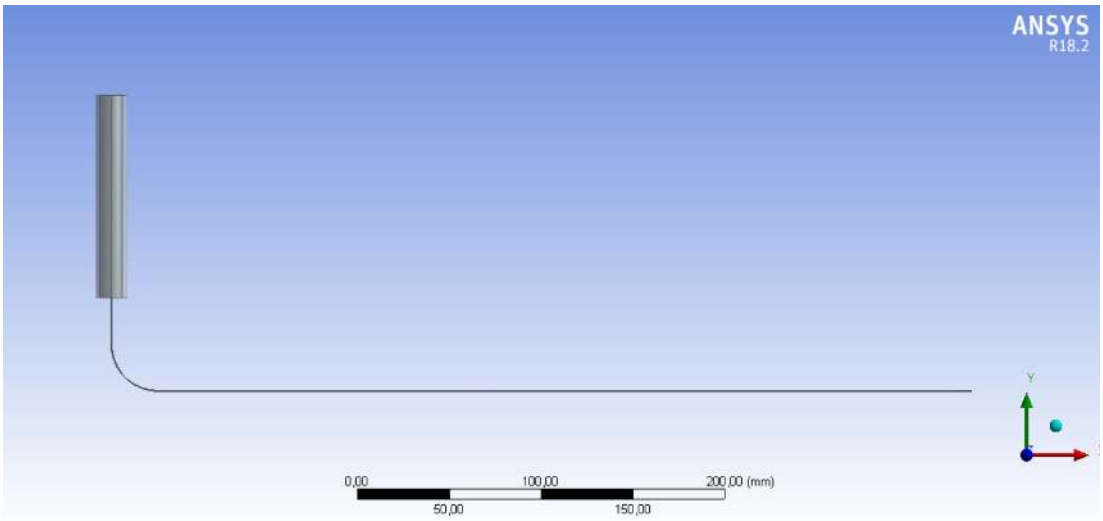

Figure 4.1 Sketching of the experimental setup.

4.2.1 AGV and Molteno Implant Experimental Setups

Both Ahmed and Molteno implants have complicated geometry. Because of this reason, they were represented a symbolic cylindrical shape at the tip of experimental setup in Figure 4.2. The diameter of the shape is the same with the pipe and its length is 10 mm.

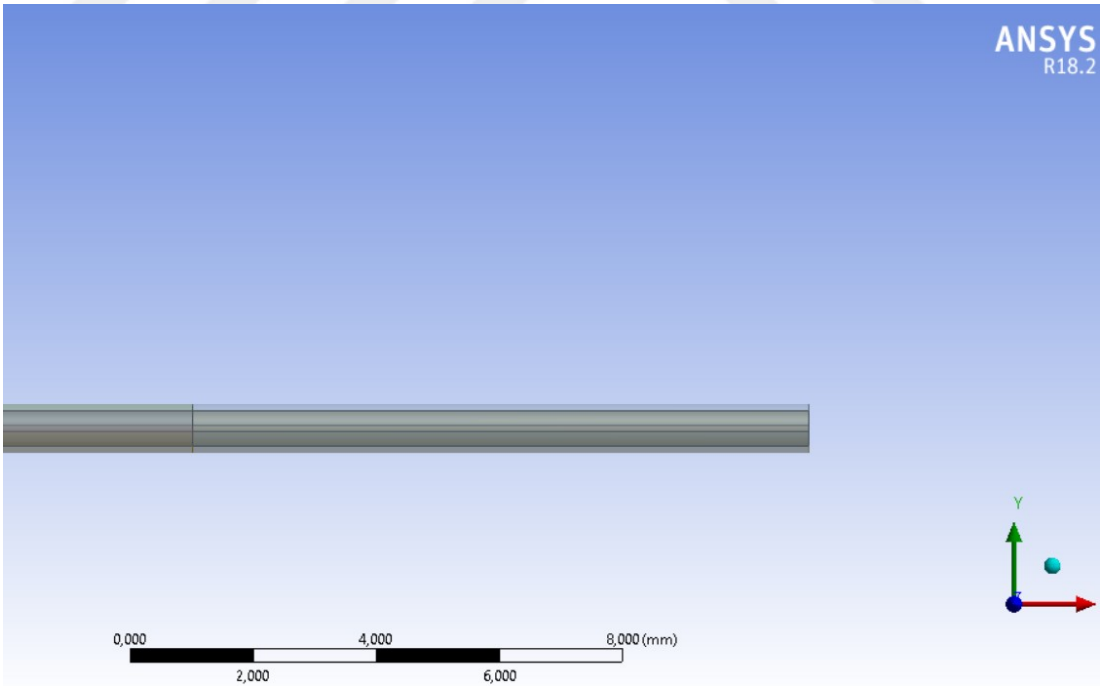

Figure 4.2 Sketching of the porous media section.

4.2.2 XEN 45 Implant Experimental Setup

XEN implant has straight cylindrical shape with lumen at its centre. The lumen diameter is 45 µm and its length is 6 mm, Figure 4.3.

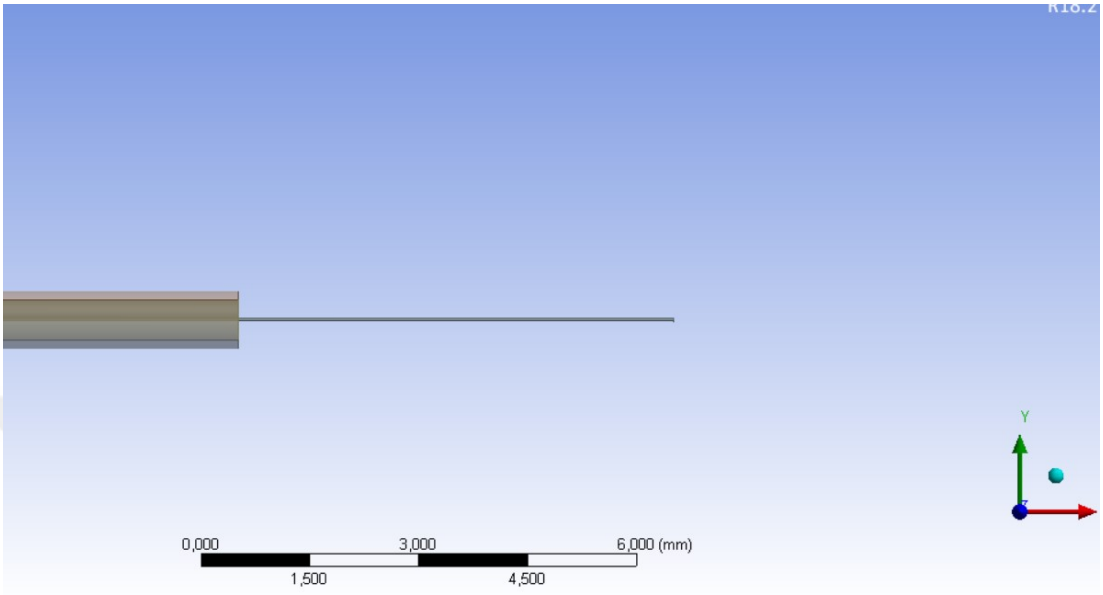

Figure 4.3 Sketching of XEN implant.

4.2.3 ExPress P200 Implant Experimental Setup

The Express implant is a non-valved tube with a disk flange [24]. Dimensions of P200 implant are shown in Table 4.1 and its sectional view is given in Figure 4.4.

Table 4.1 Dimensions of P200 model ExPress implant [24].

Length, Whole (mm)	2.56±0.01
Width, tube section (µm)	379.3±7.0
Length, complete tube section (from flange to side orifice) (mm)	1.35±0.03
Internal diameter, subconjuctival space end (µm)	206.4±3.3
Internal diameter, anterior chamber end (µm)	204.5±0.9

Figure 4.4 Cross-sectional view of ExPress P200 device.

Because this device has the main inlet and side inlet, this device was placed in the tube with inside diameter 1/32 inches to see flow distribution by the contrast with other devices in Figure 4.5.

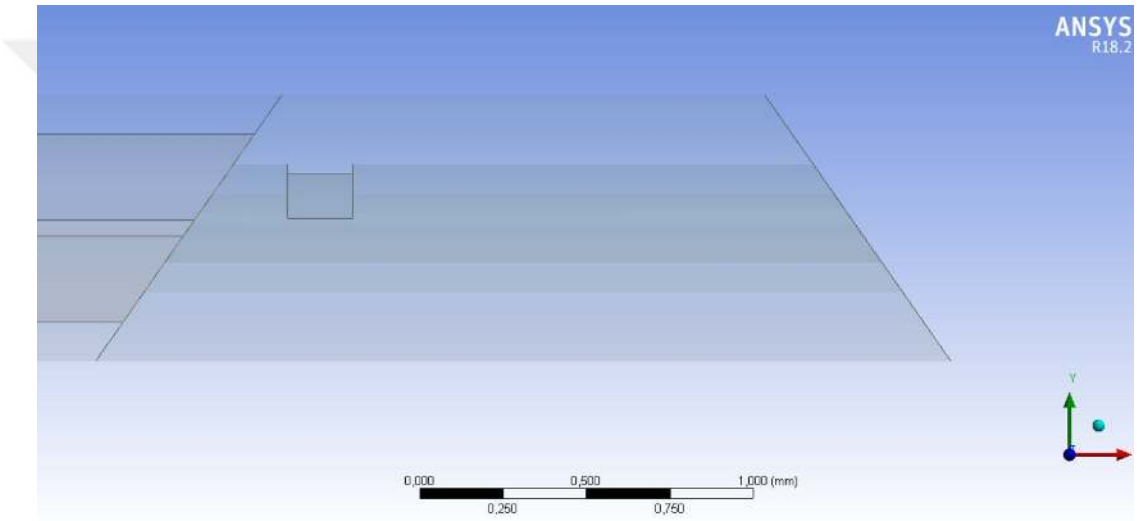

Figure 4.5 Sketching of ExPress P200 device.

4.3 Geometry Meshing

4.3.1 Meshing of AGV and Molteno Experimental Setups

All geometries were meshed with structural hexahedral meshes because of it has the highest accuracy in solution. However, the geometry has to be modified to apply this type of meshing. So, the geometry was sliced to obtain structured hexahedral meshes as seen in Figure 4.6.

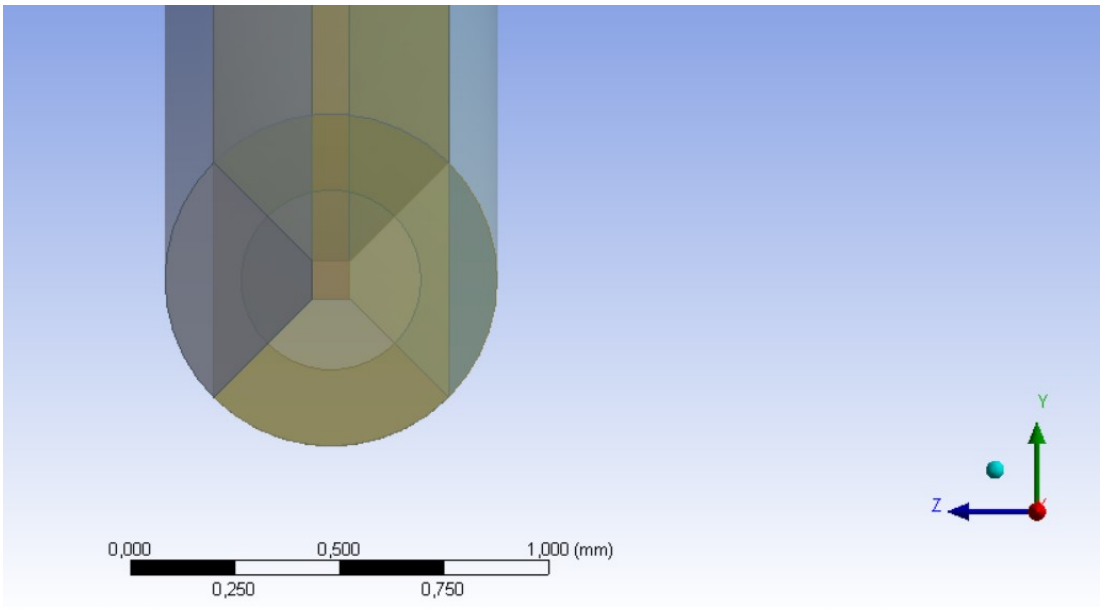

Figure 4.6 Sliced geometry of the experimental setup.

The edge sizing was applied to these created edges to control mesh size. Then five named selections were created to divide experimental setup according to its components. These are; Piston which was applied on top face of the reservoir, outlet which was applied outlet face of the GDDs, reservoir, pipe and porous. Then Sweep method for reservoir named selection, multizone method for pipe named selections and porous were applied. High level of structured hexahedral meshes with 94.6% orthogonal quality was obtained after these arrangements in Figure 4.7.

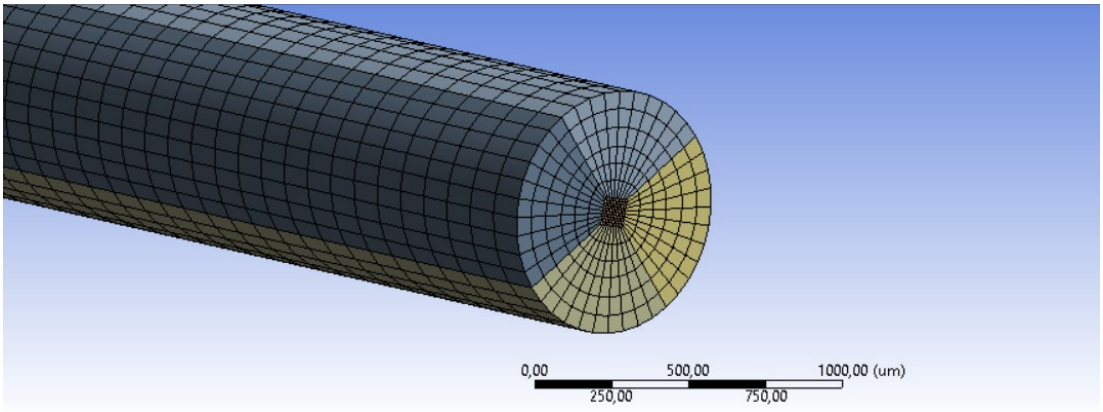

Figure 4.7 Meshing of AGV and Molteno experimental setups.

4.3.2 Meshing of XEN 45 Implant Experimental Setup

The same procedures were applied for XEN 45 implant too. Five named selections were created depending on the characteristic of each component existing on the

experimental setup. These are; Piston which is applied on top face of the reservoir, outlet which is applied outlet face of the GDDs, reservoir, pipe and XEN 45. Then Sweep method for reservoir named selection, multizone method for pipe and sweep method for XEN 45 were applied. Again, a high level of structured hexahedral meshes with 88% orthogonal quality was obtained after these arrangements as shown in Figure 4.8.

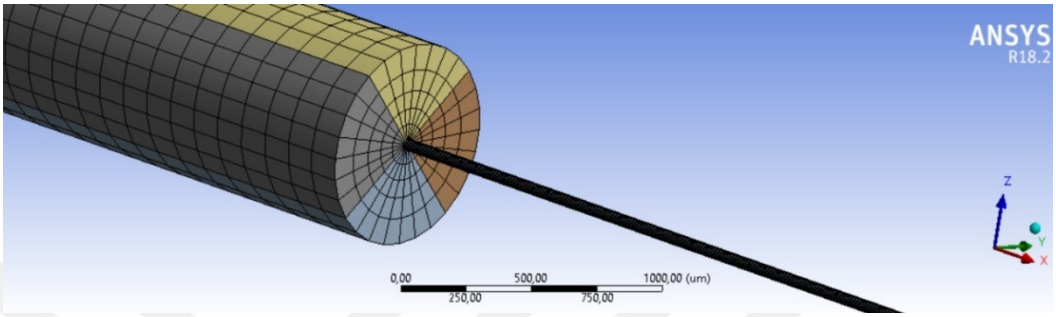

Figure 4.8 Meshing of XEN experimental setup.

4.3.3 Meshing of ExPress P200 Implant Experimental Setup

Meshing of ExPress implant experimental setup is a bit different than other devices because of its complex geometry. The experimental setup is segmented to prevent generation of unstructured and low quality meshes arising from inclined geometry of ExPress implant. The pipe was sliced starting from the end of the curvature, two sides of sensor and end of the pipe. So, five sweepable bodies were obtained. Lastly, sweep method was assigned on these bodies and patch conforming method was assigned for ExPress implant. So, hexahedral meshes for pipe and reservoir, tetrahedral meshes for ExPress implant were created with 98% orthogonal quality in Figure 4.9.

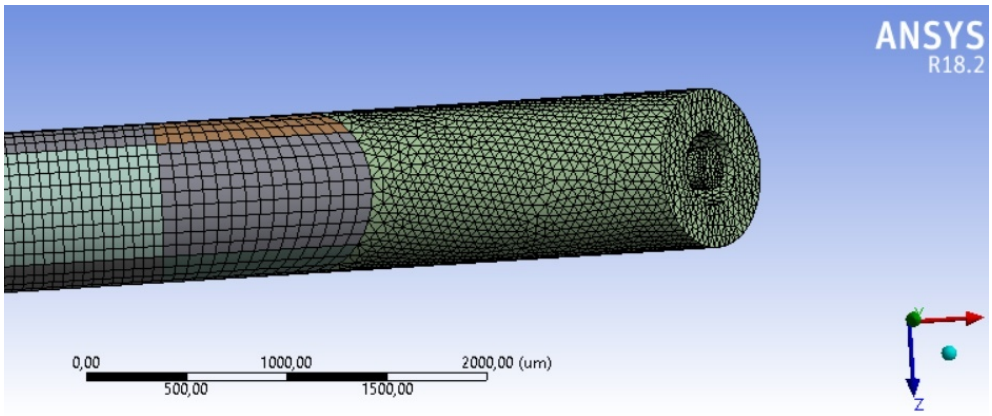

Figure 4.9 Meshing of ExPress P200 experimental setup.

CHAPTER V

SOLUTION AND RESULTS

5.1 Solution Methodology

As it was mentioned before, geometrical solution for XEN, ExPress implants and porous media solution for Ahmed, Molteno implants were used.

5.2 Theoretical Background of Porous Media

Porous media [25] allows us to simulate elements without drawing their geometry using experimental data. It uses standard fluid flow equations with a momentum source term in addition. This source term has two components; one is "viscous loss term" and the other one is "inertial loss term". It can be seen in Equation 5.1, first term on the right hand-side of equation is viscous loss term and second term on the right hand-side of equation is inertial loss term.

$$S_i = -\left(\sum_{j=1}^{3} D_{ij}\mu v_j + \sum_{j=1}^{3} C_{ij}\frac{1}{2}\rho|v|v_j\right) \tag{5.1}$$

where,

S_i = Source term for *i*th x, y, z momentum equation.

D, C = Prescribed matrices

$|v|$ = Magnitude of velocity

The equation (5.1) can be simplified for homogeneous porous media.

$$S_i = -\left(\frac{\mu}{\alpha}v_i + C_2\frac{1}{2}\rho|v|v_i\right) \tag{5.2}$$

where,

α = Permeability.

C_2 = Inertial resistance factor.

5.3 Deriving Porous Media Inputs of GDDs

Porous media inputs can be obtained from experimental tabulated pressure drop versus velocity data. We have to add in the formula porous media thickness (Δn) to calculate pressure drop across the porous media. And the formula becomes (Eq. 5.3);

$$\Delta P = -S_i \Delta n \tag{5.3}$$

Graph of tabulated data are drawn. Then, equation of this graph is placed into equation (5.3).

5.3.1 Deriving of Porous Media Inputs of AGV

Tabulated experimental data for AGV is shown in Table 5.1 [5].

Table 5.1 Tabulated experimental data for AGV.

Flow Rate (µl/min)	**Velocity (m/s) in 0.79375 mm Diameter of Porous Media**	**Pressure Drop (Pa) [4]**
1.6	5.39e-5	693.27
2.5	8.42e-5	999.92
5	16.84e-5	1133.24
10	33.68e-5	1279.89
20	67.36e-5	1386.55
25	84.20e-5	1439.88

Graph of pressure loss with respect to velocity is shown in Figure 5.1.

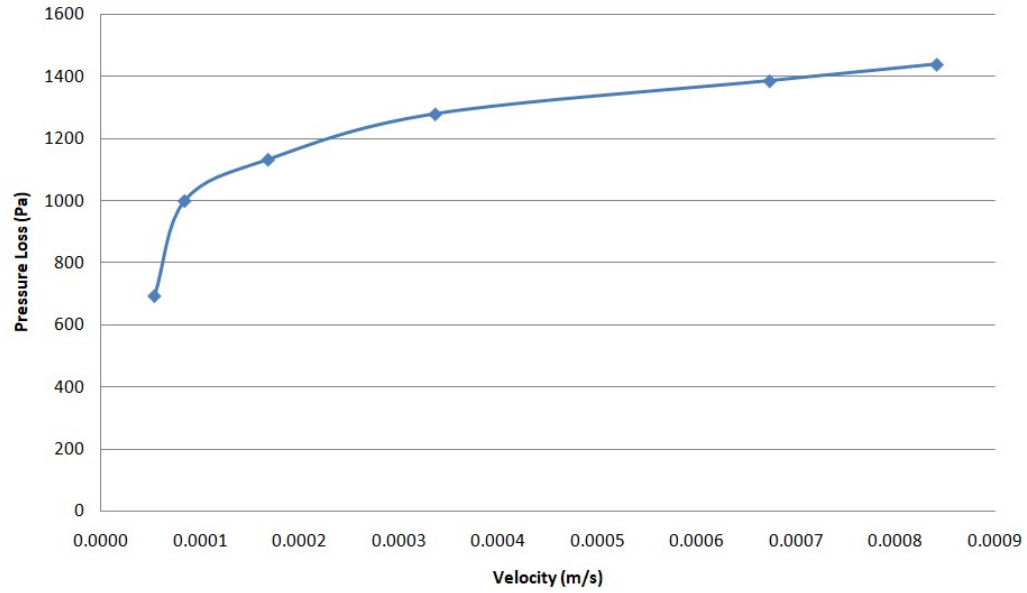

Figure 5.1 Graph of pressure loss in AGV with respect to velocity.

As can be seen from the graph, pressure drop changes linearly after the flow rate of 5 µl/min. This is because of the Ahmed implant is a valved implant. Until the 5 µl/min, pressure loss increases as parabolic but after the valve is fully open, it increases as linearly. So, the graph was divided as before and after the valve is fully opened, to obtain best fit curve in Figure 5.2 and 5.3.

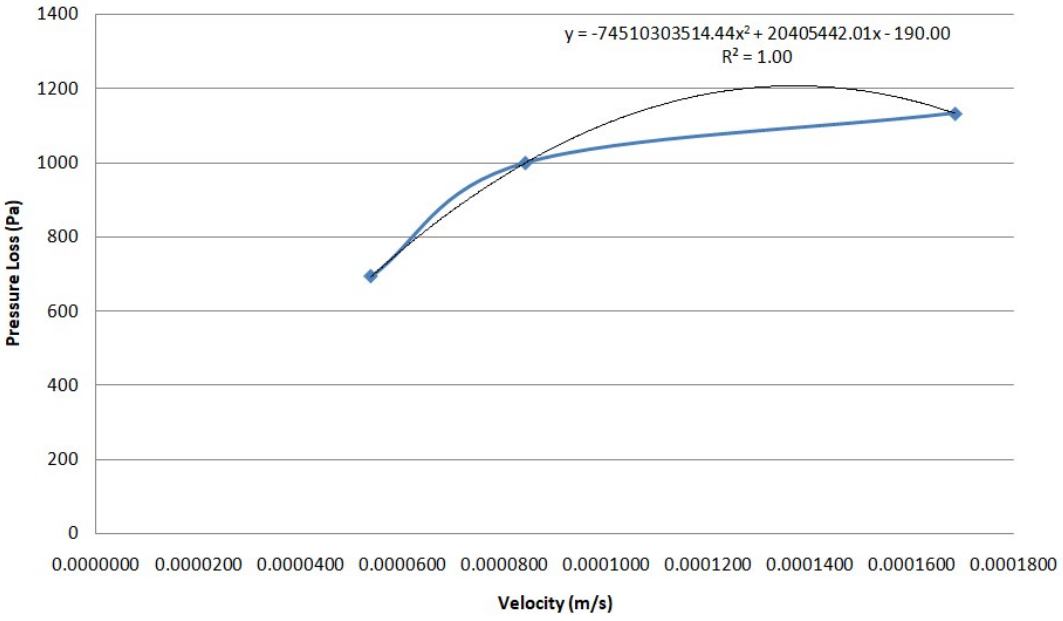

Figure 5.2 Graph of pressure loss in AGV with respect to velocity (from 0 to 5 µl/min).

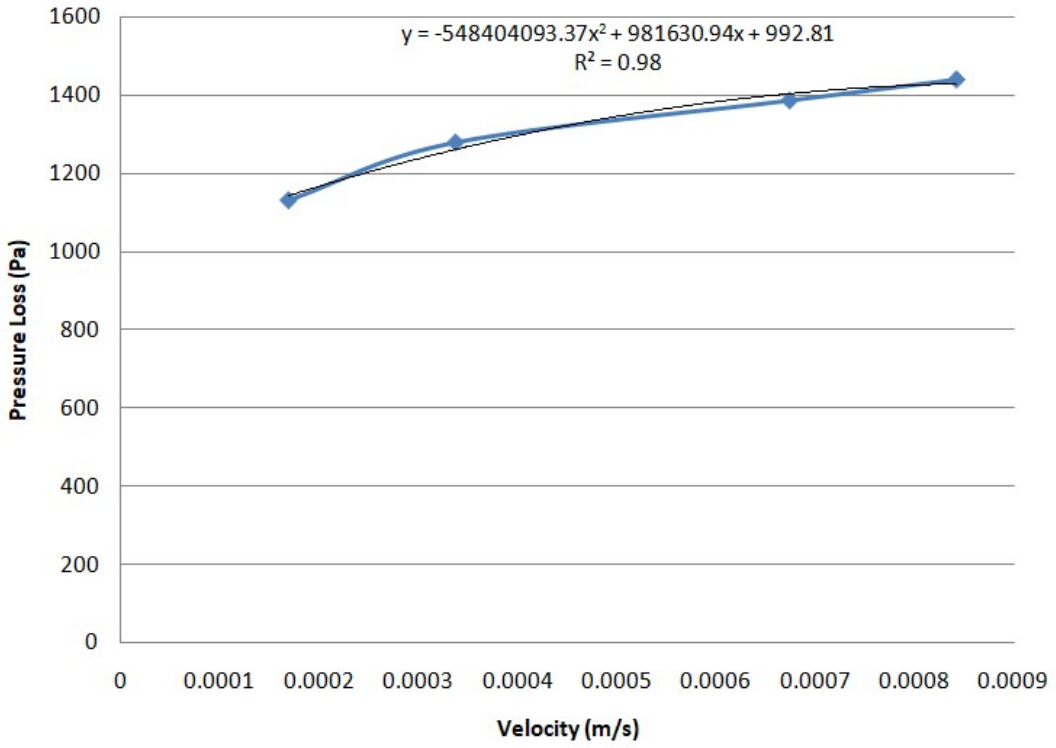

Figure 5.3 Graph of pressure loss in AGV with respect to velocity (from 5 to 25 µl/min).

For first graph, our equation is;

$$\Delta P = -74510303514v^2 + 20405442v - 190 \quad (5.4)$$

If we put this equation into equation 5.3;

$$-74510303514 = \frac{1}{2}\rho C_2 v^2 \quad (5.5)$$

and;

$$20405442 = \frac{\mu}{\alpha} v \quad (5.6)$$

where,

$$\rho = 998.2\ kg/m^3 \quad (5.7)$$

$$\mu = 0.001003 \frac{kg}{m.s} \quad (5.8)$$

So,

$$C_2 = -14928932782 \quad (5.9)$$

$$\frac{1}{\alpha} = 2.0344e + 12 \quad (5.10)$$

For second graph our equation is;

$$\Delta P = -548404093.4v^2 + 981631v + 992.8 \quad (5.11)$$

So,

$$C_2 = -109878600.2 \quad (5.12)$$

$$\frac{1}{\alpha} = 97869485527 \quad (5.13)$$

5.3.2 Deriving of Porous Media Inputs of Molteno Implants

The graph of the data from Tables 3.3 and 3.4 for single and double plate Molteno devices in Figure 5.4 and 5.5 respectively;

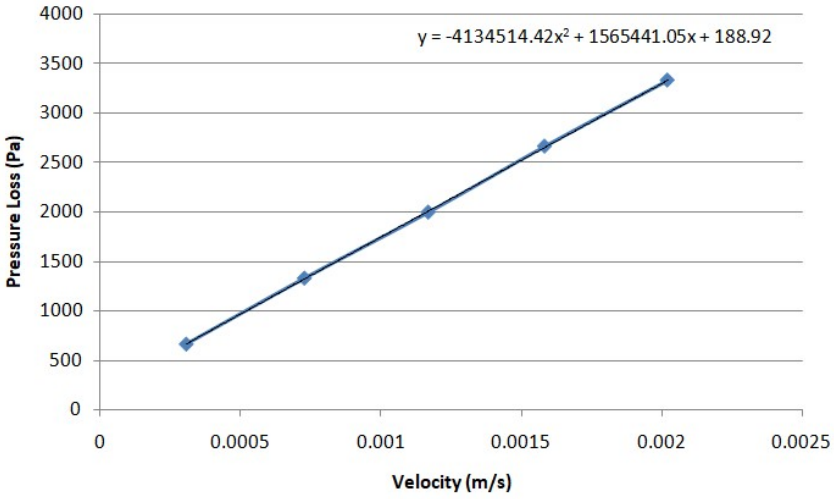

Figure 5.4 The graph of the single plate Molteno device data from the Table 3.3.

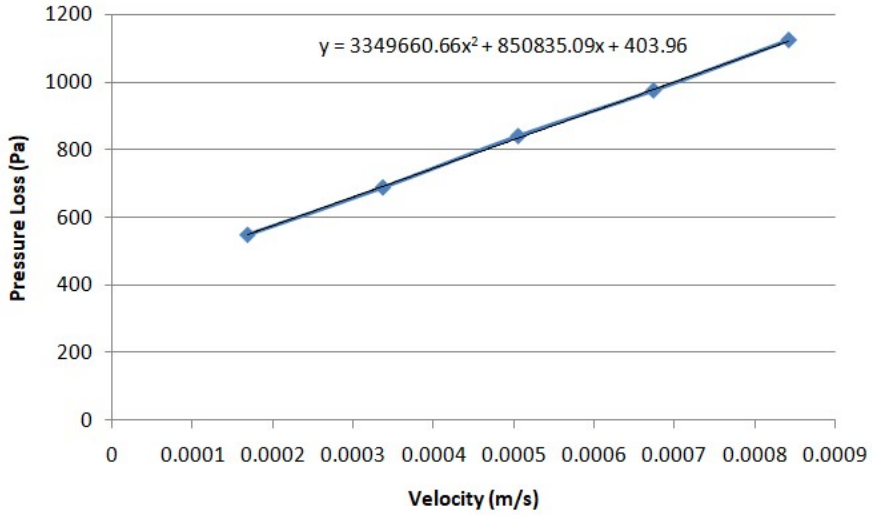

Figure 5.5 The graph of the double plate Molteno device data from the Table 3.4.

If we repeat calculation at the section 5.3.1, we find the porous media inputs;

For single plate Molteno device;

$$C_2 = -828394 \tag{5.14}$$

$$\frac{1}{\alpha} = 1.5608E + 11 \tag{5.15}$$

For double plate Molteno device;

$$C_2 = 671140.2 \tag{5.16}$$

$$\frac{1}{\alpha} = 8.4829\text{E} + 10 \tag{5.17}$$

5.4 Solution Parameters

In simulation of all GDDs, transient solution and laminar model were used. Then, AH was selected as the material for all fluid zones. To simulate piston movement, dynamic mesh was created with layering method (ratio based) in Figure 5.6. As a boundary condition only pressure outlet was selected. The inlet was identified with a piston movement. To create this movement "DEFINE_CG_MOTION" UDF code was used. Firstly, top face of the reservoir was selected as dynamic zone, and then its motion was monitored by the UDF code written in C. An example UDF code used for simulation of any GDD at 2.5 µl/min is presented in Figure 5.7. The piston

velocity in UDF was calculated according to diameter of reservoir and flow rate. Then, first order implicit was selected as the solver.

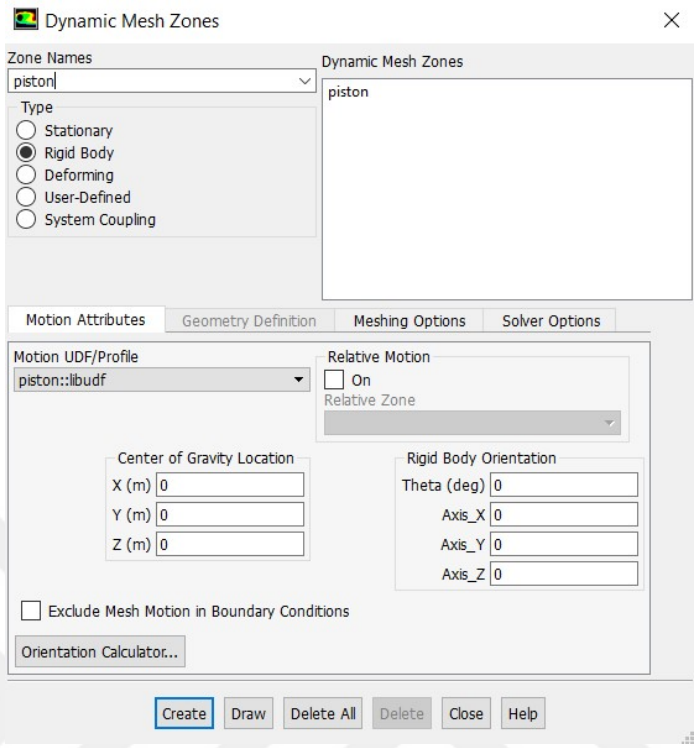

Figure 5.6 Dynamic Mesh Zone.

```
#include "udf.h"
#include "dynamesh_tools.h"

real v_prev = 0.0;
time_prev = 0.0;

real fixed_velocity = 1.79325e-07
;

DEFINE_CG_MOTION(piston, dt, vel, omega, time, dtime)

{
    NV_S (vel, =, 0.0);
    NV_S (omega, =, 0.0);
    vel[1] = -fixed_velocity;
}
```

Figure 5.7 UDF of piston movement for any GDD at 2.5 µl/min.

5.5 Mesh Dependency Tests of GDDs

5.5.1 Mesh Dependency of AGV and Molteno Implants

Because the AGV and Molteno share the same experimental setup, their mesh dependency tests can be made together. Now, it is examined for 2.5 µl/min AGV in Table 5.2.

Table 5.2 Mesh independence test for AGV and Molteno.

MESH (AGV)	ΔP at setup	ΔP at porous	ΔP Total	Elements	Node
Mesh 1	4	1190	1194	257850	302488
Mesh 2	5	1189	1194	1093056	1168557
Mesh 3	4.4	1189.6	1194	1453920	1547221
Mesh 4	4	1190	1194	3249240	3387924

As seen in the Table 5.2, change of results is very small with respect to increase of mesh. So, the mesh 3 is sufficient for our simulation.

5.5.2 Mesh Dependency of XEN 45 Implant

Mesh independence test results for XEN 45 implant are given in Table 5.3.

Table 5.3 Mesh independence test for XEN 45 implant.

MESH (XEN45)	ΔP at setup	ΔP at XEN Implant	ΔP Total	Elements	Node
Mesh 1	2.5	1652.5	1655	478030	542784
Mesh 2	3	1647	1650	594223	662392
Mesh 3	3	1616	1619	1106460	1206770
Mesh 4	3.3	1635.5	1638.8	2067630	2236668

When Mesh 3 and Mesh 4 are examined, it can be seen readily that although the mesh number is almost doubled, the result increases very small according to increase of mesh number. So, mesh 4 is selected for our simulation.

5.5.3 Mesh Dependency of ExPress P200 Implant

Mesh independence test results for ExPress P200 implant are given in Table 5.4.

Table 5.4 Mesh independence test for ExPress implant.

MESH (ExPress)	ΔP at setup	ΔP at ExPress	ΔP Total	Elements	Node
Mesh 1	1009,1	568,6	1577,7	1092680	1118738
Mesh 2	1147	566	1713	1610594	1644060
Mesh 3	1183	566	1749	3184620	3236631
Mesh 4	1198	568	1766	4340996	4410120
Mesh 5	1194	570	1764	7496664	7619232

It's obvious that the results converge to an exact value see Table 5.4. Besides, especially when the mesh size of ExPress implant was decreased further up to 15 μm to be assured of accuracy of GDD results but no change was observed. Mesh 4 is sufficient for our simulation.

5.6 Solutions

Convergence parameter is very important to obtain fine results. At first, convergence residuals had been set to 10^{-5} for all GDDs before simulations were done. However, it was noticed that time of solutions was dramatically increasing because of reversed flows. So, the criteria changed as 10^{-4} for AGV and Molteno, 10^{-3} for XEN implant and 10^{-5} for ExPress. In this way it was seen that results were changed very slightly. After selection of convergence criteria, simulations were initialised with hybrid initialisation. Then, the computations were run.

5.6.1 Analysis of Results

5.6.1.1 Results of AGV

The aqueous flow through the AGV porous model was simulated at specified flow rates. Its CFD results are shown in Table 5.5. The offsets caused by equation 5.4 and 5.11 were added on CFD results.

Table 5.5 The CFD results of AGV.

Flow rate (µl/min)	Pressure Drop in Experimental Setup by CFD (Pa)	Pressure Drop in GDD by CFD (Pa)	Offset from Porous Equation of Experimental Results (Pa)	Pressure Drop CFD + Offset (Pa)
1.6	2.8	883	-190	693
2.5	4.4	1189.6	-190	999.6
5	8.9	150	+992.8	1142.8
10	17.8	269	+992.8	1261.8
20	35.5	413.5	+992.8	1406.3
25	44.3	438.7	+992.8	1431.5

5.6.1.2 Results of Molteno Implants

The aqueous flow through the Molteno porous models were simulated at specified flow rates. Their CFD results are shown in Tables 5.6 and 5.7. The offsets caused by equations in Tables 3.3 and 3.4 were added on CFD results.

Results of Single Plate Molteno Implant;

Table 5.6 The CFD results of single plate Molteno implant.

Flow rate (µl/min)	Pressure Drop in GDD by CFD	Pressure Drop in Experimental Setup by CFD	Offset from Porous Equation of Experimental Results	Pressure Drop CFD + Offset
9.1	479.7	16.3	+188.9	669.6
21.6	1137.4	38.6	+188.9	1326.3
34.7	1825	62	+188.9	2014.9
47	2469.3	83.7	+188.9	2658.2
60	3148.6	106.4	+188.9	3338.5

Results of Double Plate Molteno Implant;

Table 5.7 The CFD results of double plate Molteno implant.

Flow rate (µl/min)	Pressure Drop in GDD by CFD	Pressure Drop in Experimental Setup by CFD	Offset from Porous Equation of Experimental Results	Pressure Drop CFD + Offset
5	143.6	8.6	+404	547.6
10	287.4	17.8	+404	691.4
15	431.4	26.6	+404	835.4
20	575.6	35.5	+404	979.6
25	720	44.3	+404	1124

5.6.1.3 Results of XEN 45 Implant

The aqueous flow through the XEN implant geometric model was simulated at physiological flow rate. Its CFD result is shown in Table 5.8.

Table 5.8 The CFD results of XEN 45 implant

Flow rate (µl/min)	ΔP at Setup by CFD (Pa)	ΔP at XEN Implant by CFD (Pa)
2.5	3.3	1635

5.6.1.4 Results of ExPress P200 Implant

The aqueous flow through the ExPress implant geometric model was simulated at physiological flow rate. Its CFD result is shown in Table 5.9.

Table 5.9 The CFD results of ExPress implant.

Flow rate (µl/min)	Pressure Drop in Experimental Setup by CFD	Pressure Drop in GDD by CFD
664	1195.7	575.4
1180	2129.2	1246.3
1575	2847.3	1898
1928	3494.1	2582.4
2241	4068	3265.5

CHAPTER VI

COMPARISON OF THE RESULTS

In this chapter, the CFD results of GDD tests will be compared firstly with experimental results in literature and pressure losses in experimental setup will be compared with manual calculation as in section 3.2.

6.1 Comparison of AGV Results

The Table 5.5 shows comparison of CFD results of AGV and pressure drop in literature, also comparison of pressure drop in Experimental setup by CFD with manual calculation. As seen in Table 5.5, CFD results of experimental setup and manual calculation meet well with each other. Again, it can be seen in Figure 5.1, the CFD results of AGV are very convenient with results in literature. So, the AGV is simulated well by porous media.

Table 6.1 The Comparison of AGV results.

Flow rate (µl/min)	Pressure Drop in GDD [5] (Pa)	Pressure Drop in Experimental Setup (Manual Calculation)	Pressure Drop CFD + Offset (Pa)	Pressure Drop in Experimental Setup by CFD (Pa)	Percentage error (CFD vs Experiment)
1.6	693.27	2.9	693	2.8	-0.0005
2.5	999.92	4.5	999.6	4.4	-0.0004
5	1133.24	9	1142.8	8.9	-0.0003
10	1279.89	18	1261.8	17.8	-1.46
20	1386.55	36	1406.3	35.5	-1.35
25	1439.88	45	1431.5	44.3	-0.65

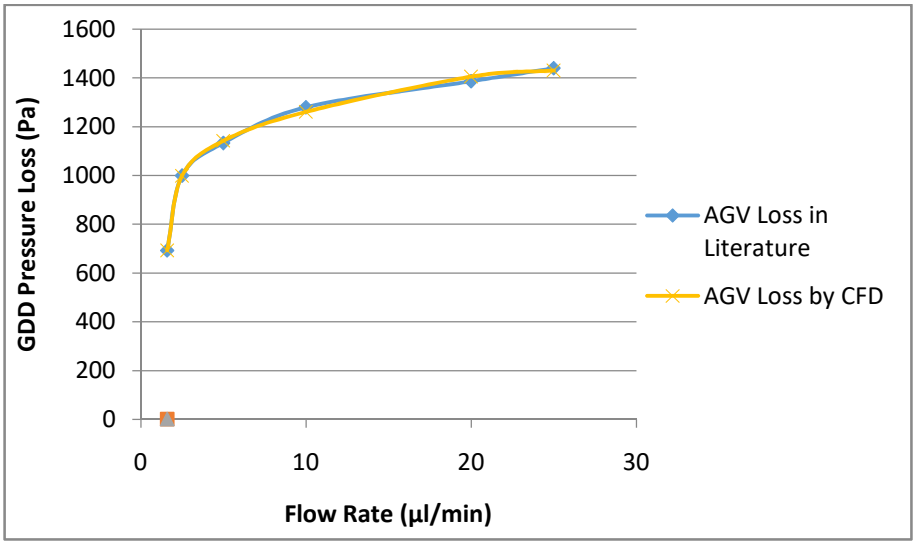

Figure 6.1 Comparison of AGV CFD results with results in literature [5].

6.2 Comparison of Molteno Device Results

As seen in Table 5.6 results of single plate Molteno and Table 5.7 double plate Molteno devices have very convenient CFD results with literature. This is because of

Molteno devices are non-valved devices and they have constant, rigid geometry by the contrast with AGV. So, their pressure loss versus flow rate graphs is linear as seen in Figure 5.2 and 5.3.

Table 6.2 The comparison of single plate Molteno implant results.

Flow rate (µl/min)	Pressure Drop in GDD (Prata et al.) [22]	Pressure Drop in Experimental Setup (Manual Calculation)	Pressure Drop in Experimental Setup by CFD	Pressure Drop CFD + Offset	Percentage error (CFD vs Experiment)
9.1	666.6	16.4	16.3	669.6	0.26
21.6	1333.2	38.9	38.6	1326.3	-0.57
34.7	1999.8	62.5	62	2014.9	0.65
47	2666.5	84.7	83.7	2658.2	-0.37
60	3333.1	108.1	106.4	3338.5	0.08

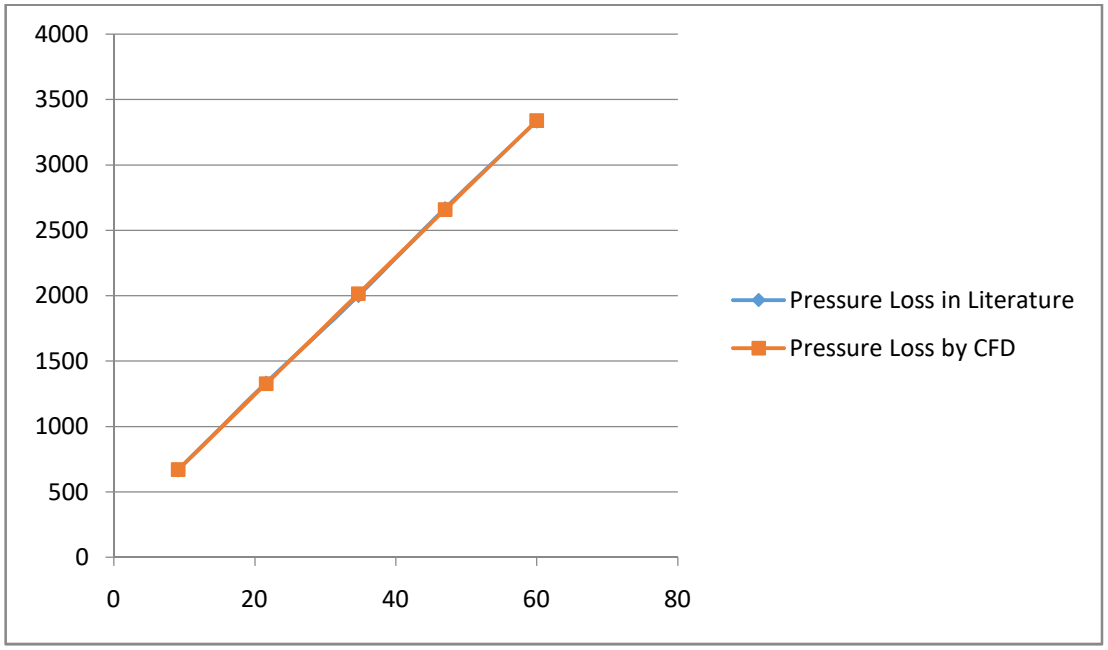

Figure 6.2 Comparison of single plate Molteno device CFD results with results in literature [22].

Table 6.3 The comparison of double plate Molteno implant results.

Flow rate (µl/min)	Pressure Drop in GDD (Prata et al.) [22]	Pressure Drop in Experimental Setup (Manual Calculation)	Pressure Drop in Experimental Setup by CFD	Pressure Drop CFD + Offset	Percentage error (CFD vs Experiment)
5	548	9	8.6	547.6	-0.11
10	687.9	18	17.8	691.4	0.43
15	839.9	27	26.6	835.4	-0.63
20	974.6	36	35.5	979.6	0.41
25	1123.9	45	44.3	1124	-0.10

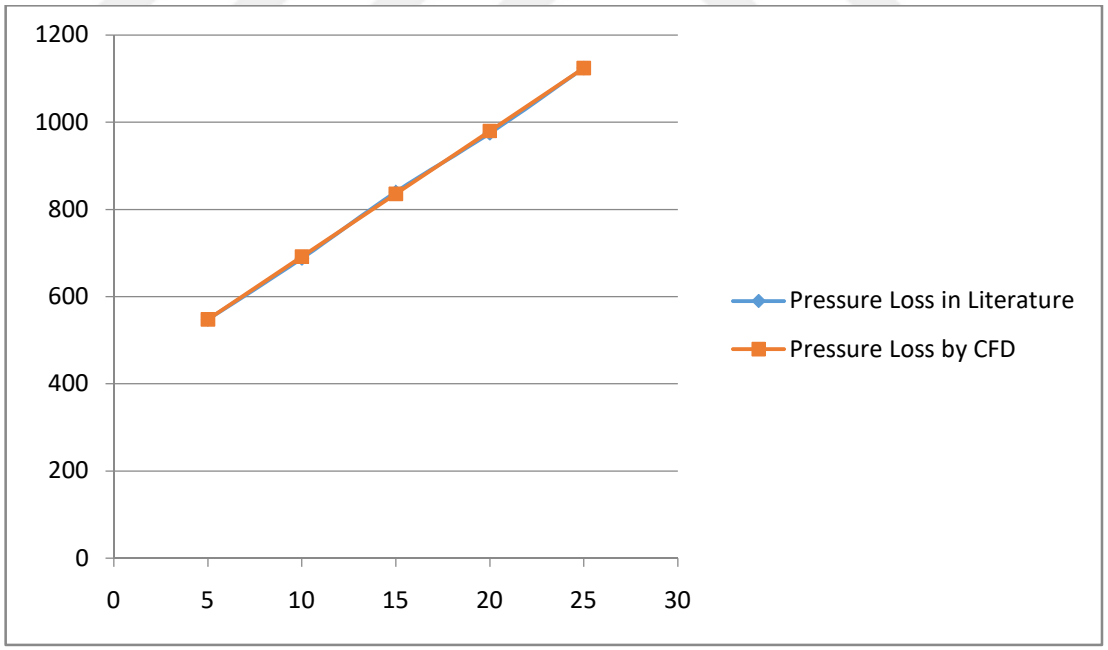

Figure 6.3 Comparison of double plate Molteno device CFD results with results in literature [22].

6.3 Comparison of XEN 45 Implant Results

When both Hagen-Poiseuille solution and CFD solution are compared with the experimental result of Sheybani et al. [6], It's noticed that their results did not matched with ours. They said that the XEN implant provided 6.28 to 7.85 mm Hg of backpressure, thus theoretically protecting against hypotony. It's deduced from these sentences that the results were above the hypotony value (5 mmHg). This means that absolute pressure losses in XEN implant are 11.28 to 12.85 mm Hg. In vivo results were investigated from literature to confirm our inference. Then, our results and in-vivo results of Tan et al. [26] were compared. They measured pressure drop after one-month from implantation as 13.7±3.7 mm Hg. These results go along well with our results. When the Table 5.8 is analysed, it's seen that our results are in the range of in vitro, in vivo and Hagen-Poiseuille results.

Table 6.4 The comparison of XEN 45 implant results.

Flow rate (µl/min)	Mean Pressure Drop in GDD (Sheybani et al.) [6]	In Vivo Pressure Drop in GDD After a Month (Tan et al.) [26]	Pressure Drop in GDD (from Hagen-Poiseuille)	ΔP at Setup by CFD (Pa)	ΔP at XEN Implant by CFD	Percentage error (CFD vs Experiment)
2.5	12.065 mm Hg (1608.5 Pa)	13.7±3.7 mm Hg (1826 Pa)	1717.2 (12.86 mm Hg)	3.3	12.26 mm Hg (1635 Pa)	1.65

6.4 Comparison of ExPress Implant Results

When the CFD and experimental results of ExPress implant tests, it's seen that two results are parallel and compatible with small offsets. Although the meshing is increased and residuals criterion is decreased, the offset cannot be eliminated.

Table 6.5 The CFD results of ExPress implant.

Flow rate (µl/min)	Pressure Drop in GDD (Estermann et al.) (Pa) [23]	Pressure Drop in Experimental Setup (Manual Calculation) (Pa)	Pressure Drop in Experimental Setup by CFD (Pa)	Pressure Drop in GDD by CFD (Pa)	Percentage error (CFD vs Experiment)
664	666.6	1198.8	1195.7	575.4	-13.7
1180	1333.2	2134.4	2129.2	1246.3	-6.5
1575	1999.8	2852.8	2847.3	1898	-5.1
1928	2666.5	3496.6	3494.1	2582.4	-3.2
2241	3333.1	4068.7	4068	3265.5	-2.0

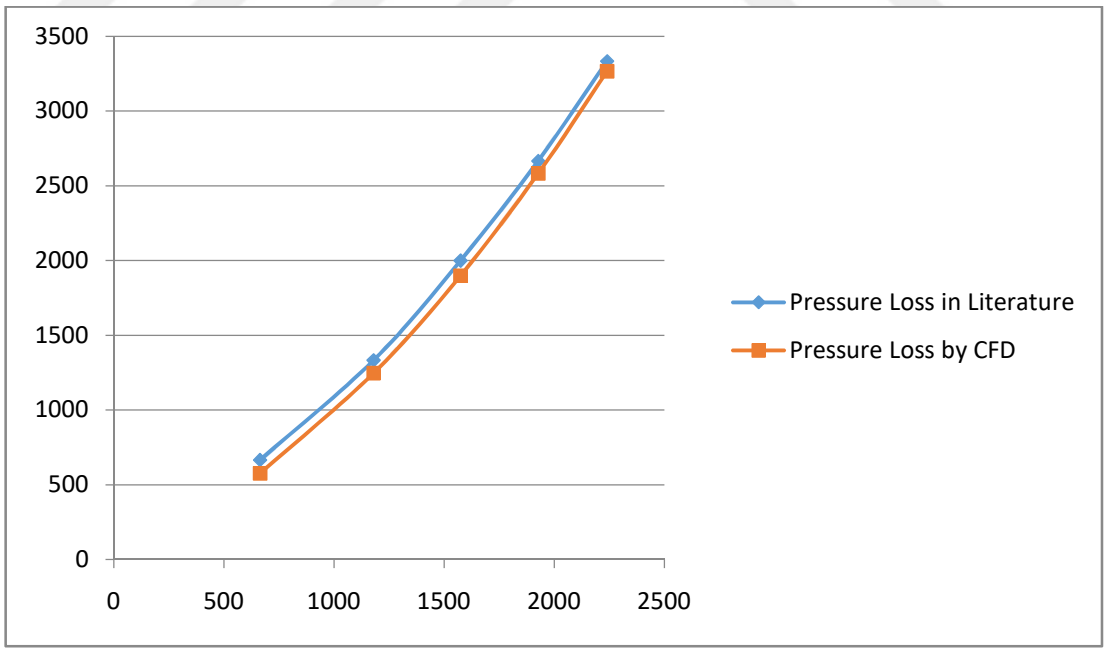

Figure 6.4 Comparison of ExPress P200 implant's CFD results and results in literature [23].

CHAPTER VII

DISCUSSION AND CONCLUSION

In this chapter, the general problems of GDDs were discussed. The problems faced during the CFD analysis and likely to be faced in future works were remarked. Lastly, suggestions for future works were presented.

7.1 General Problems of GDDs

When both CFD results shown in this study and experimental studies of GDD in literature are examined, both of them have convenient and overlapping results. However, almost all of the experimental studies are seem to be designed to solve problems of currently employed GDDs, they have lots of drawbacks in verifying real problems at these experimental setups. These real problems can be summarized as follows:

- Firstly, when the AGV is examined, it's seen that pressure drop of it is 999.9 Pa at physiologic flow rate. This is above the hypotony value (666.6 Pa). However, it's some defects cannot be seen at in vitro and ex vivo experimental setups. Firstly, it is complicated device which has a valve likely to be has malfunction. Then, it has high profile that causes inflammation.
- Secondly, if two kind of Molteno devices is examined, it's seen that both single plate and double plate devices have pressure values under the hypotony value though their flow rates are above the physiologic flow rate.
- The ExPress implant has very small pressure drop at physiological flow rate. This prevents the GDDs to use without a scleral flap and it causes hypotony.
- Lastly, the XEN 45 implant is seen that it has the most effective pressure drop without causing hypotony. Also, it has low profile. However, it again has some defects like erosion and implant migration.

7.2 Problems Faced

The general problem faced during the CFD analysis is about meshing of the geometry. Since structural mesh is said to provide best accuracy in results, all experimental setup and GDDs (except ExPress implant) meshed structurally. It was difficult to obtain good meshing results because of dimensional disproportion between GDDs (so small) and the experimental setup. Thus, this problem is overcome by dividing the geometries into different parts to obtain good meshing and size control.

The next problem is about dynamic meshing. The experimental setup has a piston movement so that the dynamic meshing was used with layering method. This achievement has limited the analysis especially at high flow rates. Because of the negative volume errors, the time step size was decreased under the order of 1 at high flow rates.

Another problem was in porous media. When the porosity values attained from experimental data was used in fluent, the last value of the experimental data diverges. This problem was solved by decreasing porosity values as small as possible.

The various problems were encountered during the meshing and solving. Some of these problems were solved immediately but some of them took a long time. For example, some meshes with low orthogonal quality divergences due to reversed flows, porous media errors etc.

7.3 Conclusions and Future Work

The aim of this thesis was to create numerical simulation of experimental setups for testing recent GDDs. Consequently, the simulations of experimental setups were created successfully.

As the future work suggestion, all the flow way of eye and bleb formations' porosity values can be created. This helps to make realistic GDD analysis.

The new works may be on the GDD defects which cannot be detected in vitro experimental setup. Especially, erosion and immigration problems of XEN implant can be solved by comprehensive ergonomics, material studies by calculating shear stresses on the implant.

Both CFD and experimental results of in-vitro study will be compared and post-operative data which will be taken from Faculty of Medicine of Gaziantep University can be an auxiliary result for in-vivo comparison.

REFERENCES

[1] Jyoti, G.K. (2006). Numerical Solution of Flow Resistance In Outflow Pathway And Intravitreal Drug Delivery In Vitrectomised Eyes Mechanical Engineering. M.S. Thesis, Louisiana State University.

[2] London Eye Unit. 2015. Possible Causes Of A Painless Red Eye. https://www.londoneyeunit.co.uk/wp-content/uploads/sites/15/2015/12/Red-Eye.jpg. 19.10.2010.

[3] Moon, S., Im, S., An, J., Ju, Park C., Kim, H. G., Park, S. W., Kim, H. I., Lee J.H. (2011). Selectively Bonded Polymeric Glaucoma Drainage Device for Reliable Regulation of Intraocular Pressure. *Biomed Microdevices*. **14**,325-335.

[4] Schwartz, K. S., Lee, R. K., Gedde, S.J., (2006). Glaucoma Drainage Implants: Critical Comparison of Types. *Current Opinion in Ophthalmology*. **101(5)**, 872-5.

[5] Kara, E. (2008). Design of an alternative glaucoma drainage device using CFD tools. M.S. Thesis, University of Gaziantep.

[6] Sheybani, A., Reitsamer, H., Ahmed, I.I.K. (2015). Fluid Dynamics of a novel micro-fistula implant for the surgical treatment of glaucoma. *Investigate Ophtamology&Visual Science*. **56(8)**, 4789-4795.

[7] Samsudin, A., Eames, I., Brocchini, S., Khaw, P.T. (2014). Evalution of dimensional and flow properties of ExPress glaucoma drainage device. *J Glaucoma.* **25(1)**, e39–e45.

[8] American Academy of Ophtalmojy. (2019). XEN Glaucoma Treatment System.https://eyewiki.aao.org/Xen_Glaucoma_Treatment_System#cite_note-treze-13. 12.06.2019.

[9] Moon, S., Im, S., An, J., Ju Park, C., Kim, H. G., Park, S. W., Kim, H. I., Lee, J.H. (2011). Selectively Bonded Polymeric Glaucoma Drainage Device for Reliable Regulation of Intraocular Pressure. *Biomed Microdevices*. **14**,325-335.

[10] DeCroos, F.C., Kondo, Y., Mordes, D., Lee, M.R., Ahmad, S., Asrani, S., Allingham, R.R., Olbrich, K.C., Klitzman, B. (2011). In Vitro Fluid Dynamics of the Ahmed Glaucoma Valve Modified with Expanded Polytetrafluoroethylene. *Current Eye Research*. **36(2),** 112-117.

[11] Maleki, T., Member, IEEE, Chitnis, G., Park, J.H., Cantor, L.B, Ziaie, B., Senior Member, IEEE. (2012). Biodegradable microfabricated plug-filters for glaucoma drainage devices. *IEEE Trans Biomed Eng*. **59(6),** 1507-13.

[12] Siewert, S., Schultze, C., Schmidt, W., Hinze, U., Chichkov, B., Wree, A., Sternberg, K., Allemann, R., Guthoff, R., Schmitz, KP. (2012). Development of a micro-mechanical valve in a novel glaucoma implant. *Biomed Microdevices*. **14(5),** 907-20.

[13] Schmidt, W., Quosdorf, D., Siewert, S., Hinze, U., Chichkov, B., Brede, M., Leder, A., Guthoff, R., Schmitz, K.-P. (2012). Micro particle-image-velocimetry for characterization of a micro-mechanical valve in a glaucoma implant. *Biomed Tech.* **57 (1**).

[14] Siewert, s., Schultze, C., Schmidt, W., Hinze, U., Schmitz, K.-P. (2010). Adaptierte biegesteifigkeit und micromechanische ventile in einem neuartigen glaukomimplantat – finite-elemente-analyse und experimentelle untersuchungen. *Biomed Tech.* **55 (Suppl. 1)**.

[15] Paschalis, El., Chodosh, J., Sperling, RA., Salvador-Culia, B., Dohlman, C., (2013). A novel implantable glaucoma valve using ferrofluid. *PLoS ONE.* **8(6),** e67404.

[16] Luong, Q.M., Shang, L., Kong, J.F., Peng, Y., Wong, T.T., Venkatraman, S.S. (2013). A new design and application of bioelastomers for beter control of intraocular pressure in a glaucoma drainage device. *Adv Healthc Mater.* **3(2),** 205-13.

[17] Villamarin, A., Roy, S., Bigler, S., Stergiopulos, N., (2014). A new adjustable glaucoma drainage device. *Investigate Ophtamology&Visual Science*. **55(3),** 1848-1852.

[18] Rosa, P., Karayiannis, T.G. and Collins, M.W., 2009. Single-phase heat transfer in microchannels: The importance of scaling effects. *Appl. Therm. Eng.* **29**, 3447-3468.

[19] University of Virginia. (2019). Physics of Human Body. http://galileo.phys.virginia.edu/classes/304/h2o.pdf. 10.04.2018

[20] Fluid Mechanics; Douglas J.F., 2011.

[21] Aksel H. (2003). Fluid Mechanics Textbook. Vol 1. (3rd ed.).

[22] Prata, J.A., MD, Mermoud, A., MD, LaBree, L., MS, Minckler, D.S., MD, (1994). In vitro and in vivo flow characteristic of glaucoma drainage implants.*Ophthalmology.* **102,** 894-904.

[23] Estermann, S., Yuttitham, K., MD, Chen, J.A., MD, Lee, O., BA, Stamper R.L. (2013). Comparative in vitro flow study of 3 different Ex-Press miniature glaucoma device models. *J Glaucoma.* **22,** 209–214.

[24] Samsudin, A., Eames, I., Brocchini, S., Khaw, P.T. (2014). Evalution of dimensional and flow properties of ExPress glaucoma drainage device. *J Glaucoma.* **25,** e39–e45.

[25] FLUENT Inc., editor. FLUENT 6.3 Documentation: User's guide. FLUENT Inc., Lebanon, 2003.

[26] Tan, SZ., Walkden, A., Au, L. (2018). One year results of XEN implant for glaucoma: efficacy, safety and postoperative management. *Eye.* **32,** 324–332.

APPENDIX A

POSTPROCESSING OF AGV

1.6 µl/min

Sample Fluent Summary Report File:

```
Fluent

Version: 3d, dp, pbns, dynamesh, lam, transient (3d, double
precision, pressure-based, dynamic mesh, laminar, transient)

Release: 18.2.0

Title:


Models

------

   Model                         Settings
   ------------------------------------------------------------
   Space                         3D
   Time                          Unsteady, 1st-Order Implicit
   Viscous                       Laminar
   Heat Transfer                 Disabled
   Solidification and Melting    Disabled
   Species                       Disabled
   Coupled Dispersed Phase       Disabled
   NOx Pollutants                Disabled
   SOx Pollutants                Disabled
   Soot                          Disabled
   Mercury Pollutants            Disabled


Material Properties

-------------------


   Material: water-liquid (fluid)


      Property                        Units     Method     Value(s)
```

Property	Units	Method	Value(s)
Density	kg/m3	constant	998.2
Cp (Specific Heat)	j/kg-k	constant	4182
Thermal Conductivity	w/m-k	constant	0.6
Viscosity	kg/m-s	constant	0.001003
Molecular Weight	kg/kmol	constant	18.0152
Thermal Expansion Coefficient	1/k	constant	0
Speed of Sound	m/s	none	#f

Material: air (fluid)

Property	Units	Method	Value(s)
Density	kg/m3	constant	1.225
Cp (Specific Heat)	j/kg-k	constant	1006.43
Thermal Conductivity	w/m-k	constant	0.0242
Viscosity	kg/m-s	constant	1.7894e-05
Molecular Weight	kg/kmol	constant	28.966
Thermal Expansion Coefficient	1/k	constant	0
Speed of Sound	m/s	none	#f

Material: aluminum (solid)

Property	Units	Method	Value(s)
Density	kg/m3	constant	2719
Cp (Specific Heat)	j/kg-k	constant	871
Thermal Conductivity	w/m-k	constant	202.4

Cell Zone Conditions

```
--------------------

   Zones

      name         id   type
      ----------------------
      reservoir    8    fluid
      pipe         9    fluid
      porous       10   fluid

   Setup Conditions

      reservoir

         Condition       Value
         ---------------------
         Frame Motion?   no
         Mesh Motion?    no

      pipe

         Condition       Value
         ---------------------
         Frame Motion?   no
         Mesh Motion?    no

      porous

         Condition                                  Value
         ------------------------------------------------------
```

Frame Motion?	no
Mesh Motion?	no
Porous zone?	yes
Direction-1 Viscous Resistance (1/m2)	2.0344e+12
Direction-2 Viscous Resistance (1/m2)	2.0344e+12
Direction-3 Viscous Resistance (1/m2)	2.0344e+12
Direction-1 Inertial Resistance (1/m)	-1.4928933e+10
Direction-2 Inertial Resistance (1/m)	-1.4928933e+10
Direction-3 Inertial Resistance (1/m)	-1.4928933e+10

Boundary Conditions

Zones

name	id	type
wall-24	24	wall
wall-23	23	wall
wall-21	21	wall
wall-20	20	wall
wall-reservoir	11	wall
wall-pipe	12	wall
wall-porous	13	wall
piston	14	wall
outlet	15	pressure-outlet
contact_region-src	16	interface
contact_region-trg	17	interface
contact_region_2-src	18	interface
contact_region_2-trg	19	interface

Setup Conditions

wall-24

Condition	Value
Wall Motion	0
Shear Boundary Condition	0

wall-23

Condition	Value
Wall Motion	0
Shear Boundary Condition	0

wall-21

Condition	Value
Wall Motion	0
Shear Boundary Condition	0

wall-20

Condition	Value
Wall Motion	0
Shear Boundary Condition	0

wall-reservoir

Condition	Value
Wall Motion	0
Shear Boundary Condition	0

wall-pipe

Condition	Value
Wall Motion	0
Shear Boundary Condition	0

wall-porous

Condition	Value
Wall Motion	0
Shear Boundary Condition	0

piston

Condition	Value
Wall Motion	0
Shear Boundary Condition	0

outlet

```
         Condition   Value
         -----------------

      contact_region-src

         Condition   Value
         -----------------

      contact_region-trg

         Condition   Value
         -----------------

      contact_region_2-src

         Condition   Value
         -----------------

      contact_region_2-trg

         Condition   Value
         -----------------

Solver Settings
---------------

   Equations

      Equation   Solved
      -----------------
```

Flow	yes

Numerics

Numeric	Enabled
Absolute Velocity Formulation	yes

Unsteady Calculation Parameters

Time Step (s)	1
Max. Iterations Per Time Step	3000

Relaxation

Variable	Relaxation Factor
Pressure	0.3
Density	1
Body Forces	1
Momentum	0.7

Linear Solver

Variable	Solver Type	Termination Criterion	Residual Reduction Tolerance
Pressure	F-Cycle	0.1	

X-Momentum	F-Cycle	0.1
Y-Momentum	F-Cycle	0.1
Z-Momentum	F-Cycle	0.1

Pressure-Velocity Coupling

Parameter	Value
Type	SIMPLE

Discretization Scheme

Variable	Scheme
Pressure	Second Order
Momentum	Second Order Upwind

Solution Limits

Quantity	Limit
Minimum Absolute Pressure	1
Maximum Absolute Pressure	5e+10
Minimum Temperature	1
Maximum Temperature	5000

1.6 µl/min

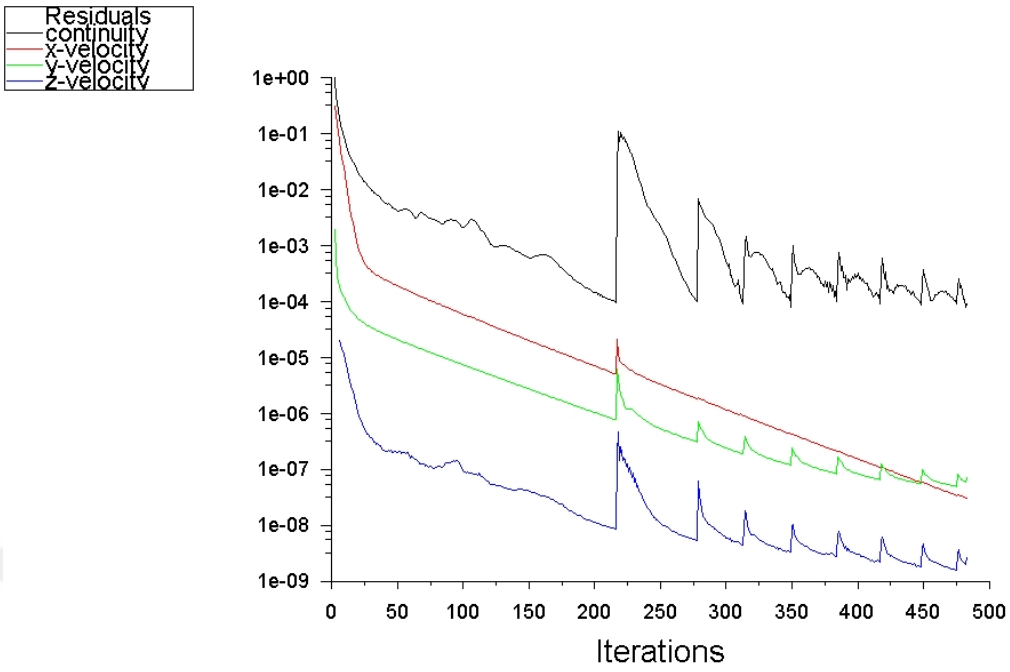

Figure A.1 Convergence results of AGV at 1.6 µl/min.

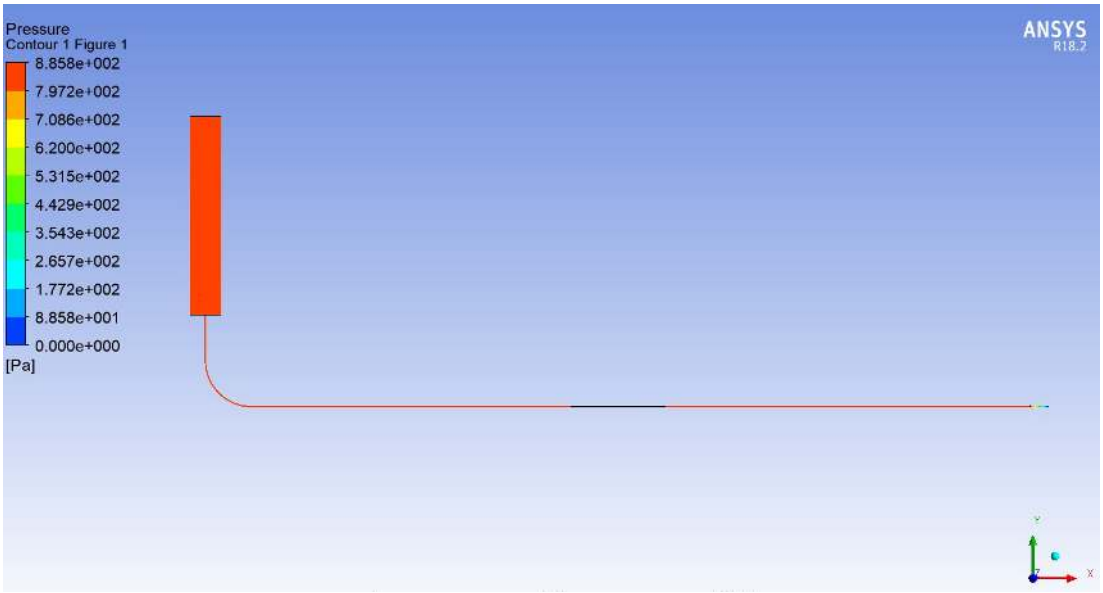

Figure A.2 Pressure drop of experimental setup at 1.6 µl/min.

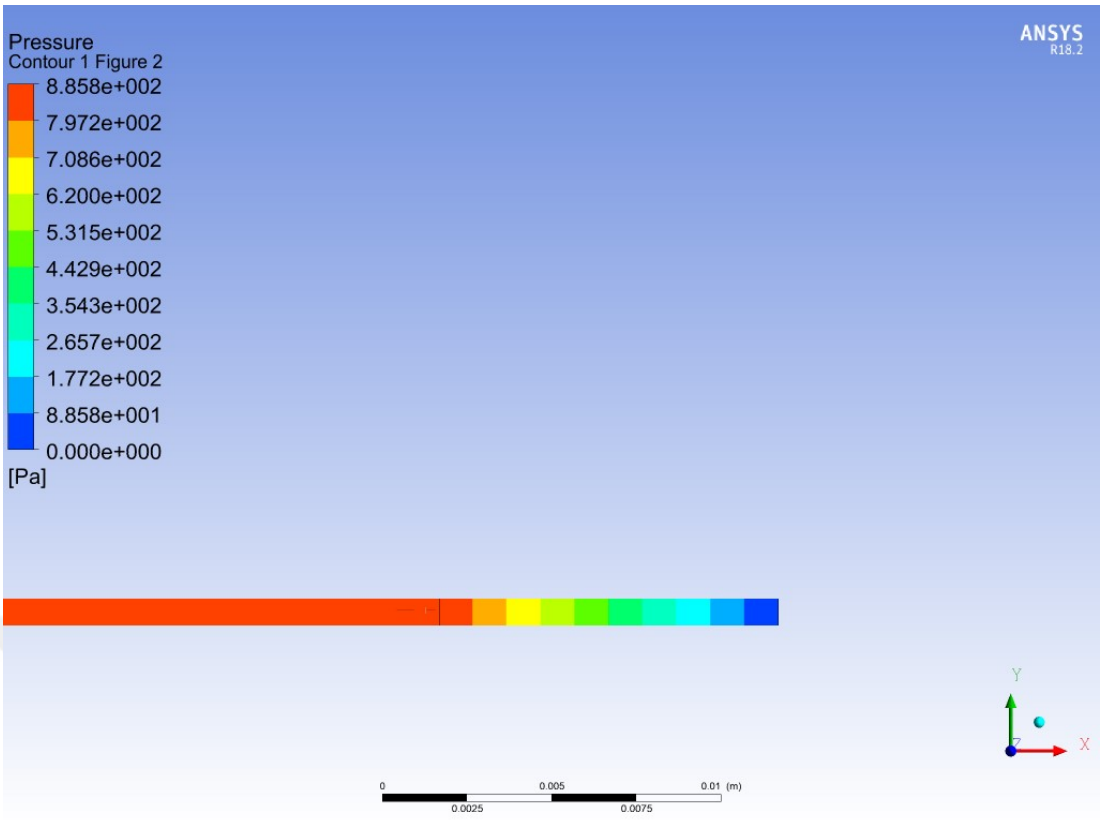

Figure A.3 Pressure drop of AGV at 1.6 µl/min.

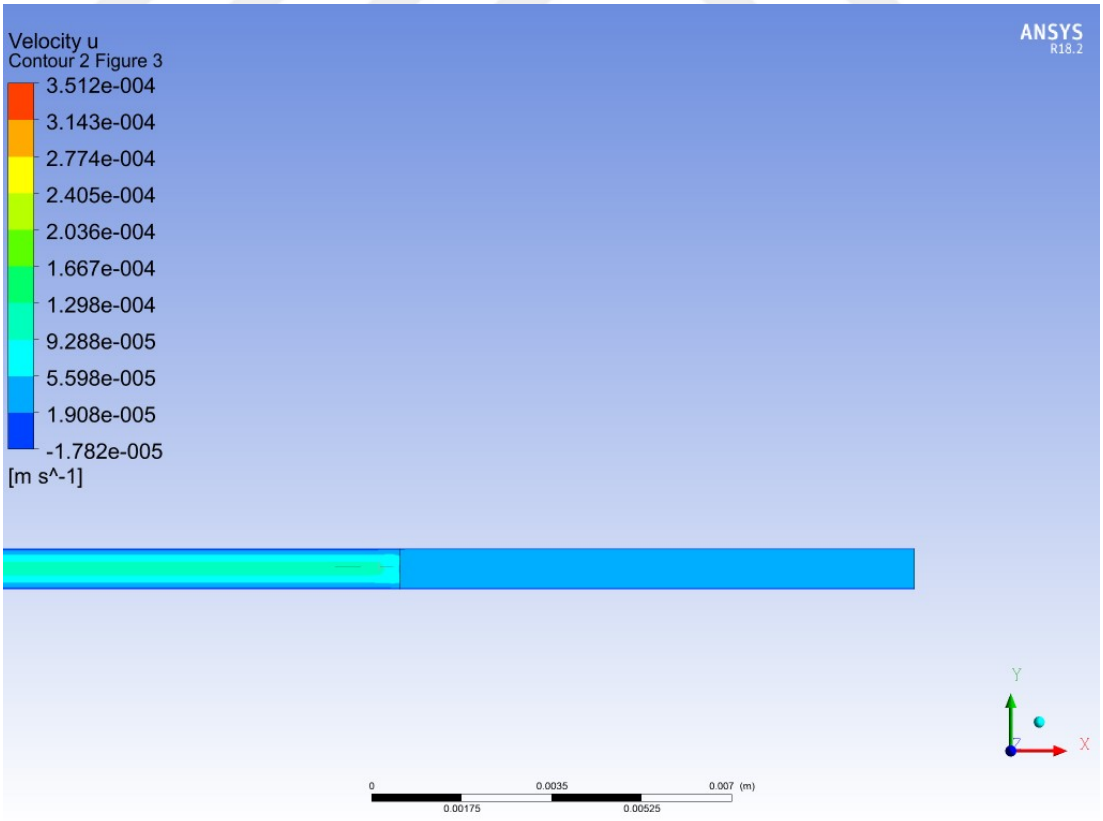

Figure A.4 Velocity contours of AGV at 1.6 µl/min.

2.5 µl/min

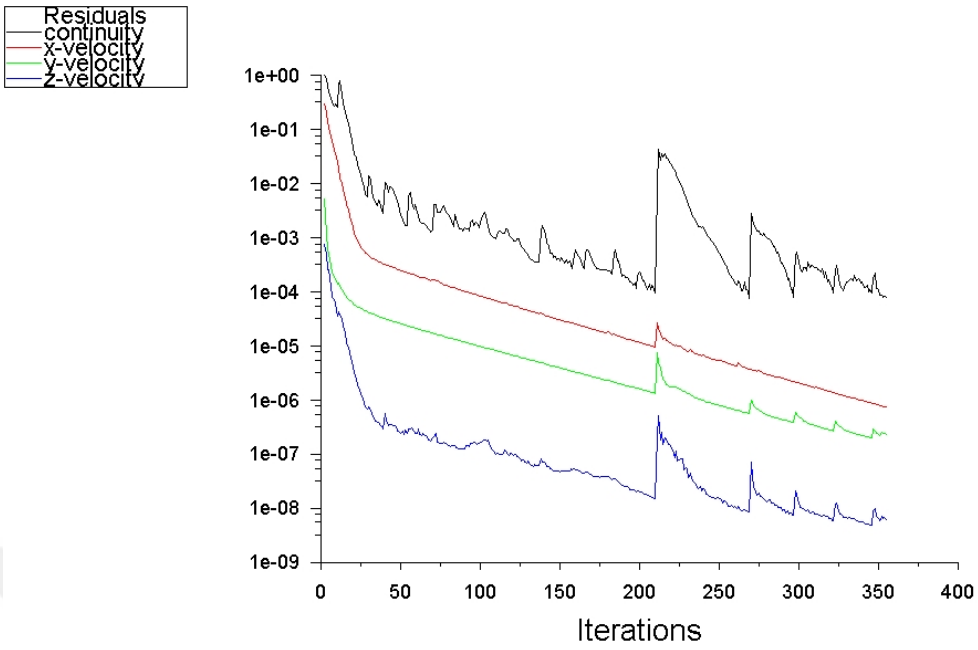

Figure A.5 Convergence results of AGV at 2.5 µl/min.

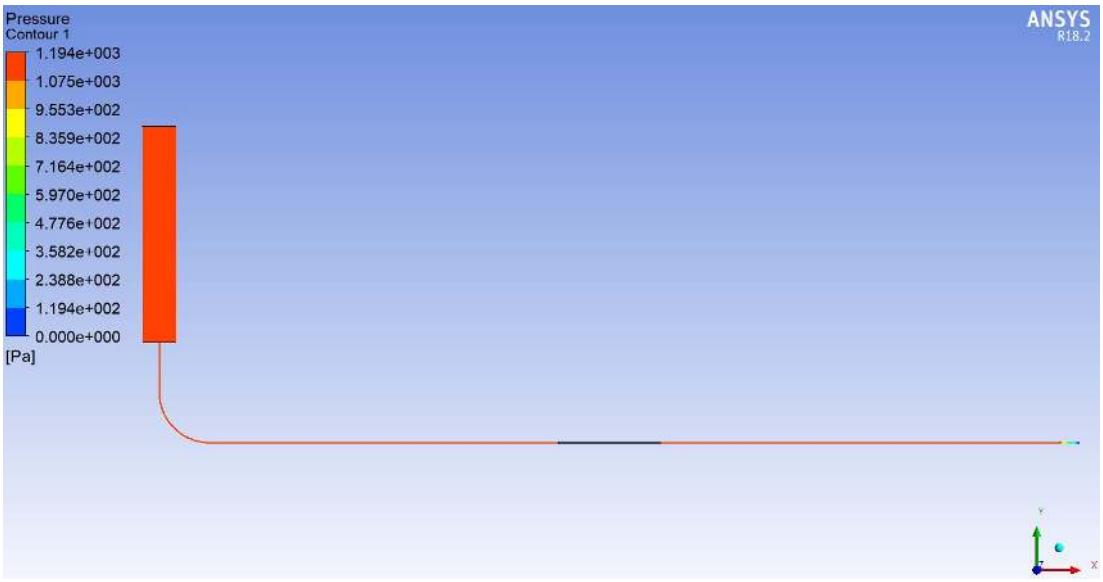

Figure A.6 Pressure drop of experimental setup at 2.5 µl/min.

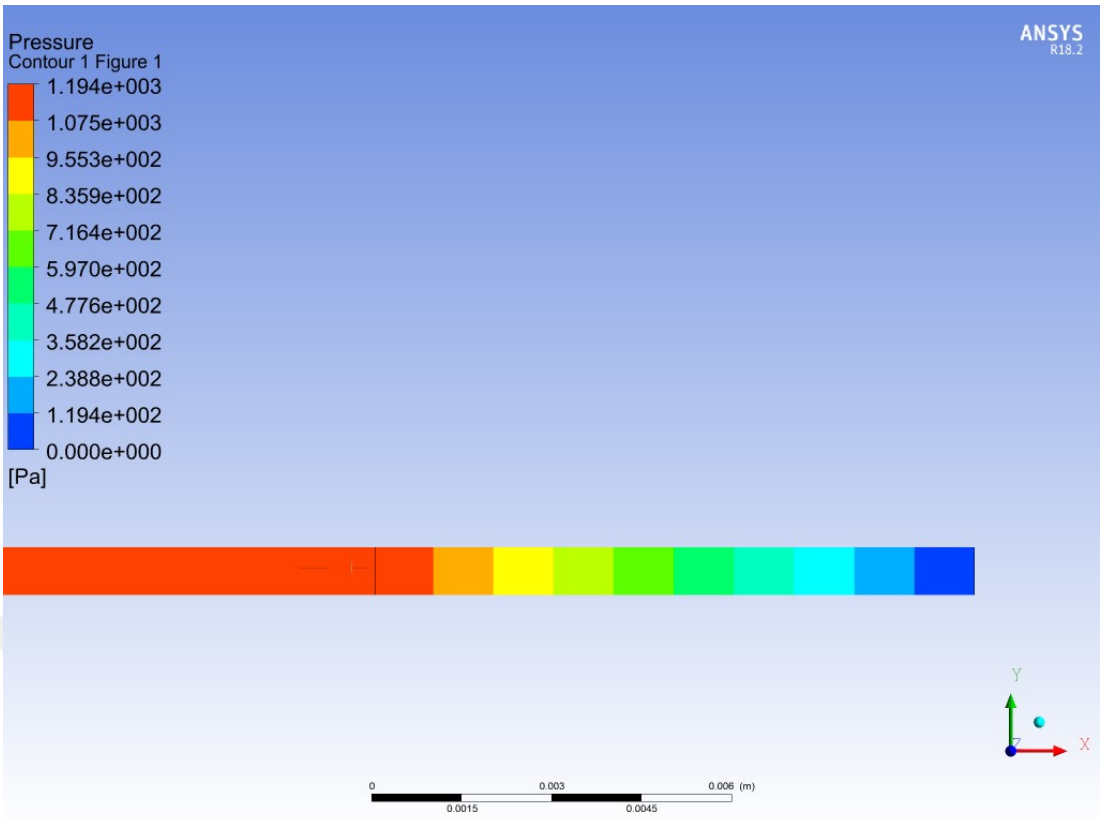

Figure A.7 Pressure drop of AGV at 2.5 µl/min.

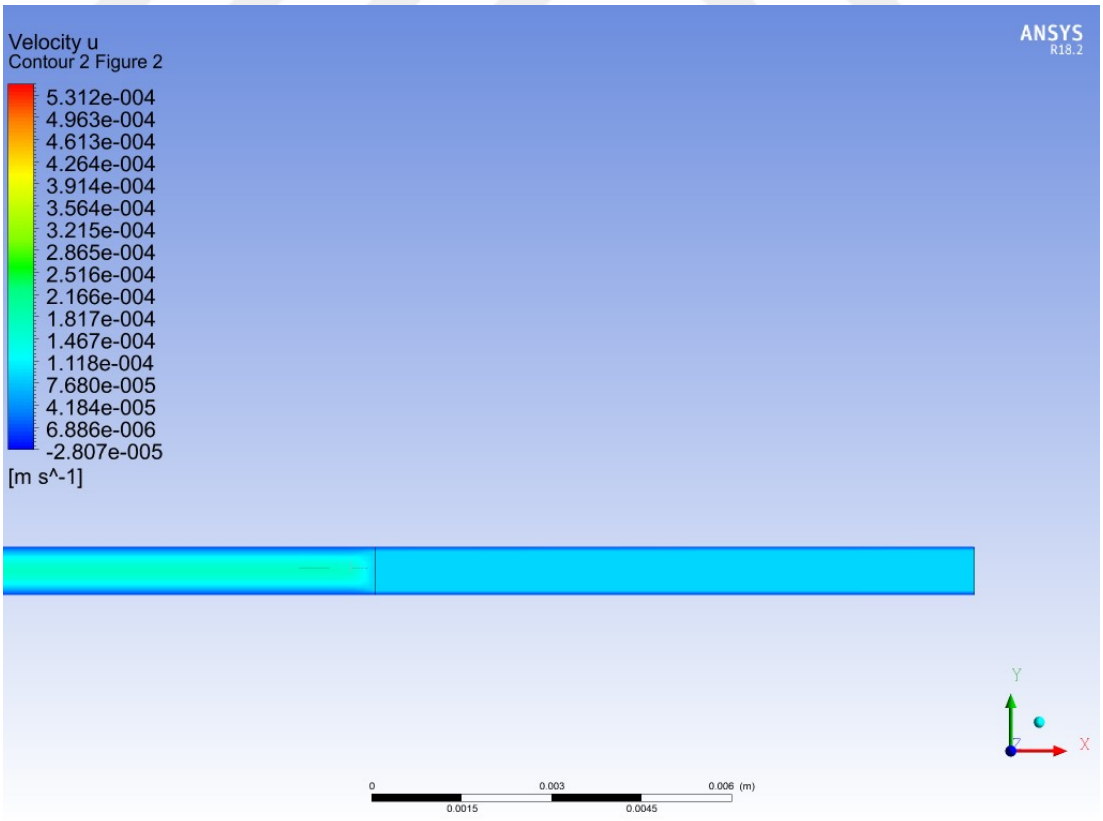

Figure A.8 Velocity contours of AGV at 2.5 µl/min.

5 µl/min

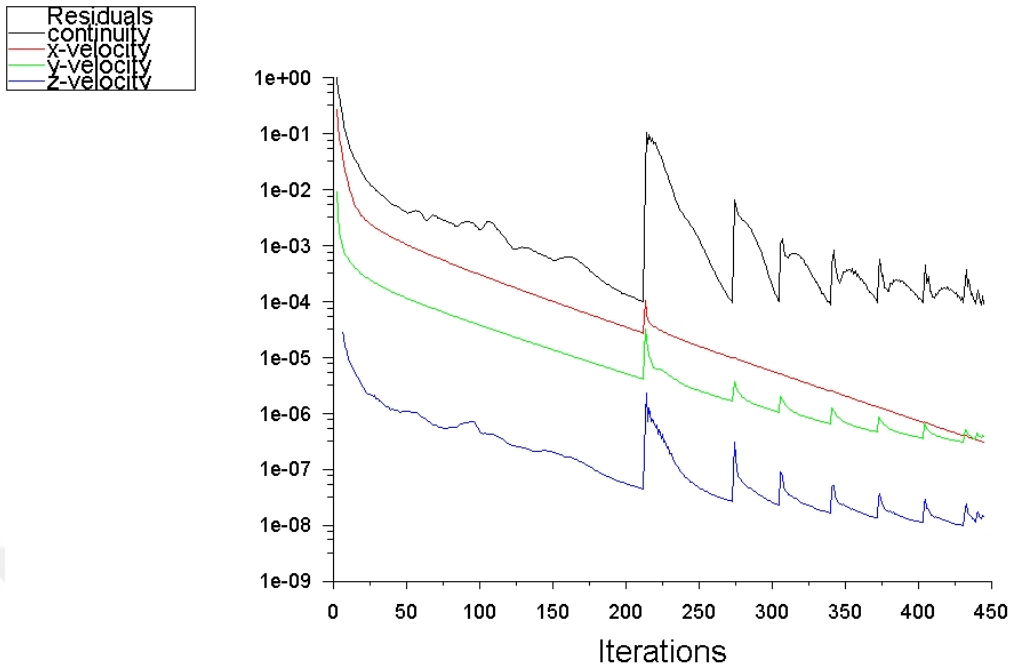

Figure A.9 Convergence results of AGV at 5 µl/min.

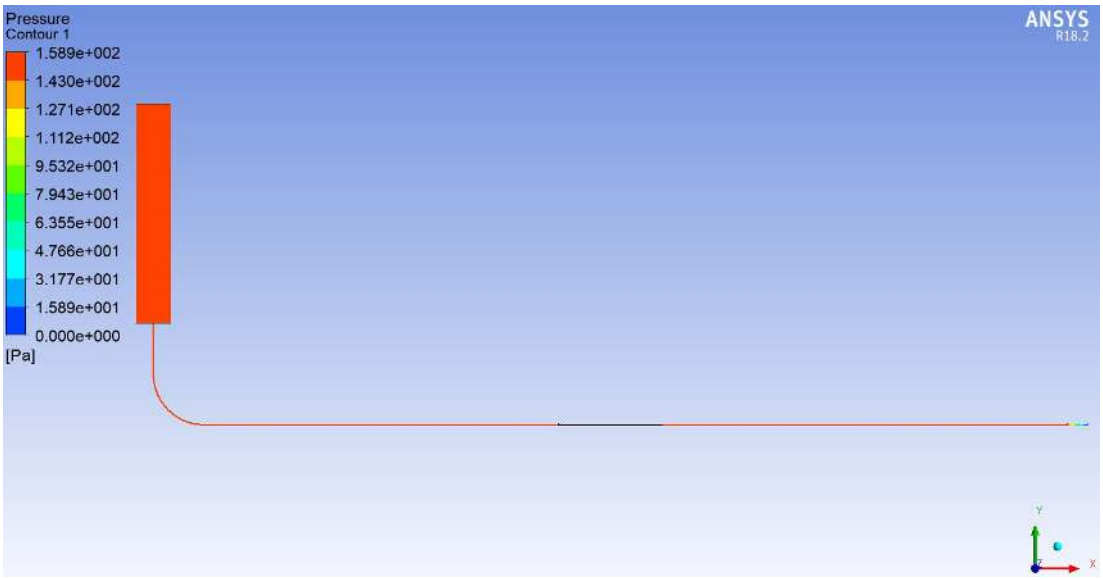

Figure A.10 Pressure drop of experimental setup at 5 µl/min.

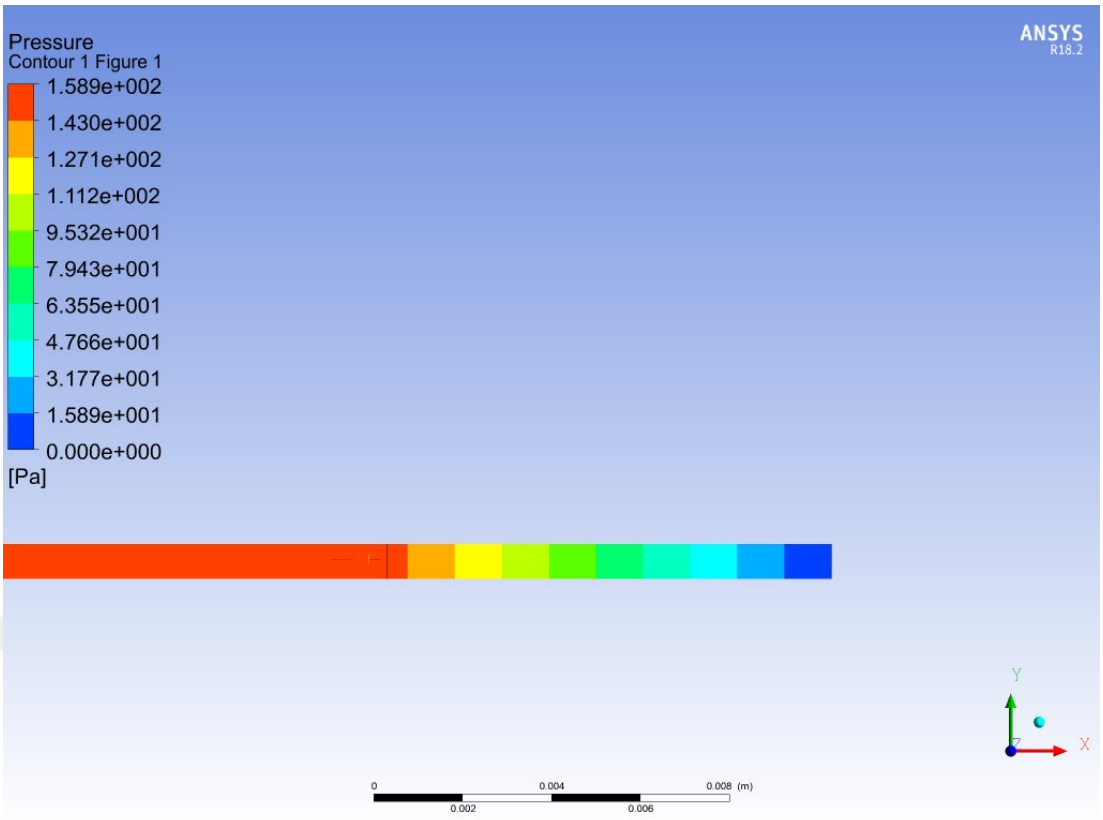

Figure A.11 Pressure drop of AGV at 5 µl/min.

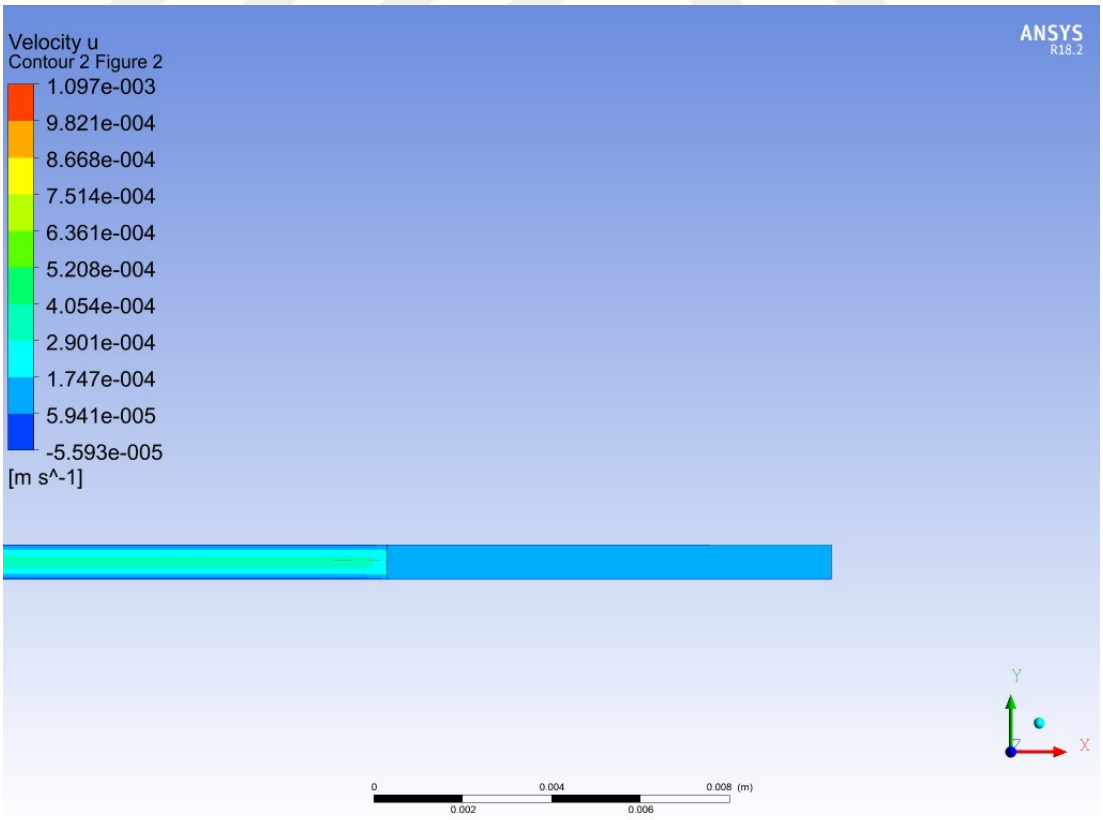

Figure A.12 Velocity contours of AGV at 5 µl/min.

10 µl/min

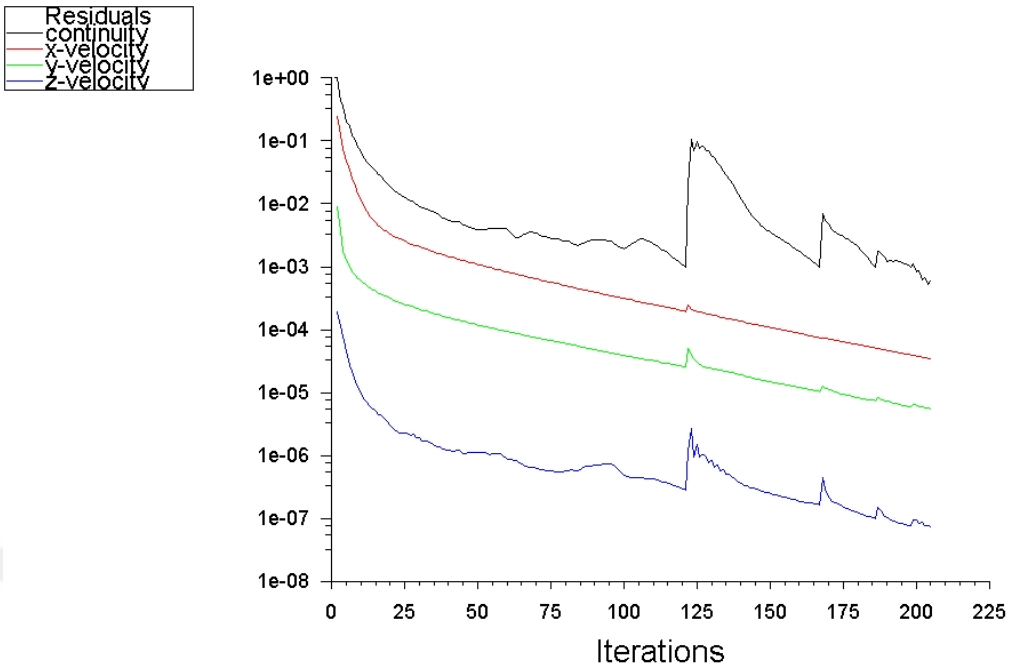

Figure A.13 Convergence results of AGV at 10 µl/min.

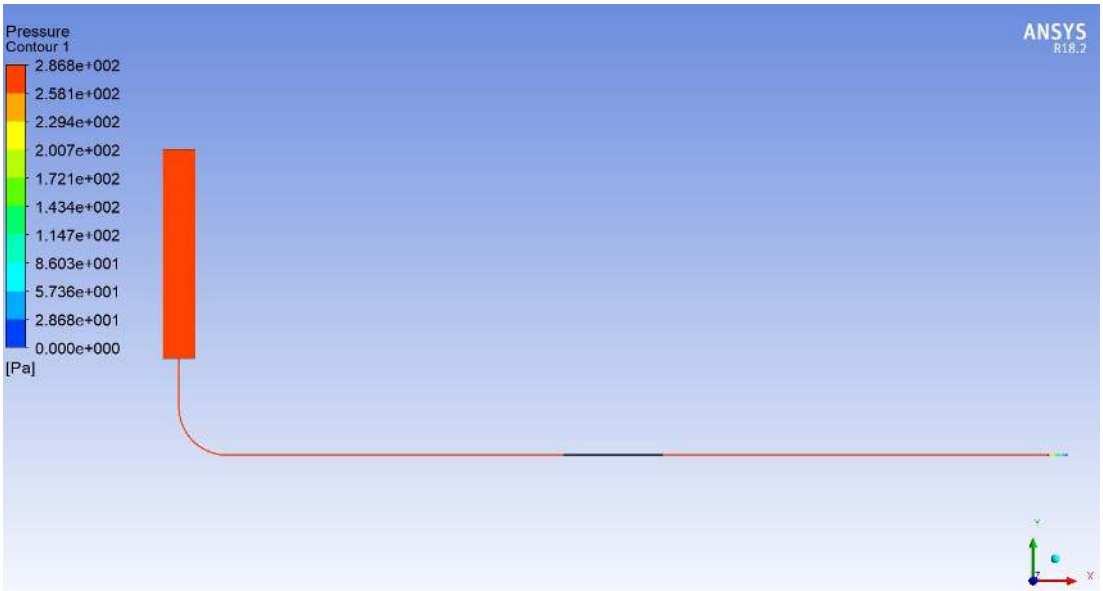

Figure A.14 Pressure drop of experimental setup at 10 µl/min.

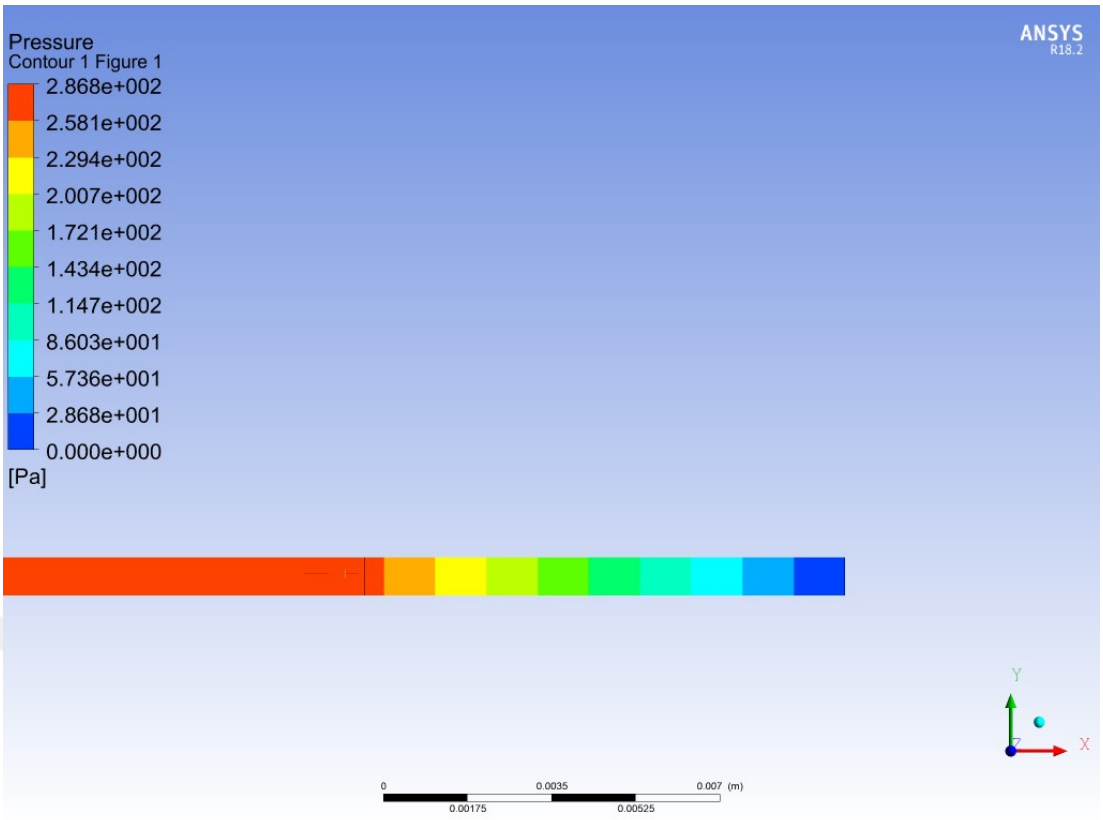

Figure A.15 Pressure drop of AGV at 10 µl/min.

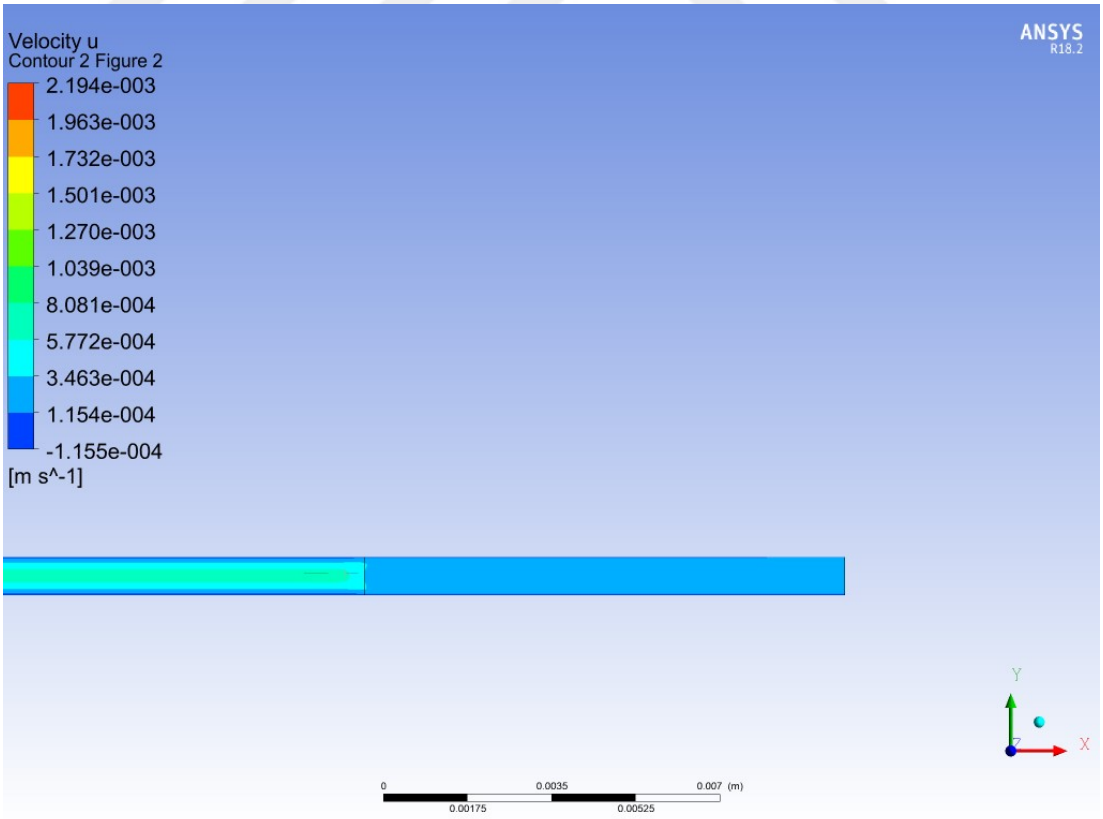

Figure A.16 Velocity contours of AGV at 10 µl/min.

20 µl/min

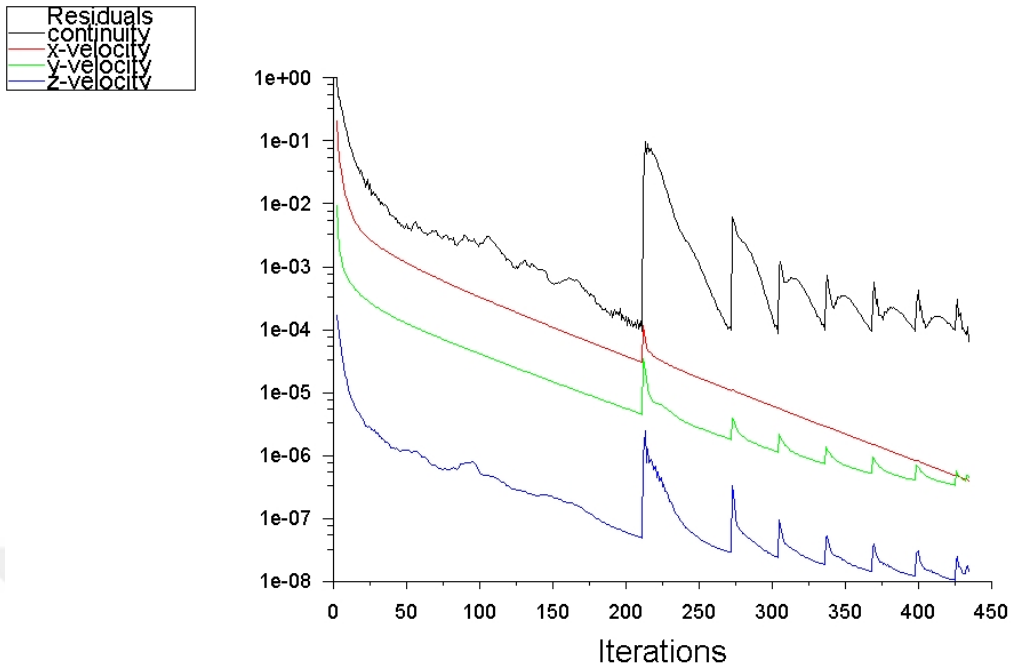

Figure A.17 Convergence results of AGV at 20 µl/min.

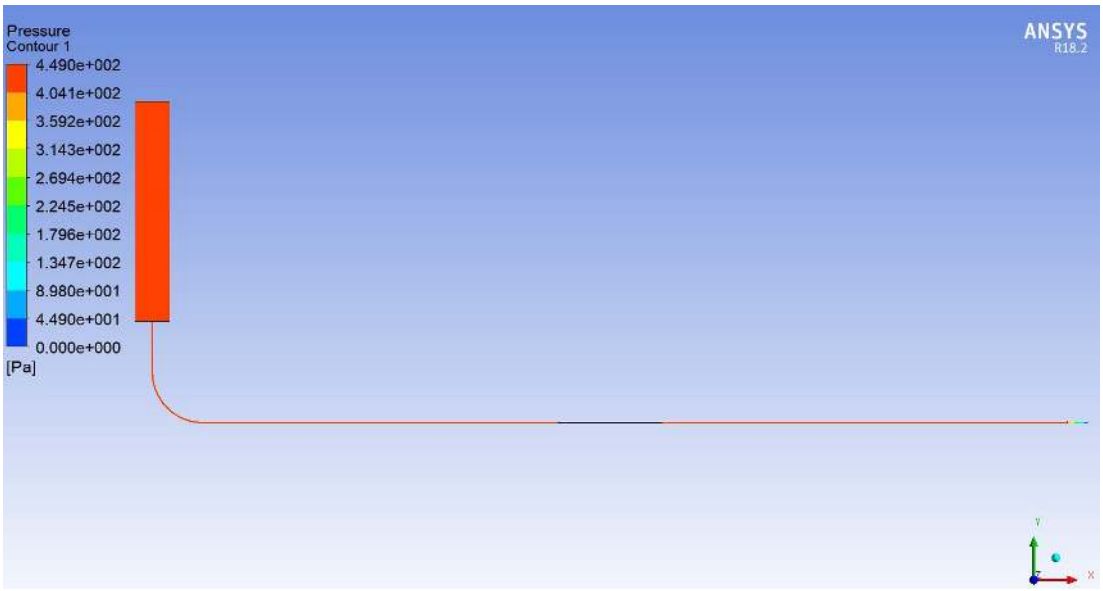

Figure A.18 Pressure drop of experimental setup at 20 µl/min.

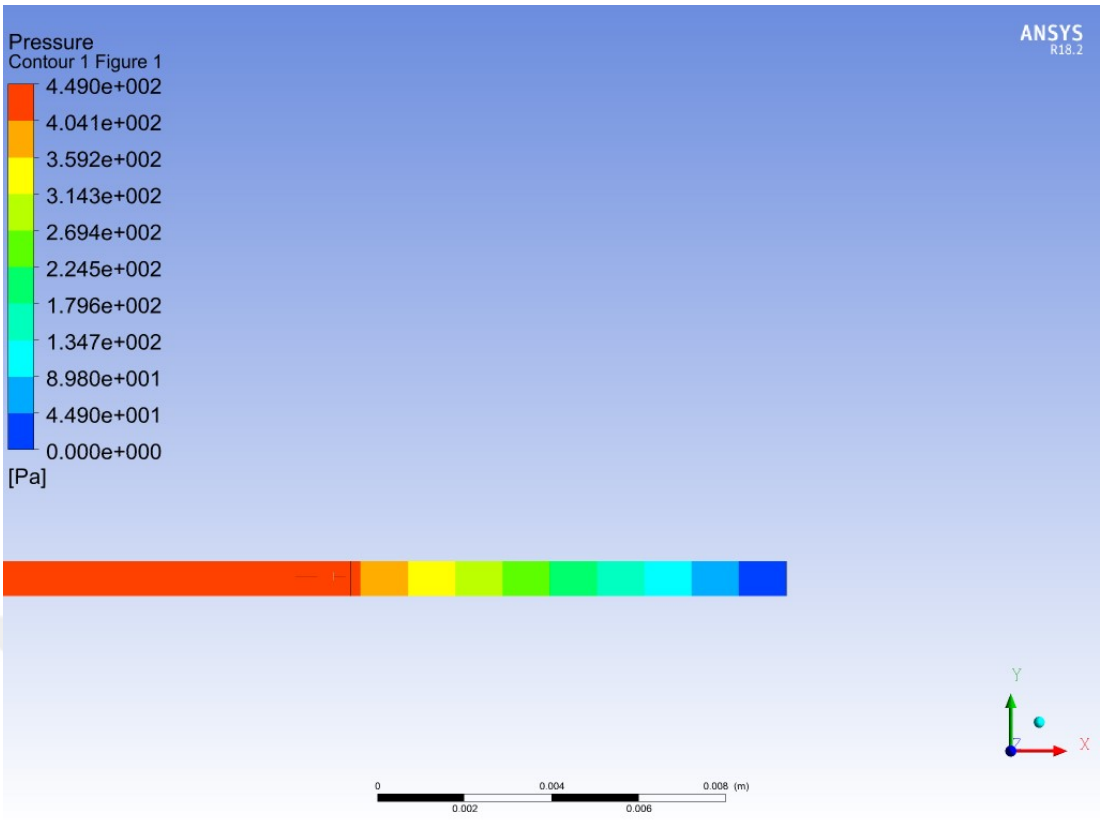

Figure A.19 Pressure drop of AGV at 20 µl/min.

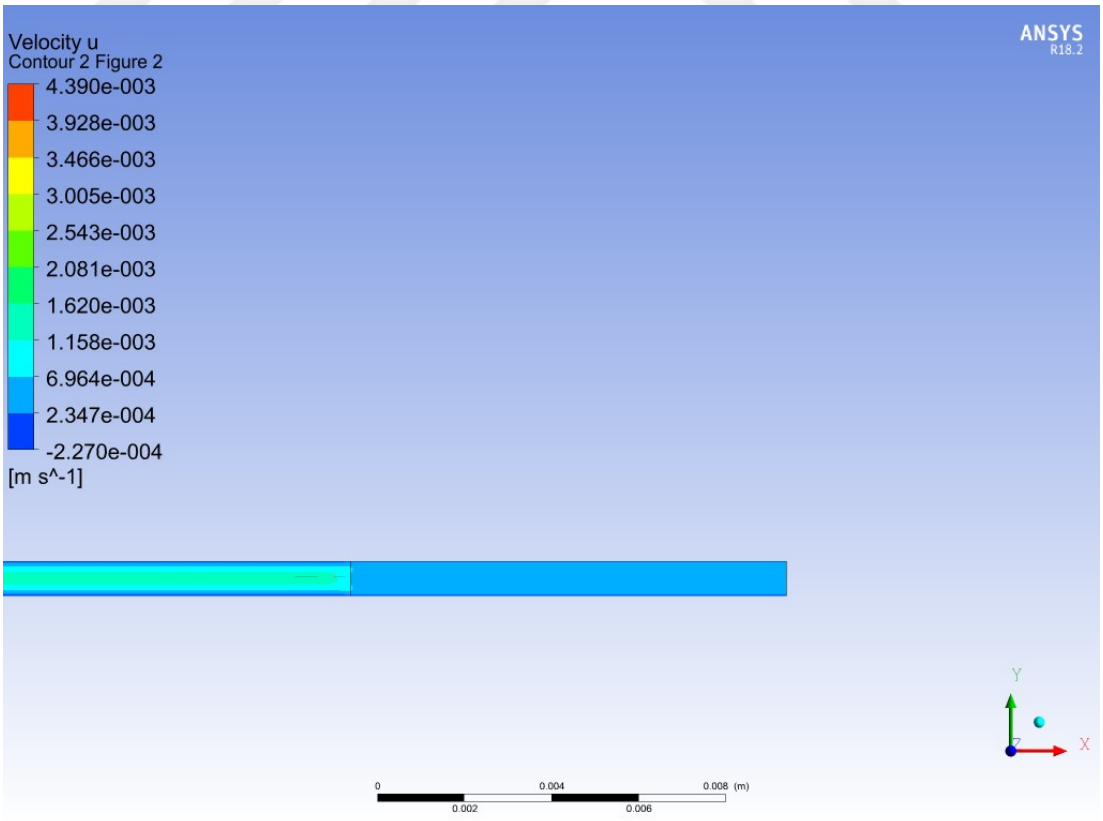

Figure A.20 Velocity contours of AGV at 20 µl/min.

25 µl/min

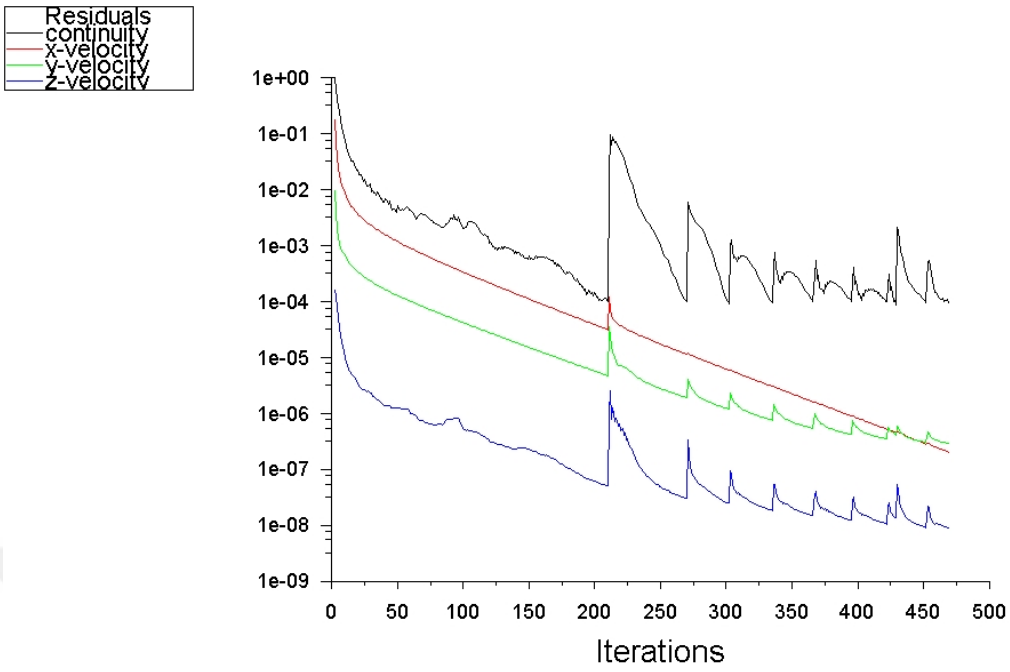

Figure A.21 Convergence results of AGV at 25 µl/min.

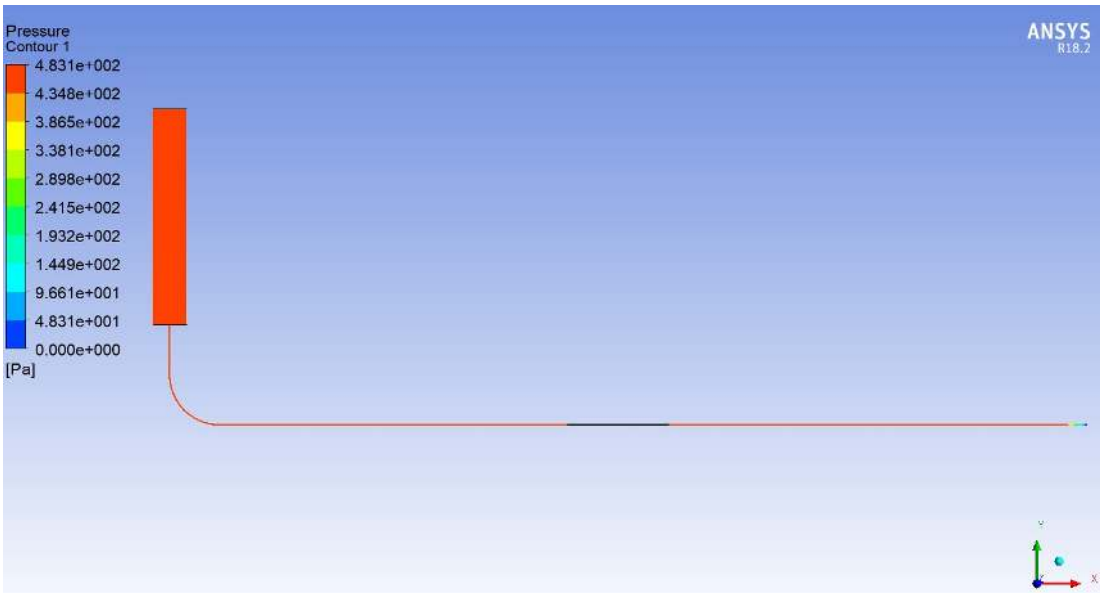

Figure A.22 Pressure drop of experimental setup at 25 µl/min.

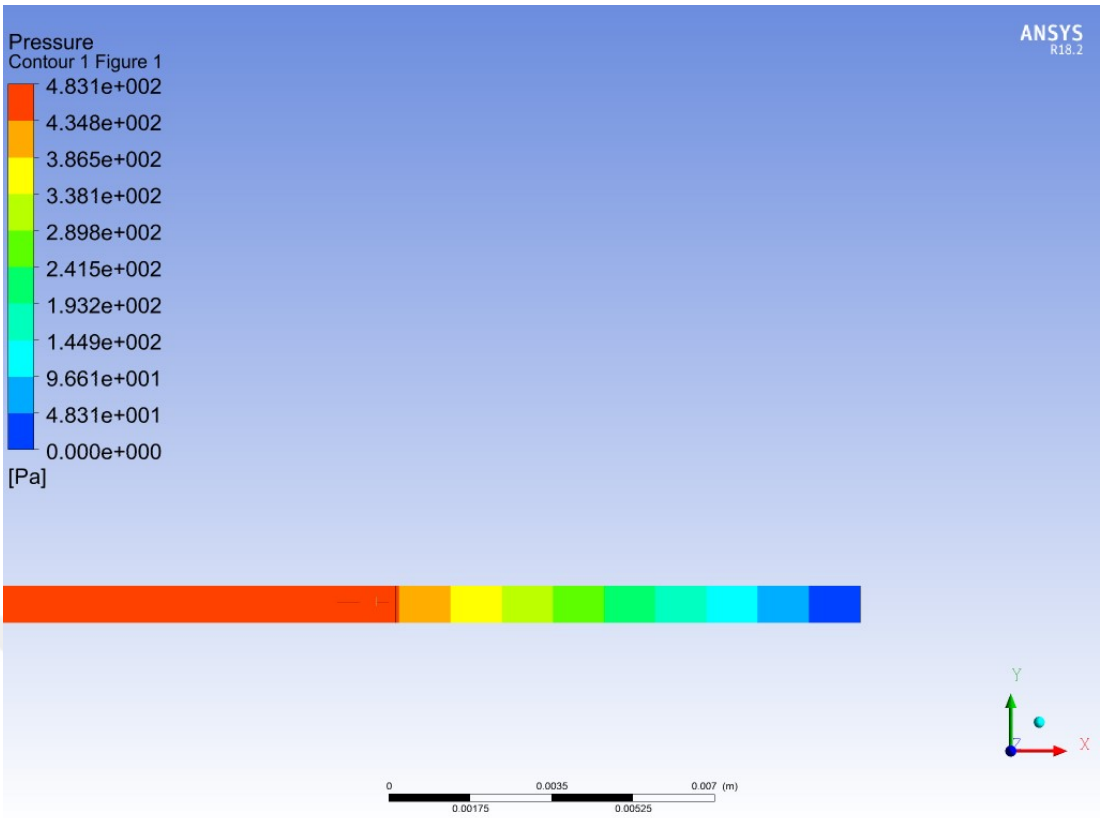

Figure A.23 Pressure drop of AGV at 25 µl/min.

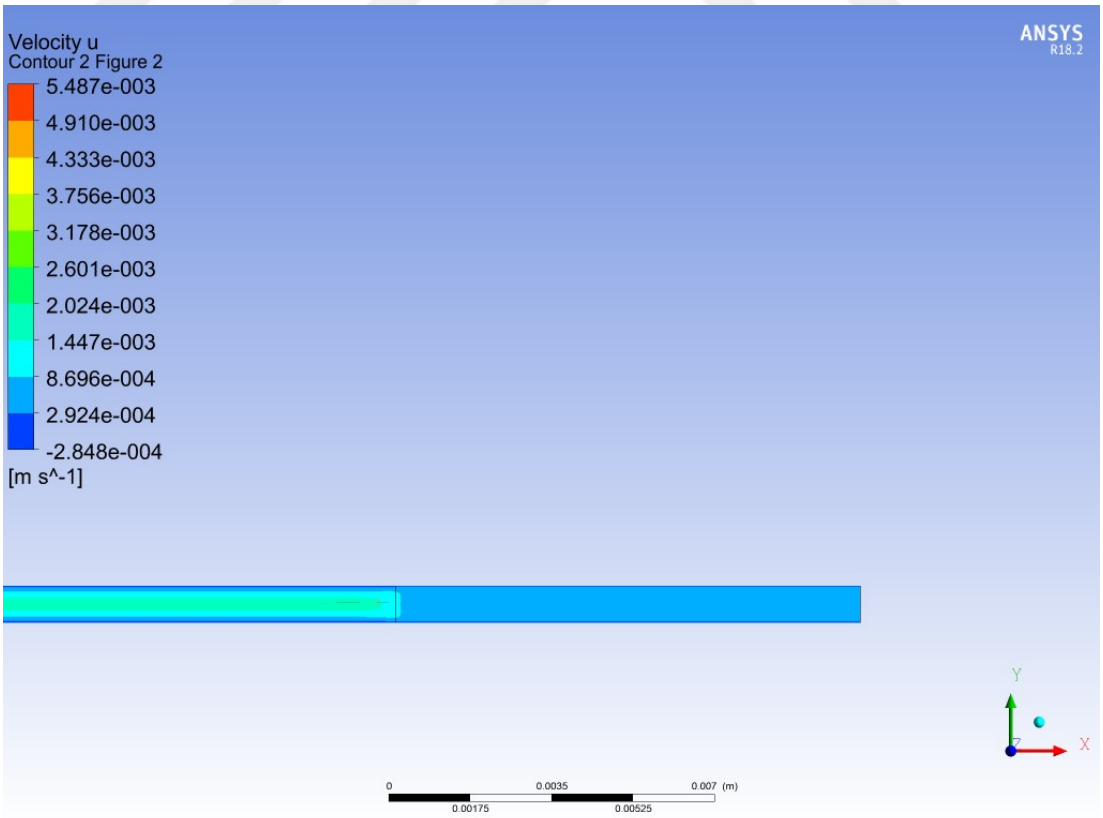

Figure A.24 Velocity contours of AGV at 25 µl/min.

APPENDIX B

POSTPROCESSING OF SINGLE PLATE MOLTENO DEVICE

5 mmHg

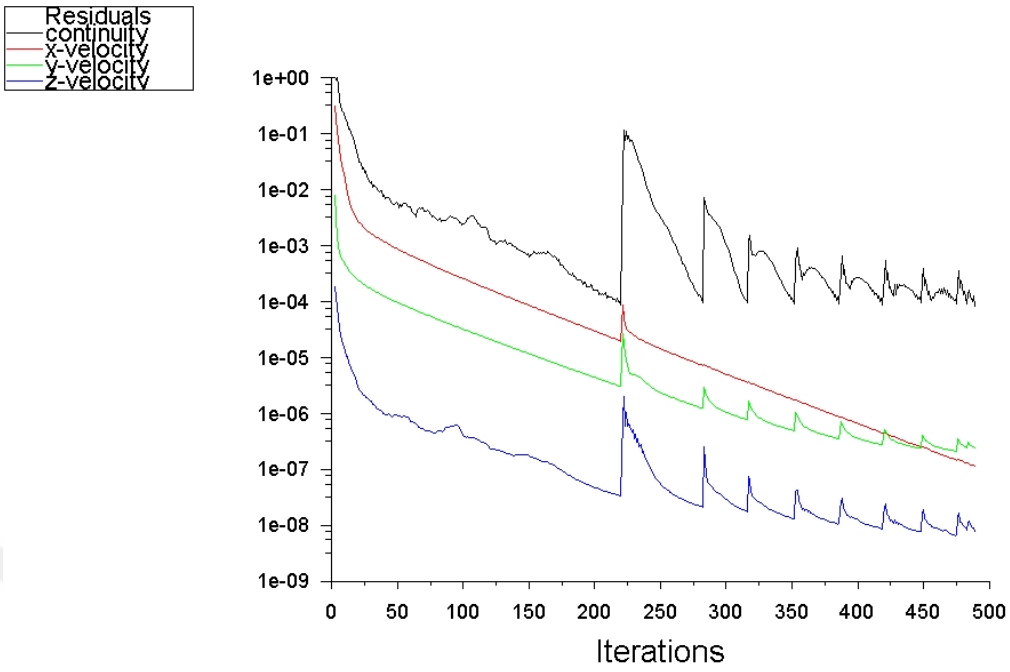

Figure B.1 Convergence results of single plate Molteno device at 5 mmHg.

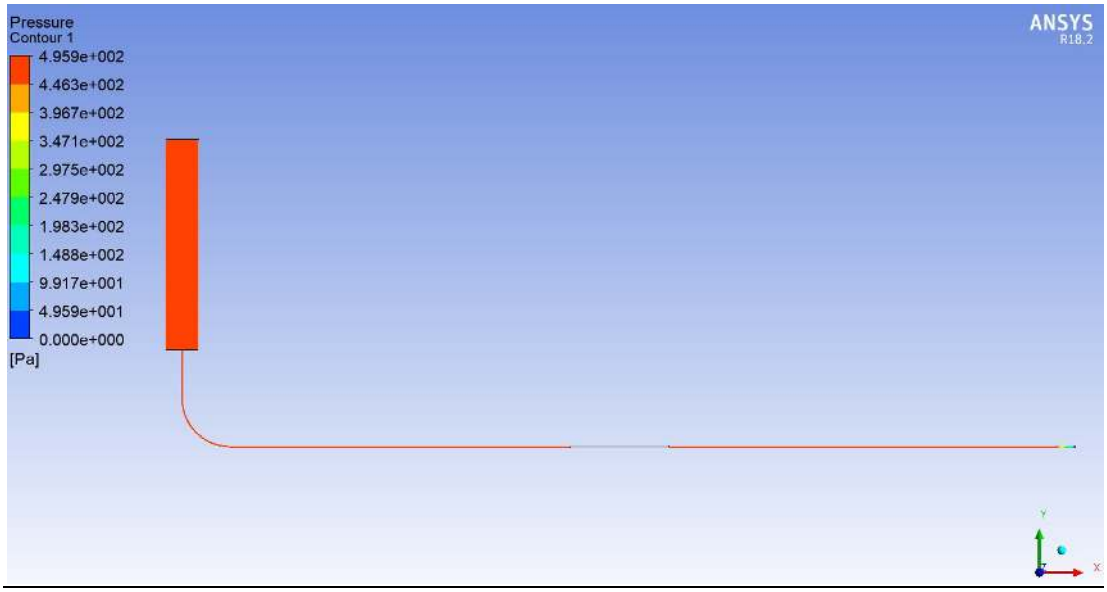

Figure B.2 Pressure drop of experimental setup at 5 mmHg.

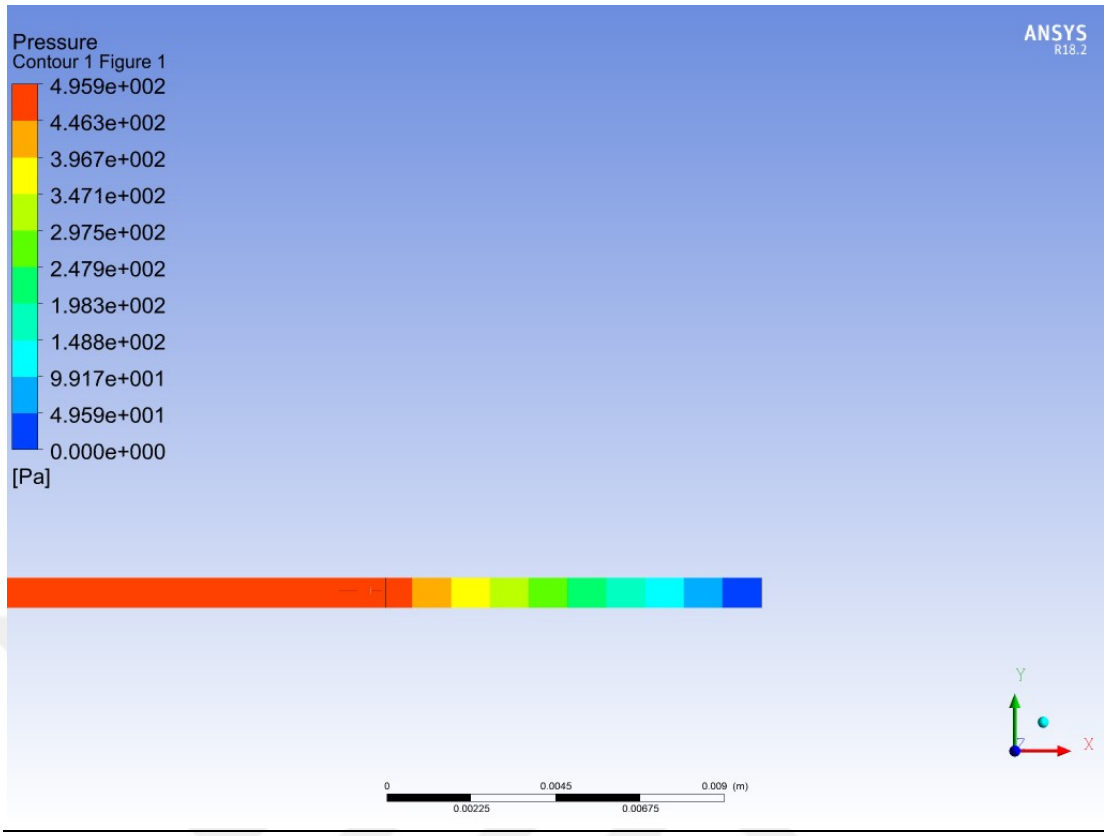

Figure B.3 Pressure drop of single plate Molteno device at 5 mmHg.

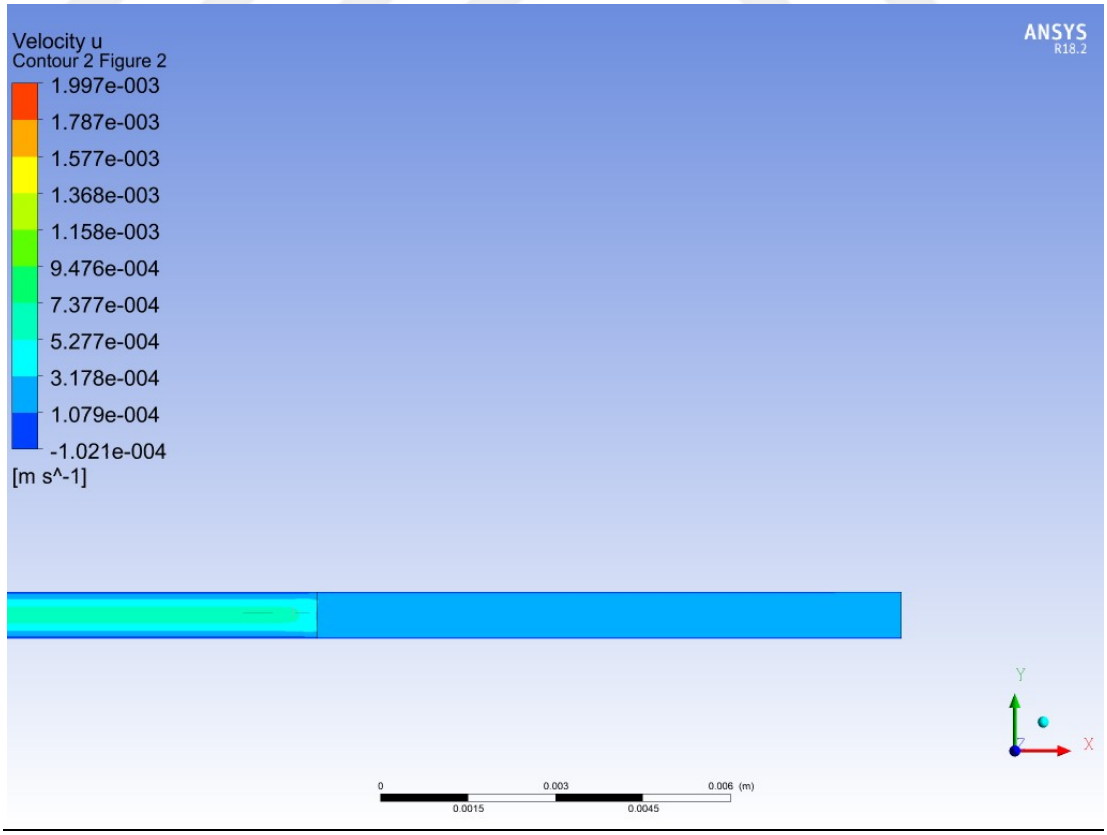

Figure B.4 Velocity contours of single plate Molteno device at 5 mmHg.

10 mmHg

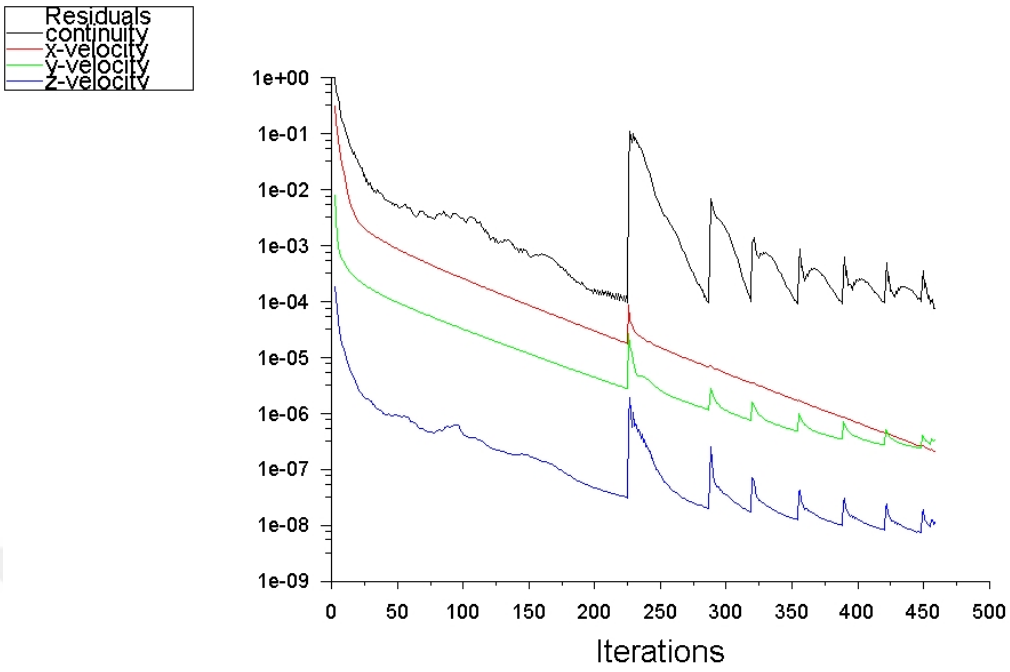

Figure B.5 Convergence results of single plate Molteno device at 10 mmHg.

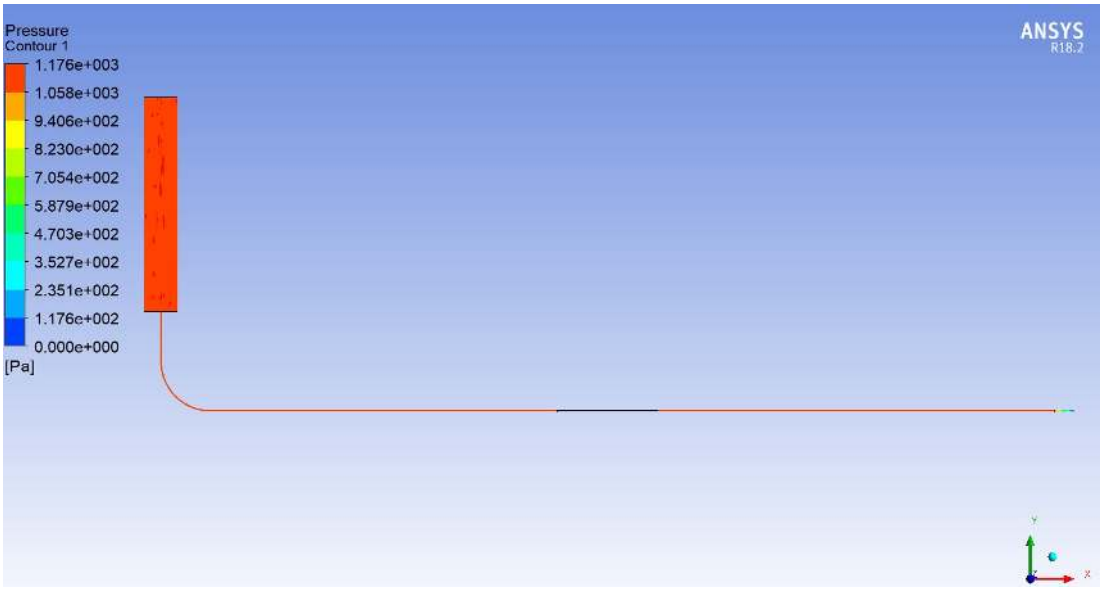

Figure B.6 Pressure drop of experimental setup at 10 mmHg.

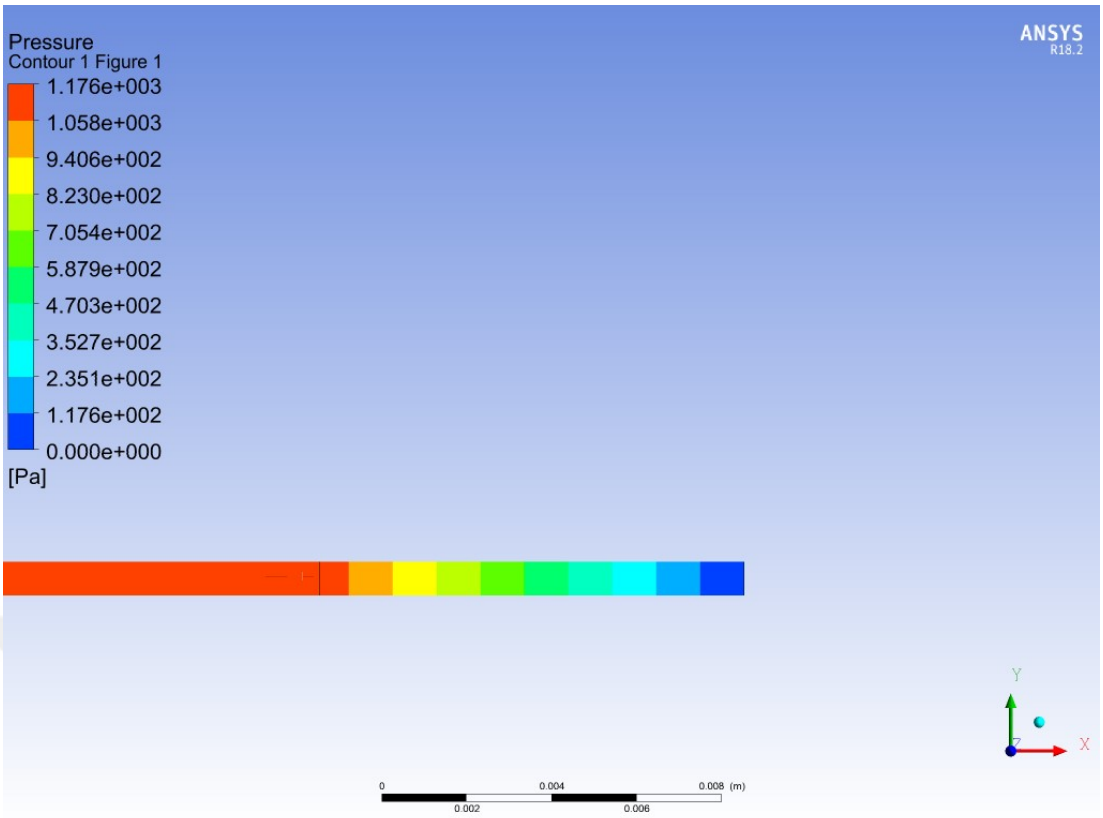

Figure B.7 Pressure drop of single plate Molteno device at 10 mmHg.

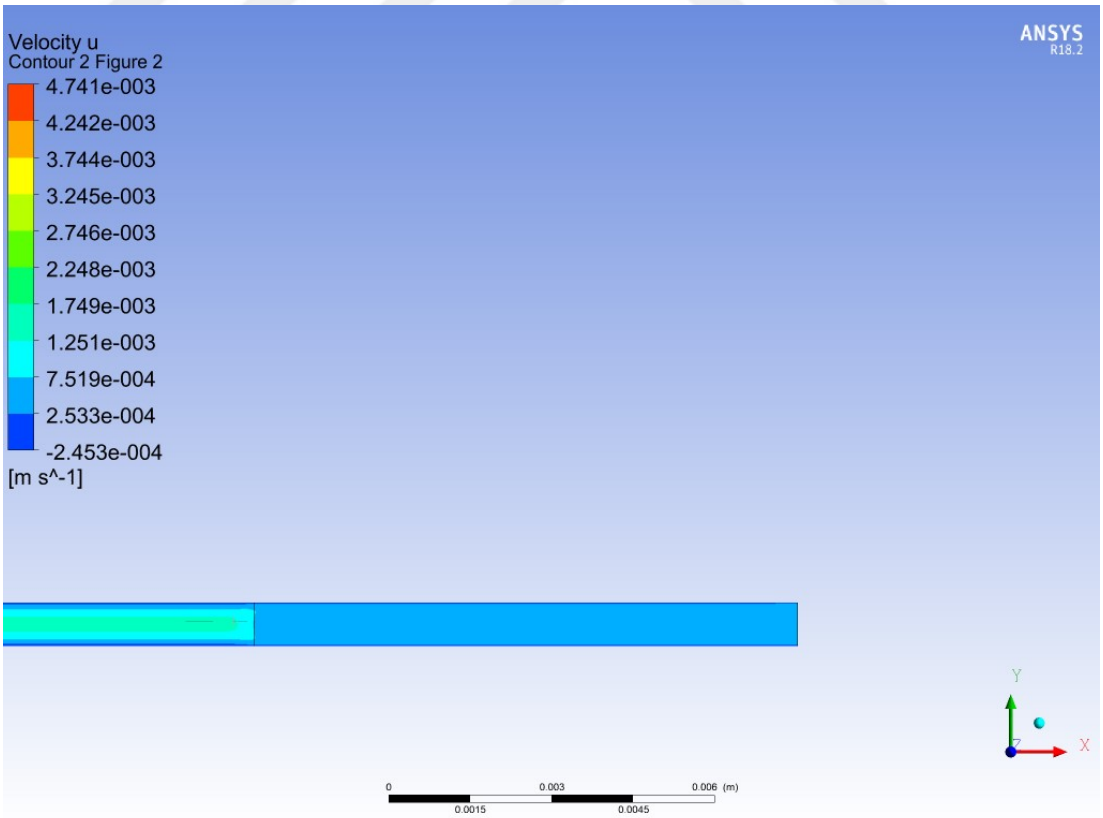

Figure B.8 Velocity contours of single plate Molteno device at 10 mmHg.

15 mmHg

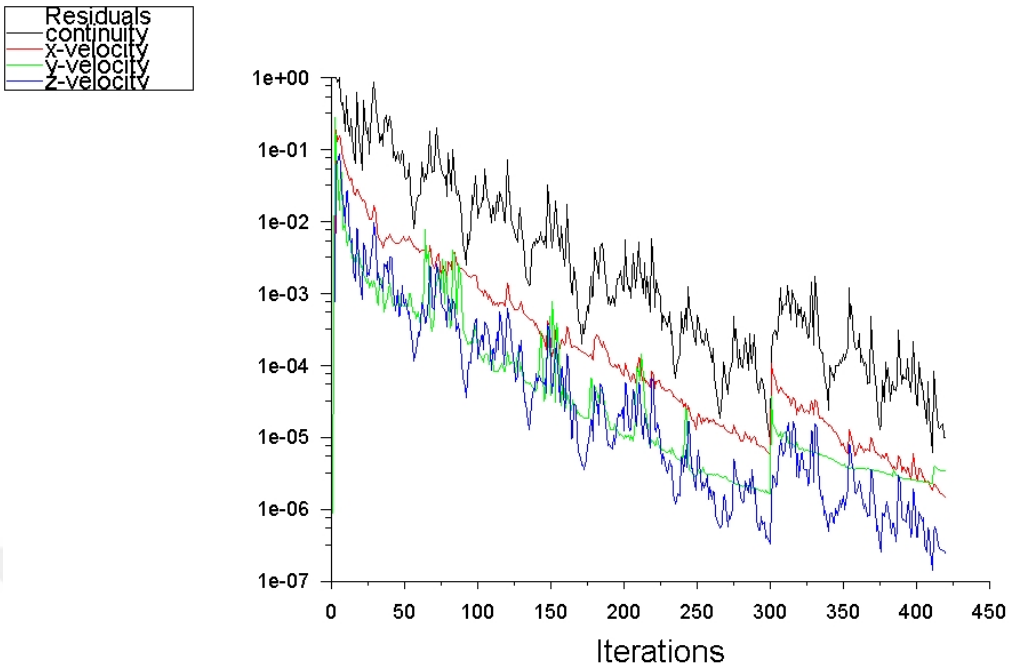

Figure B.9 Convergence results of single plate Molteno device at 15 mmHg.

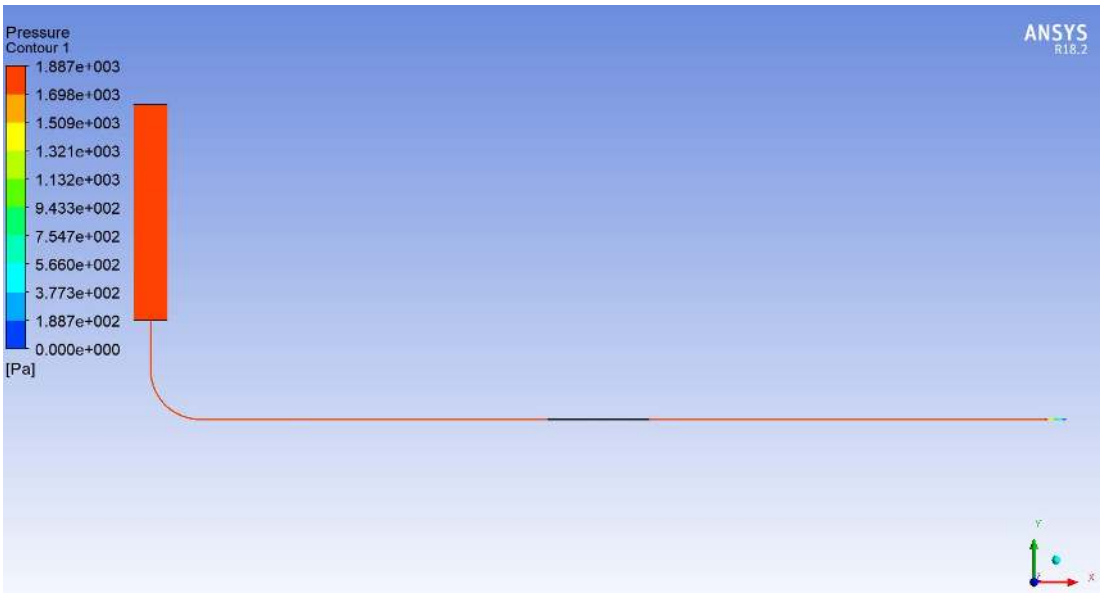

Figure B.10 Pressure drop of experimental setup at 15 mmHg.

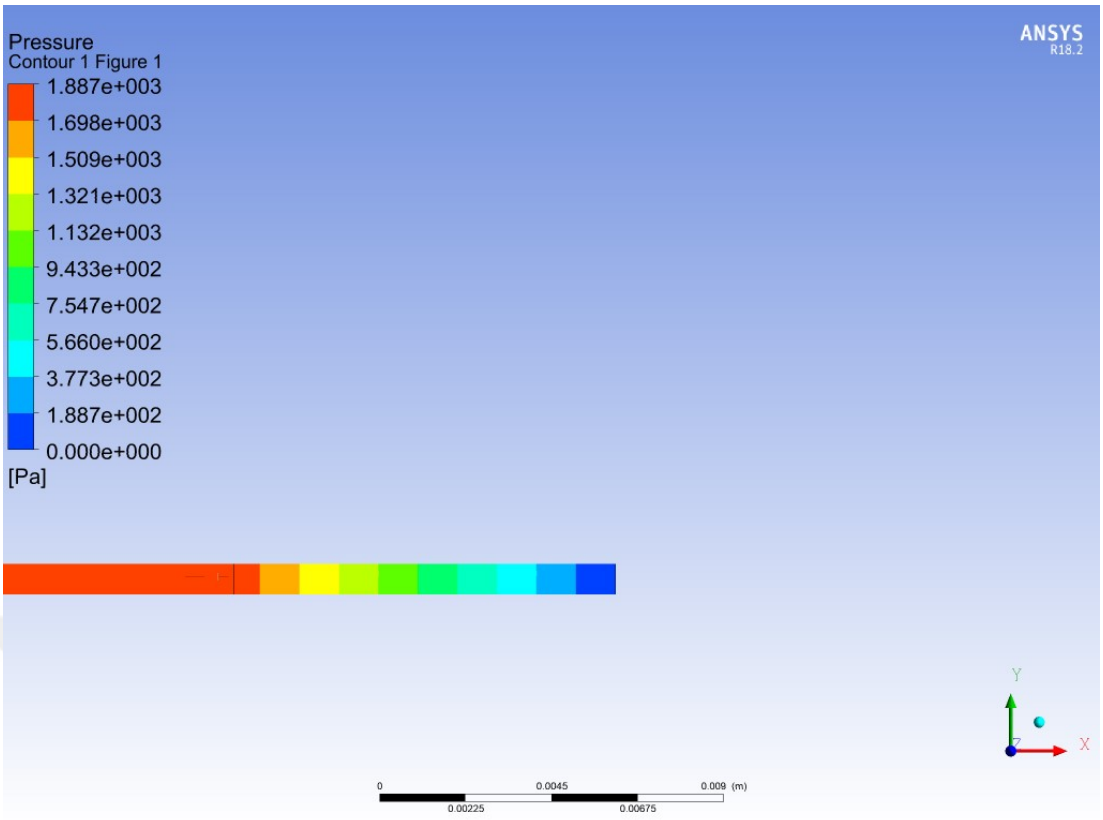

Figure B.11 Pressure drop of single plate Molteno device at 15 mmHg.

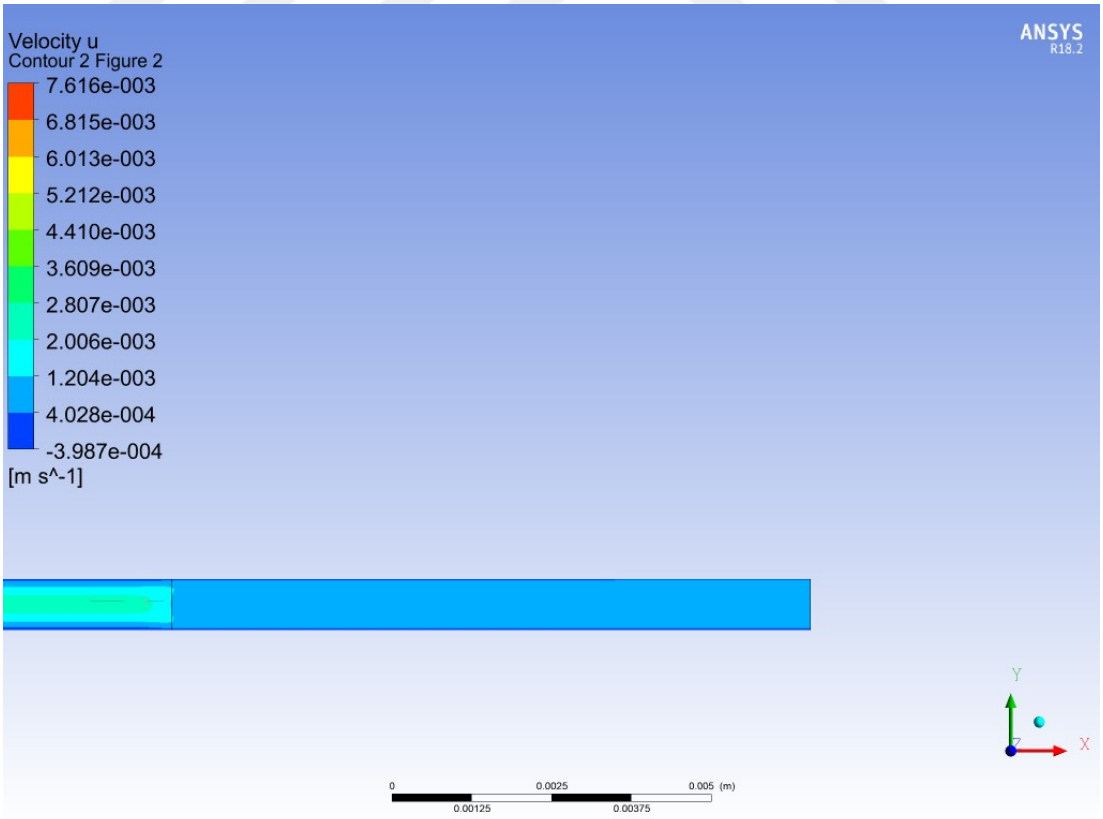

Figure B.12 Velocity contours of single plate Molteno device at 15 mmHg.

20 mmHg

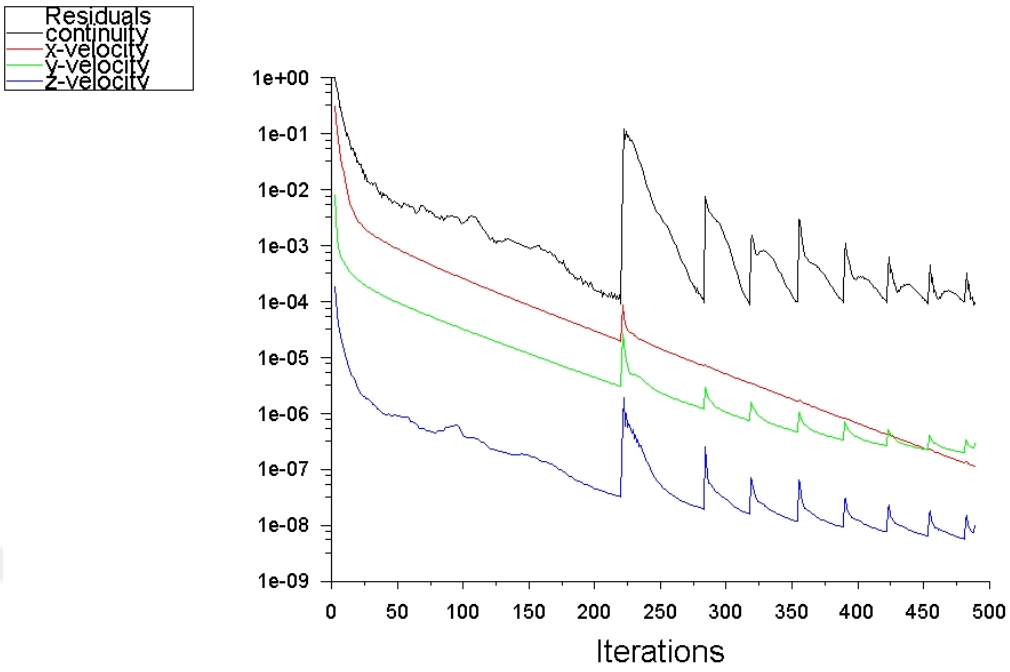

Figure B.13 Convergence results of single plate Molteno device at 20 mmHg.

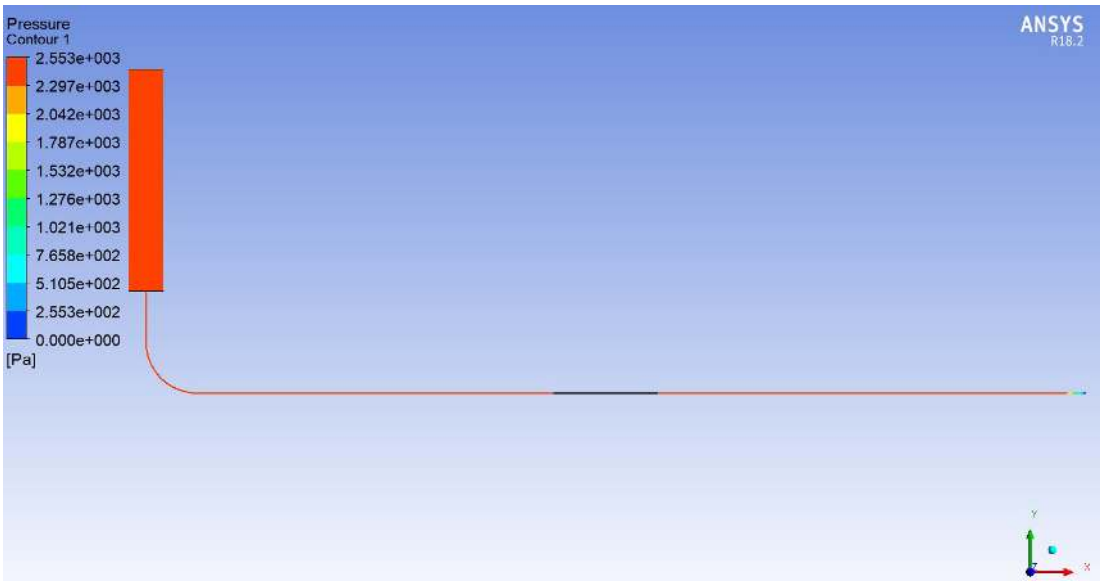

Figure B.14 Pressure drop of experimental setup at 20 mmHg.

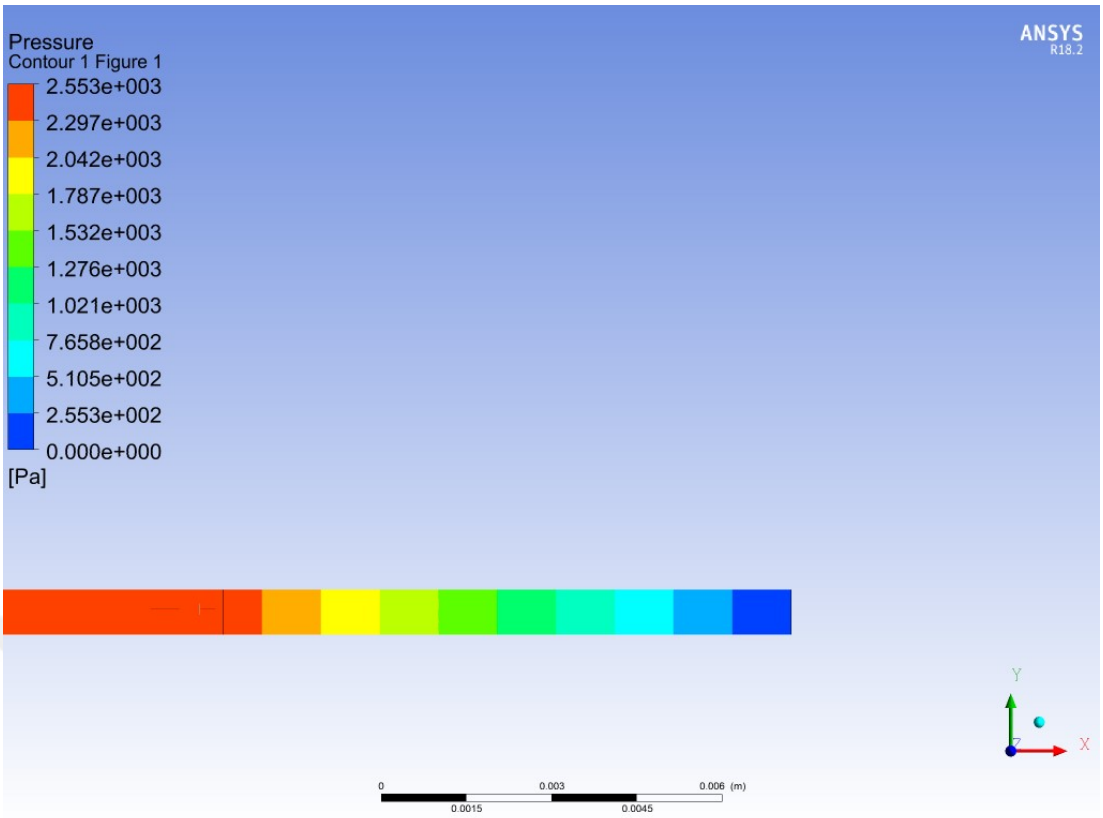

Figure B.15 Pressure drop of single plate Molteno device at 20 mmHg.

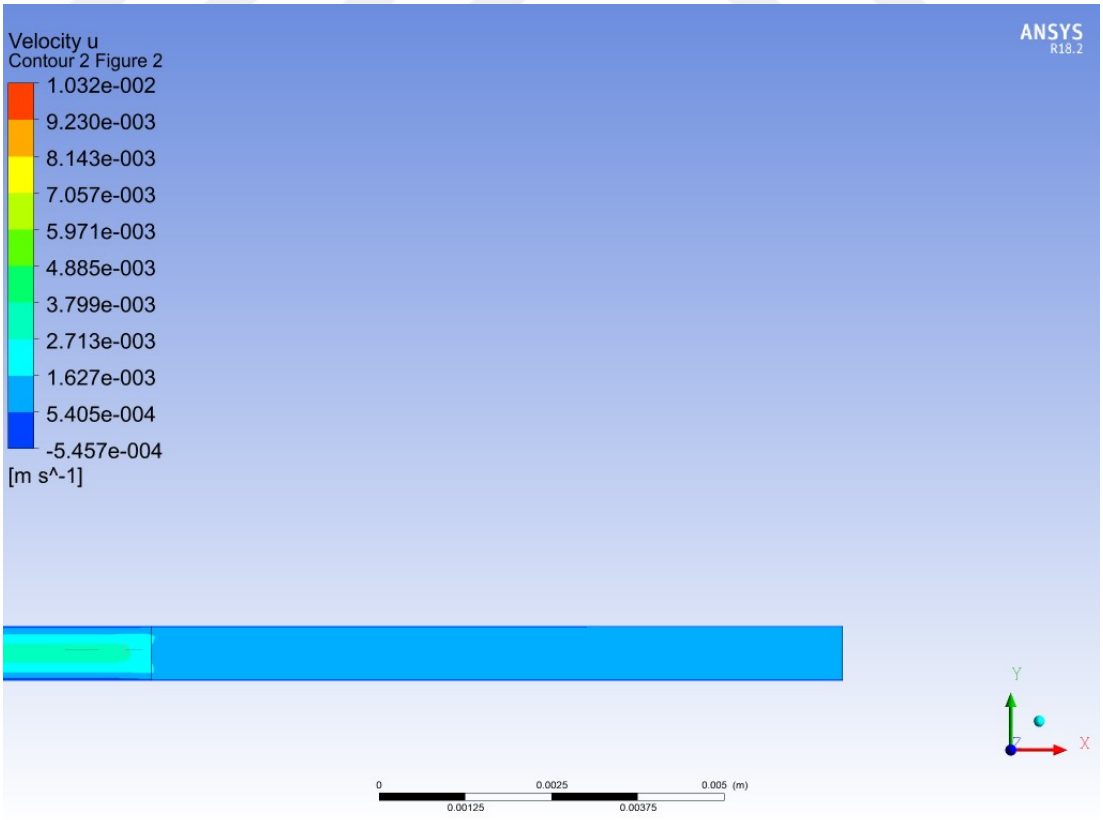

Figure B.16 Velocity contours of single plate Molteno device at 20 mmHg.

25 mmHg

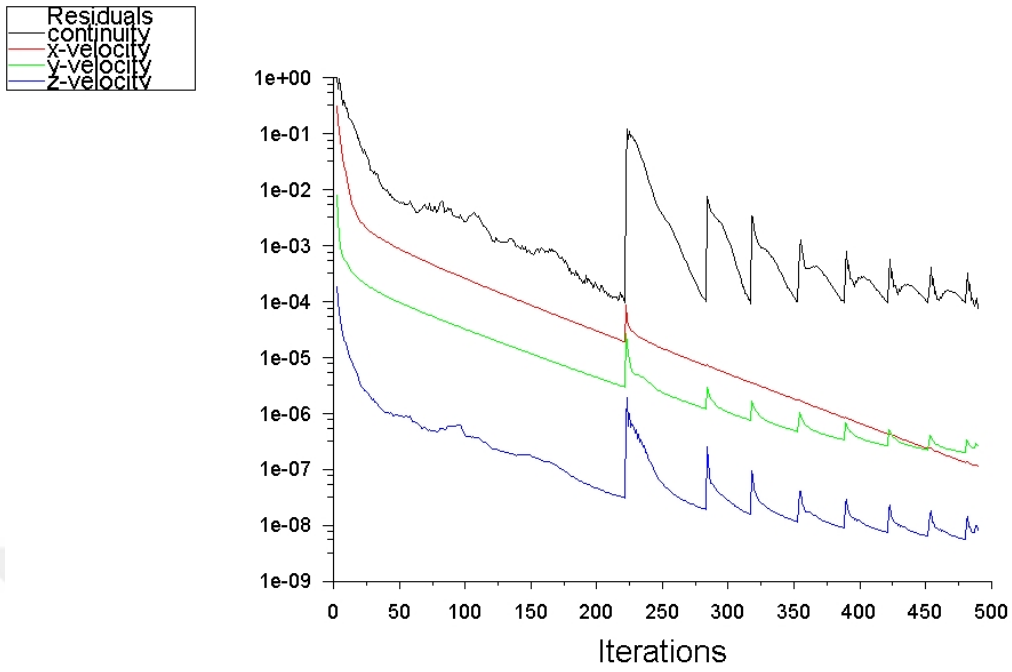

Figure B.17 Convergence results of single plate Molteno device at 25 mmHg.

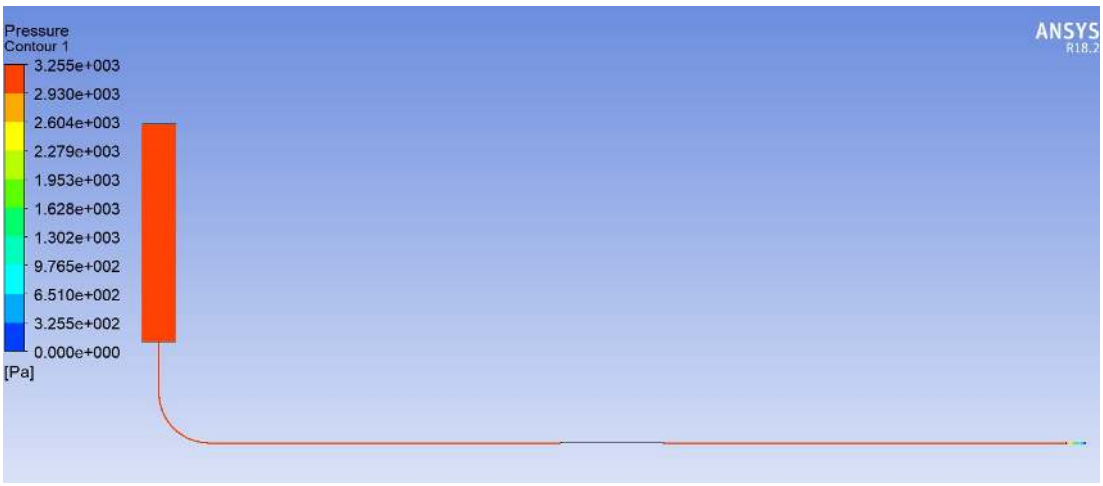

Figure B.18 Pressure drop of experimental setup at 25 mmHg.

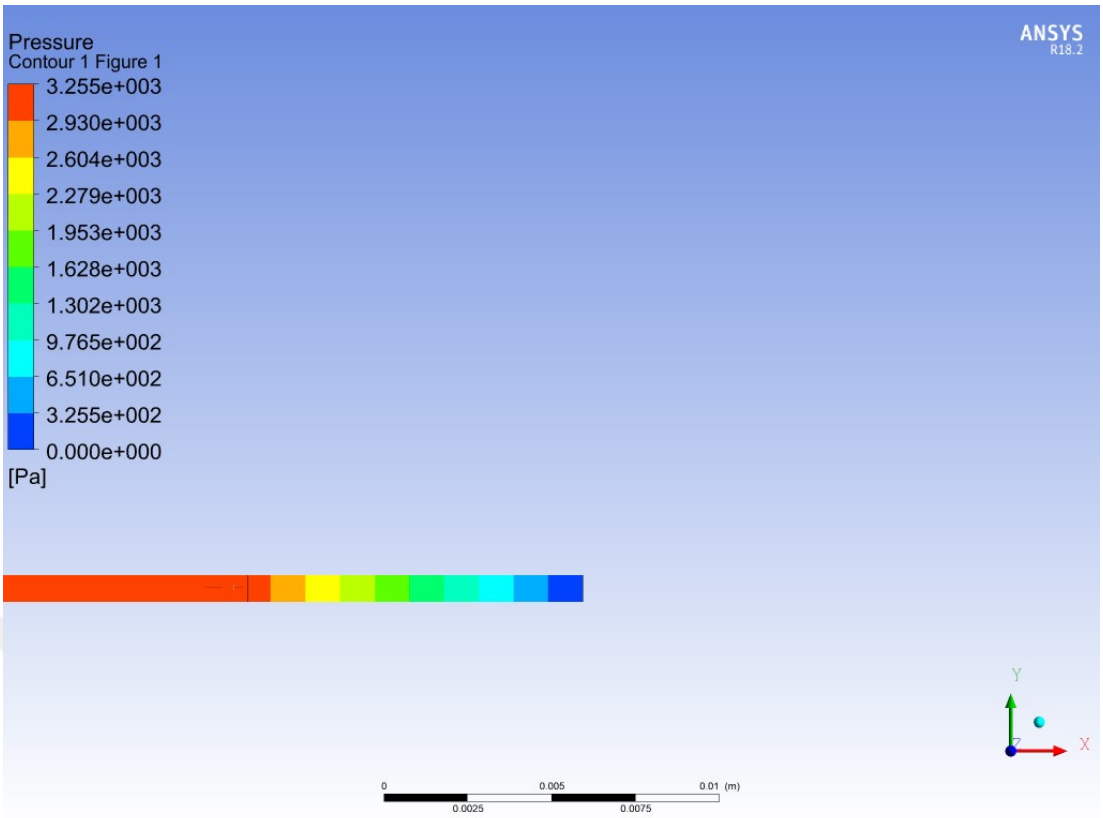

Figure B.19 Pressure drop of single plate Molteno device at 25 mmHg.

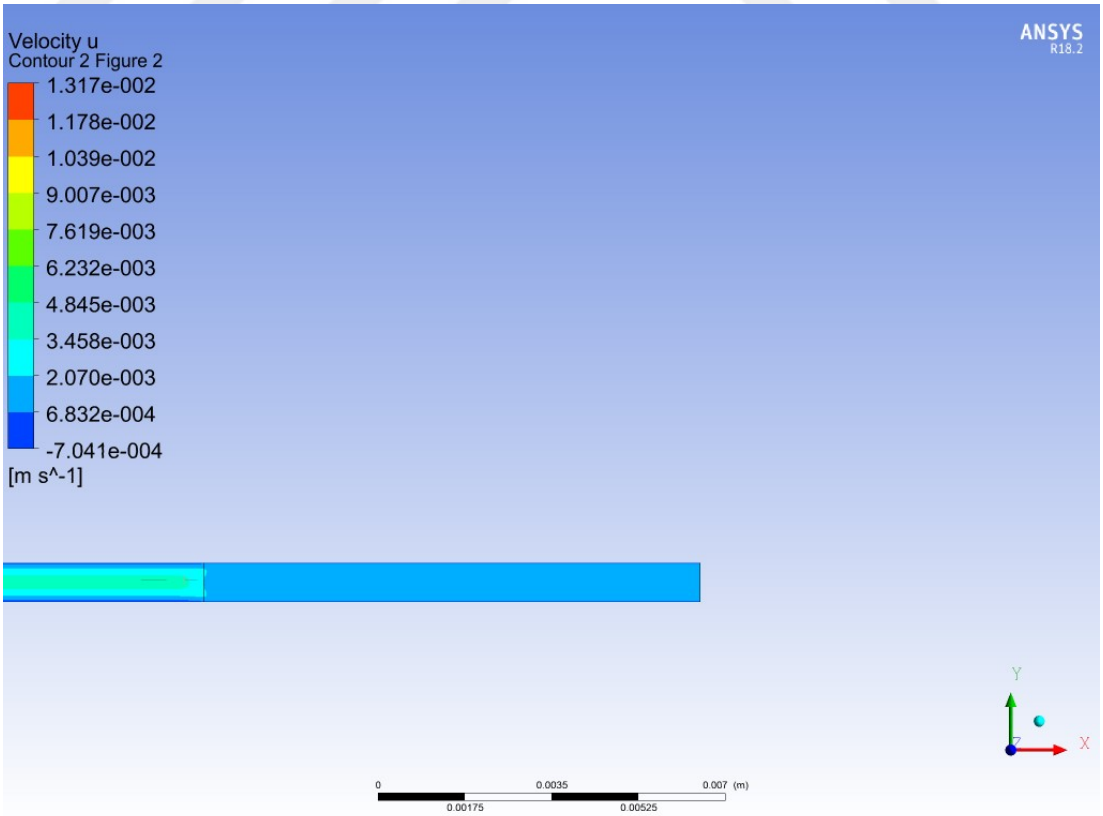

Figure B.20 Velocity contours of single plate Molteno device at 25 mmHg.

APPENDIX C

POSTPROCESSING OF DOUBLE PLATE MOLTENO DEVICE

5 µl/min

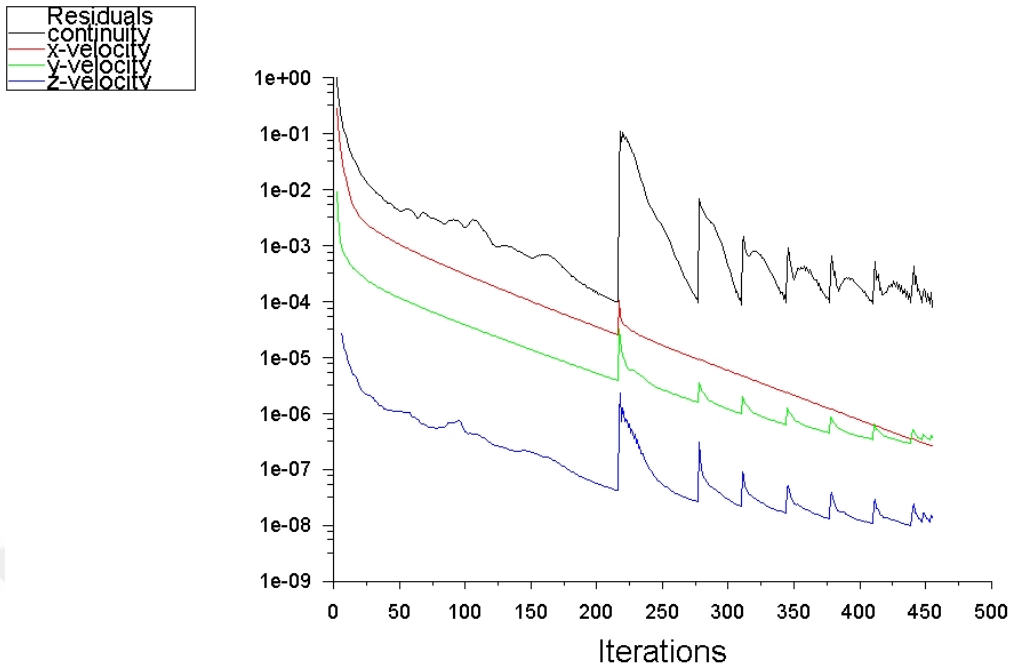

Figure C.1 Convergence results of double plate Molteno device at 5 µl/min.

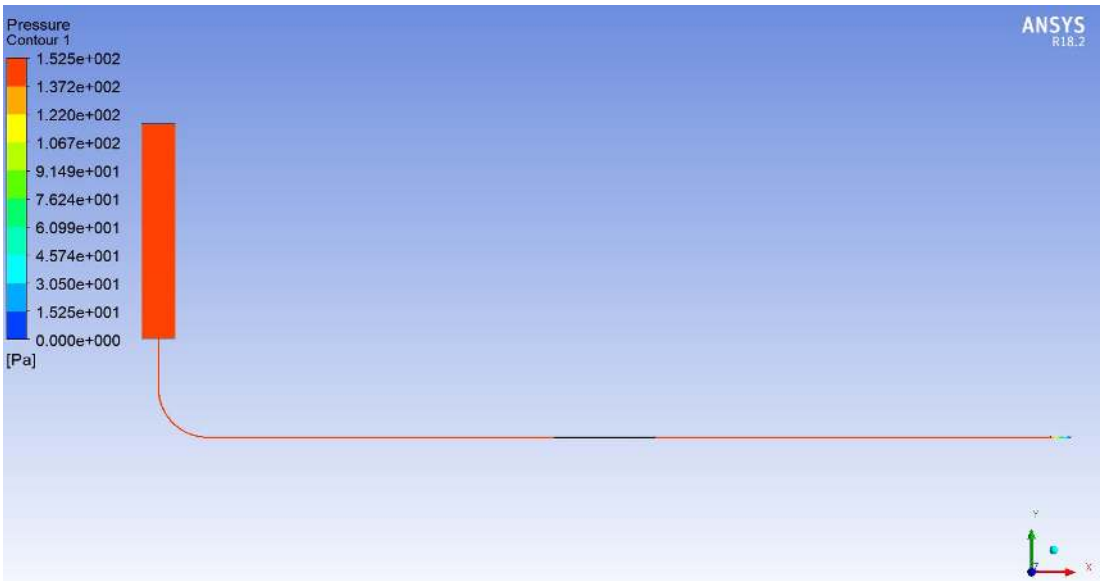

Figure C.2 Pressure drop of experimental setup at 5 µl/min.

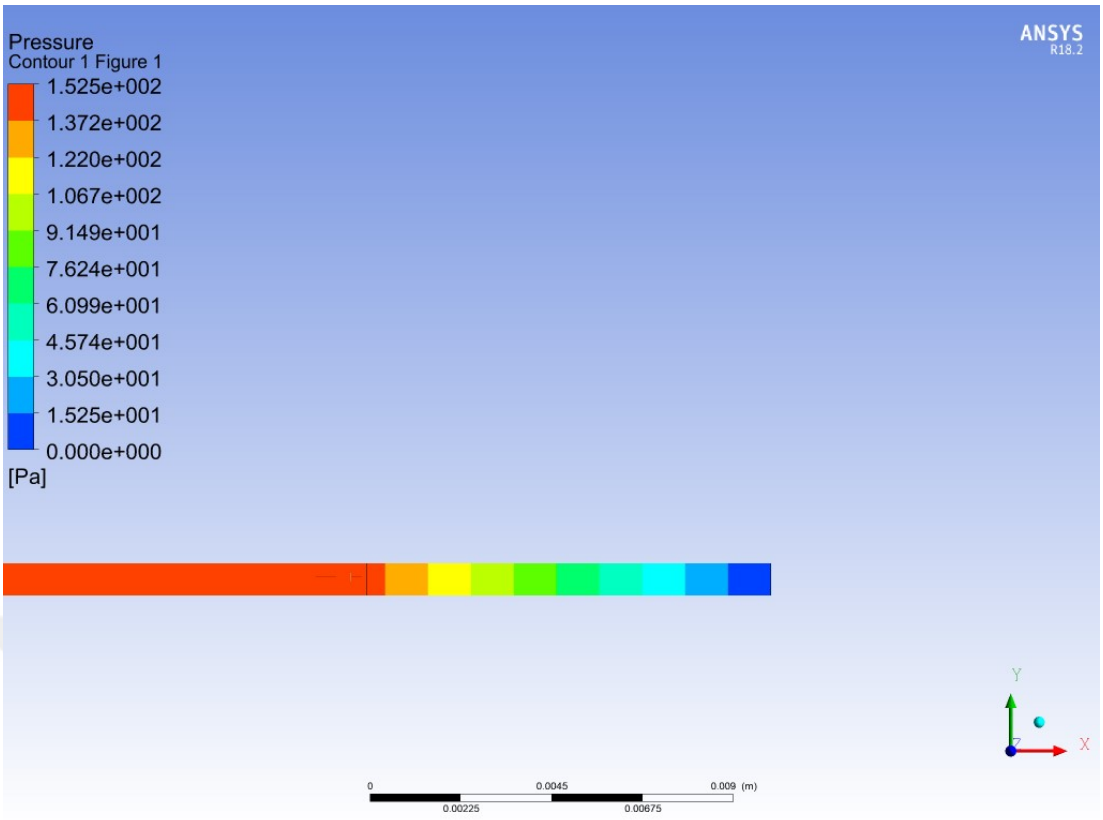

Figure C.3 Pressure drop of double plate Molteno device at 5 µl/min.

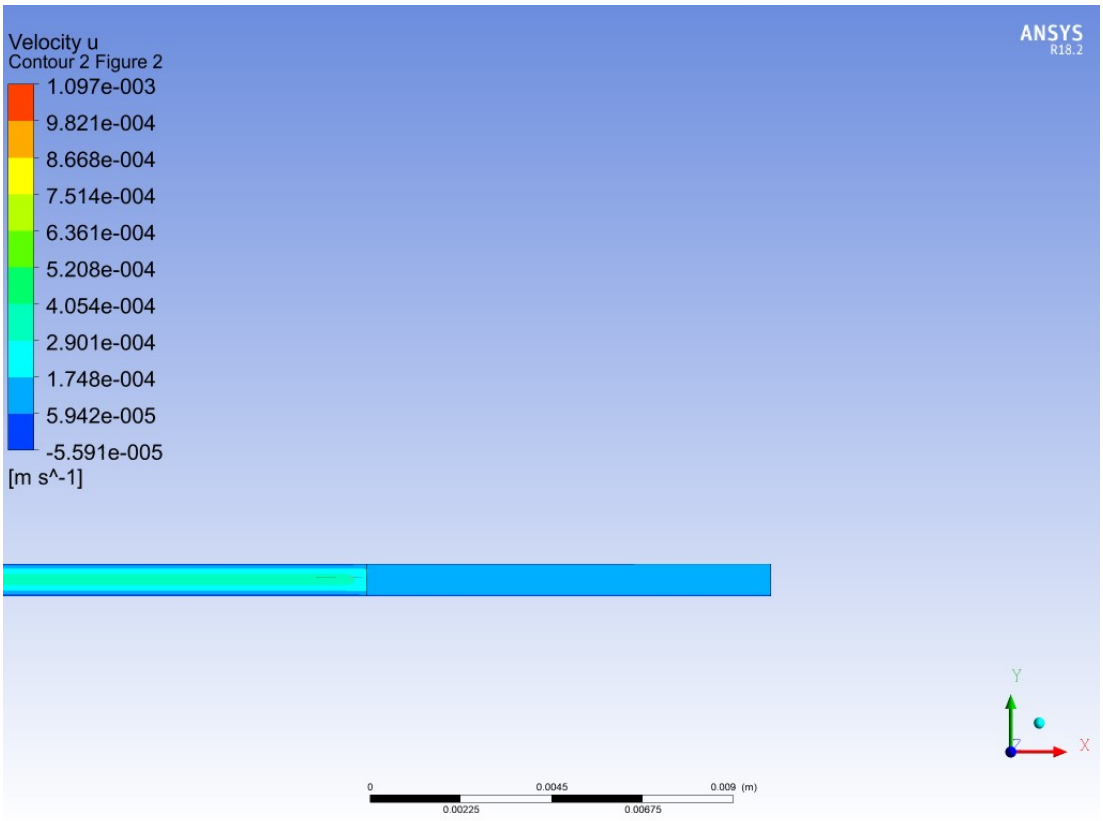

Figure C.4 Velocity contours of double plate Molteno device at 5 µl/min.

10 µl/min

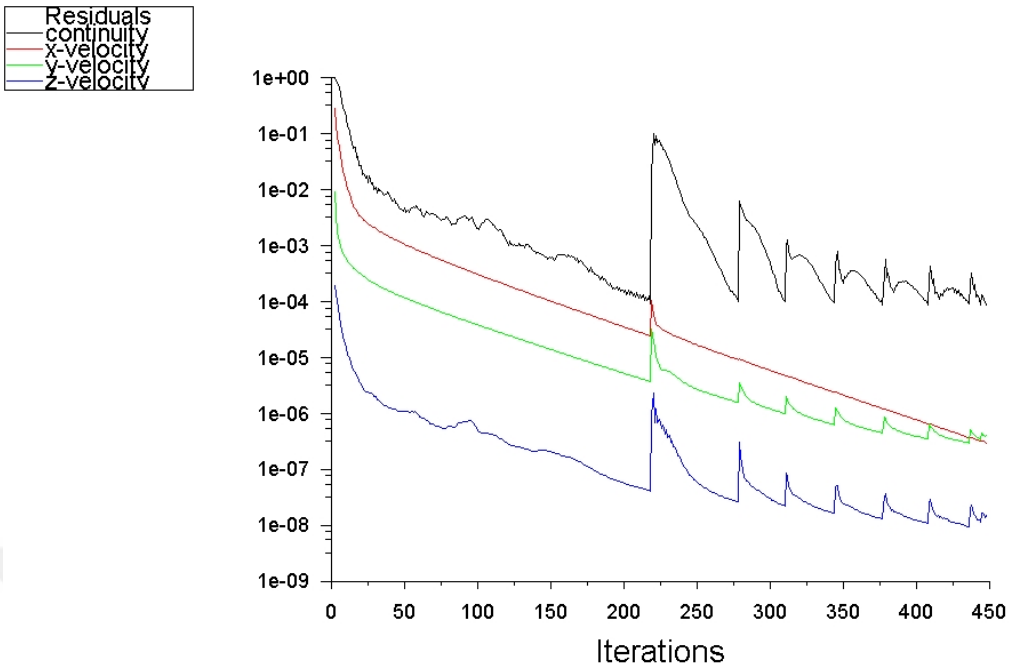

Figure C.5 Convergence results of double plate Molteno device at 10 µl/min.

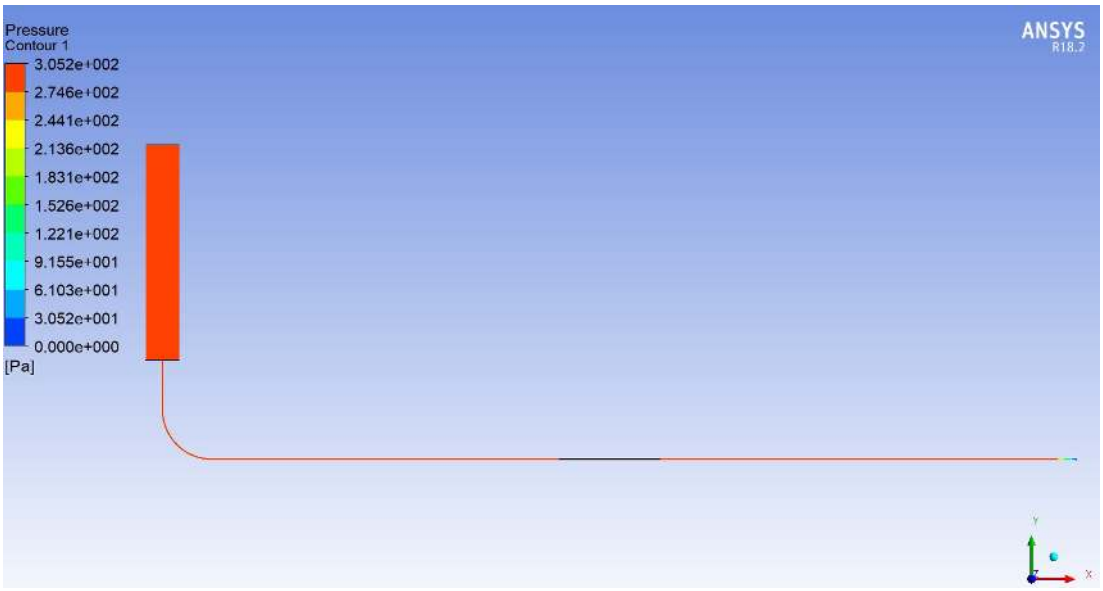

Figure C.6 Pressure drop of experimental setup at 10 µl/min.

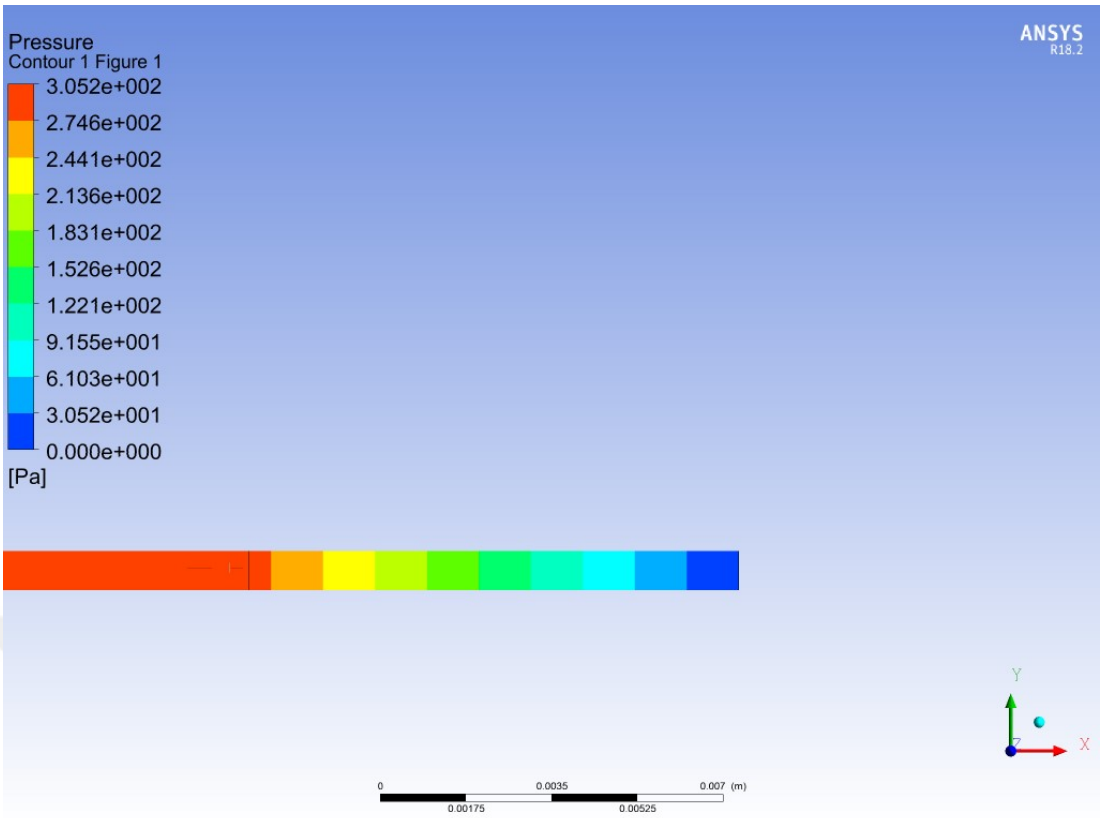

Figure C.7 Pressure drop of double plate Molteno device at 10 µl/min.

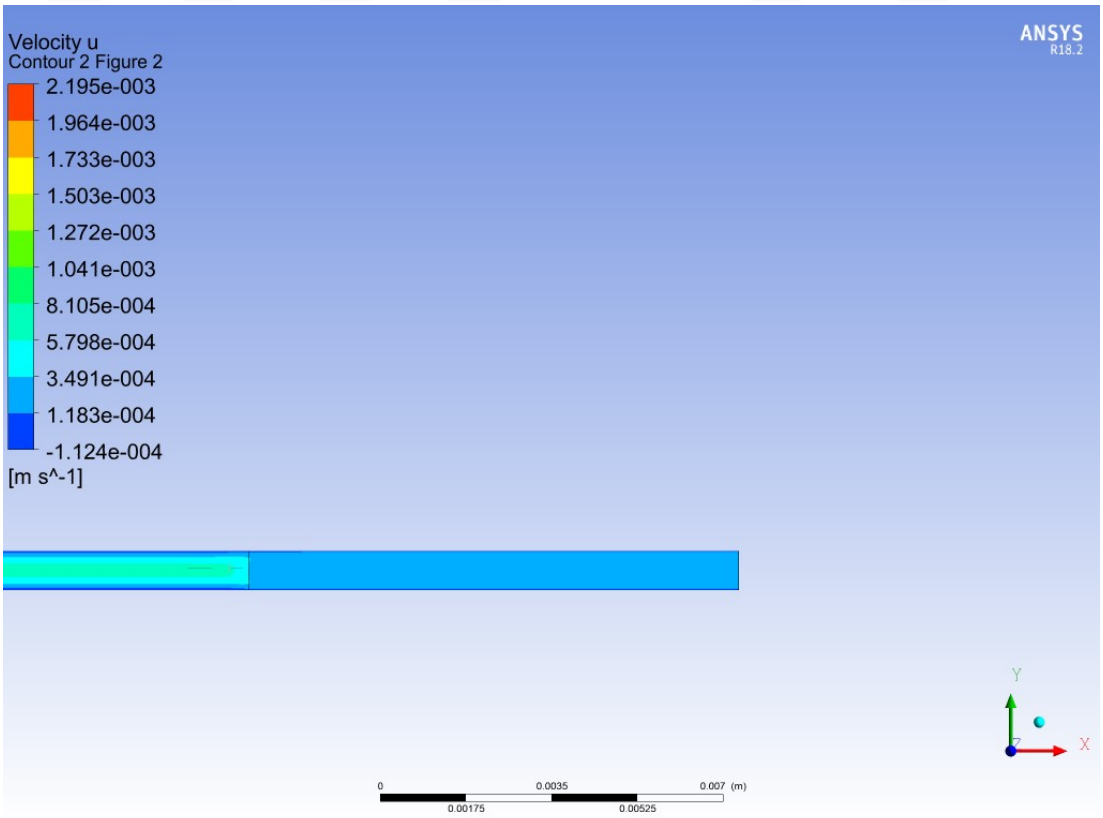

Figure C.8 Velocity contours of double plate Molteno device at 10 µl/min.

15 µl/min

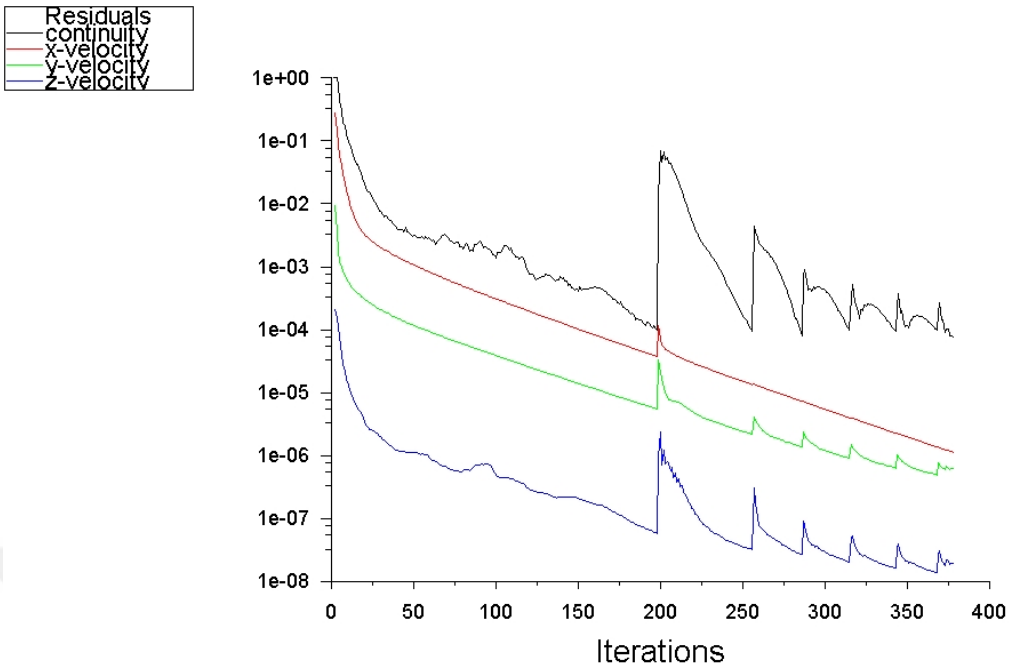

Figure C.9 Convergence results of double plate Molteno device at 15 µl/min.

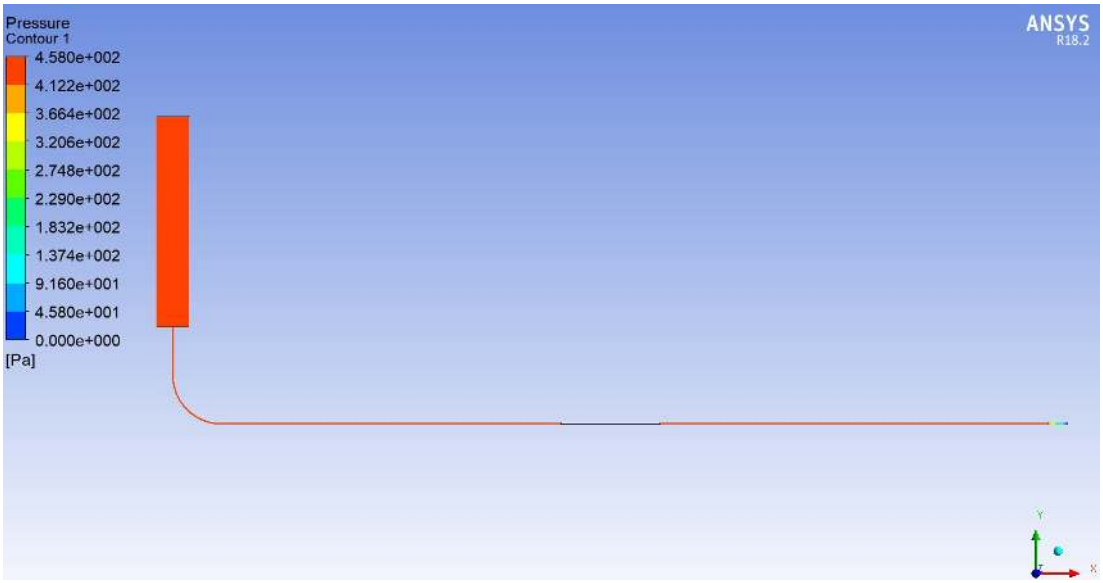

Figure C.10 Pressure drop of experimental setup at 15 µl/min.

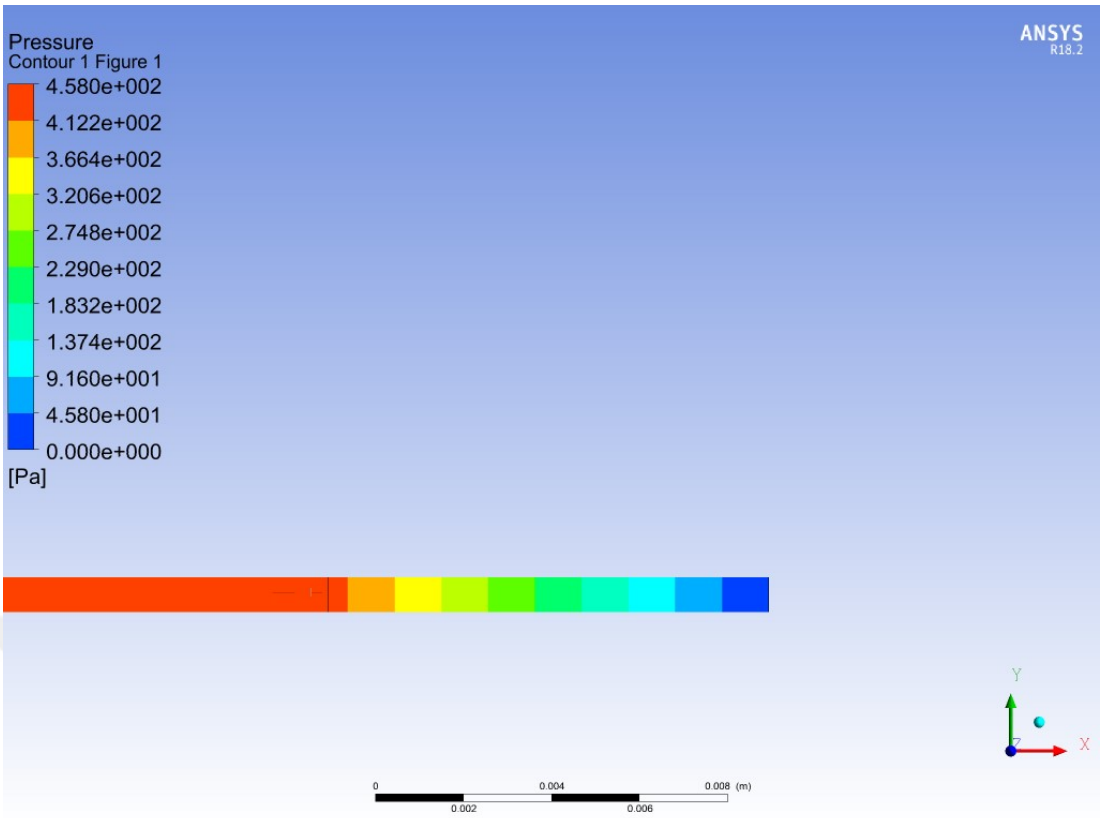

Figure C.11 Pressure drop of double plate Molteno device at 15 µl/min.

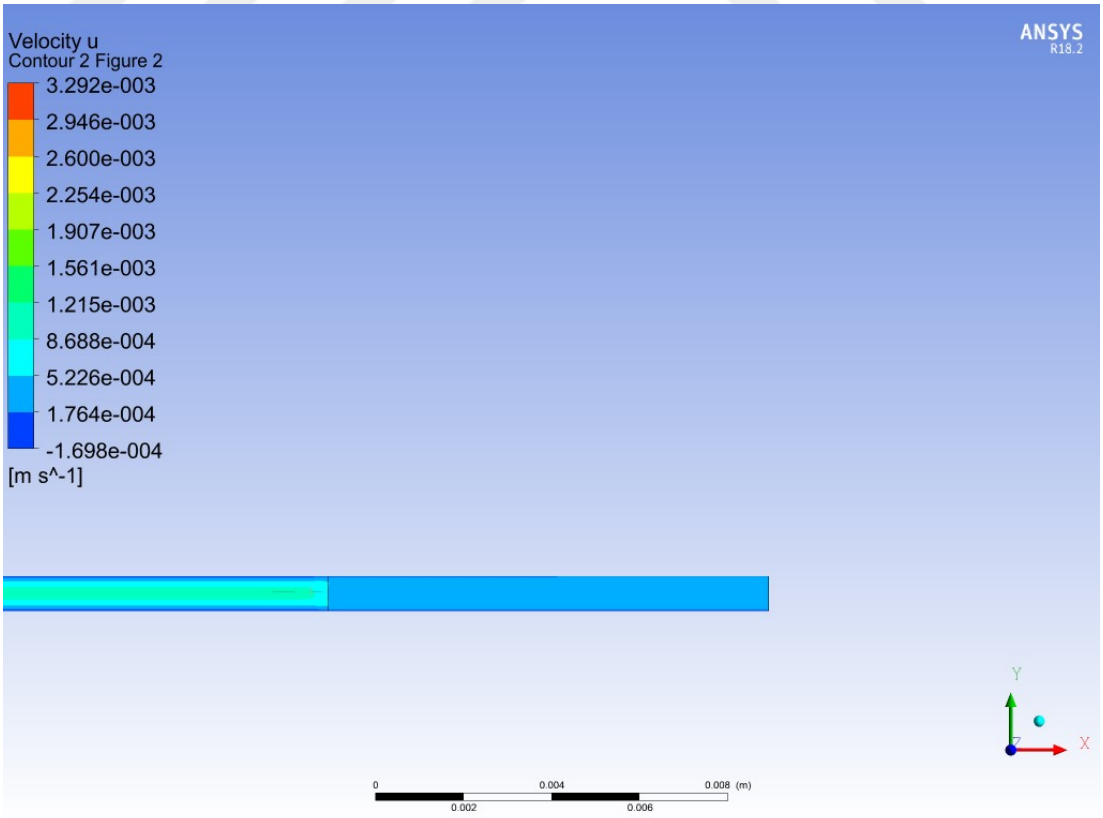

Figure C.12 Velocity contours of double plate Molteno device at 15 µl/min.

20 µl/min

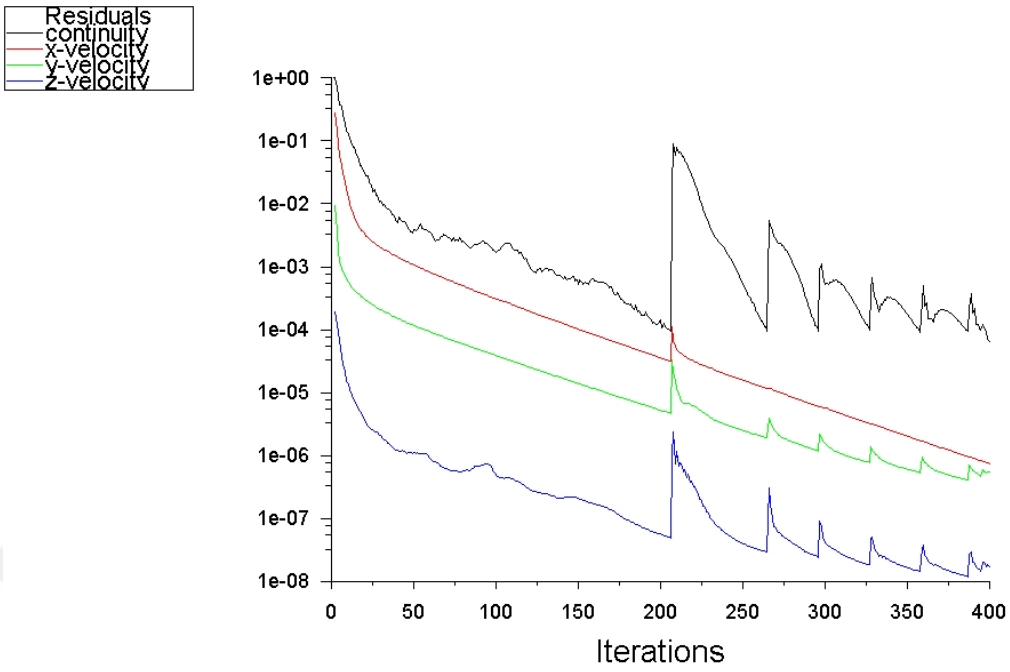

Figure C.13 Convergence results of double plate Molteno device at 20µl/min.

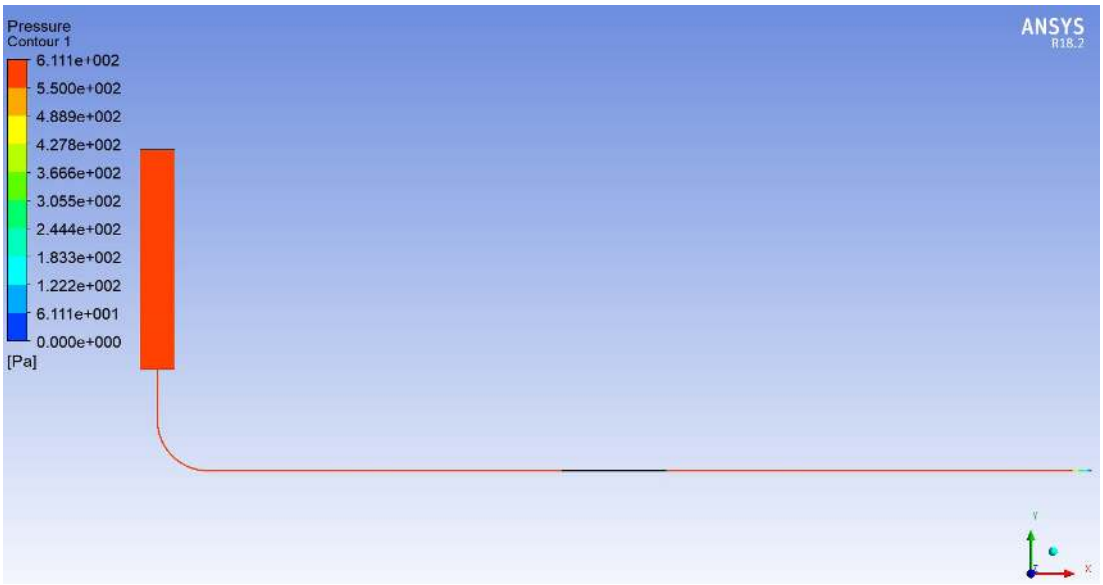

Figure C.14 Pressure drop of experimental setup at 20 µl/min.

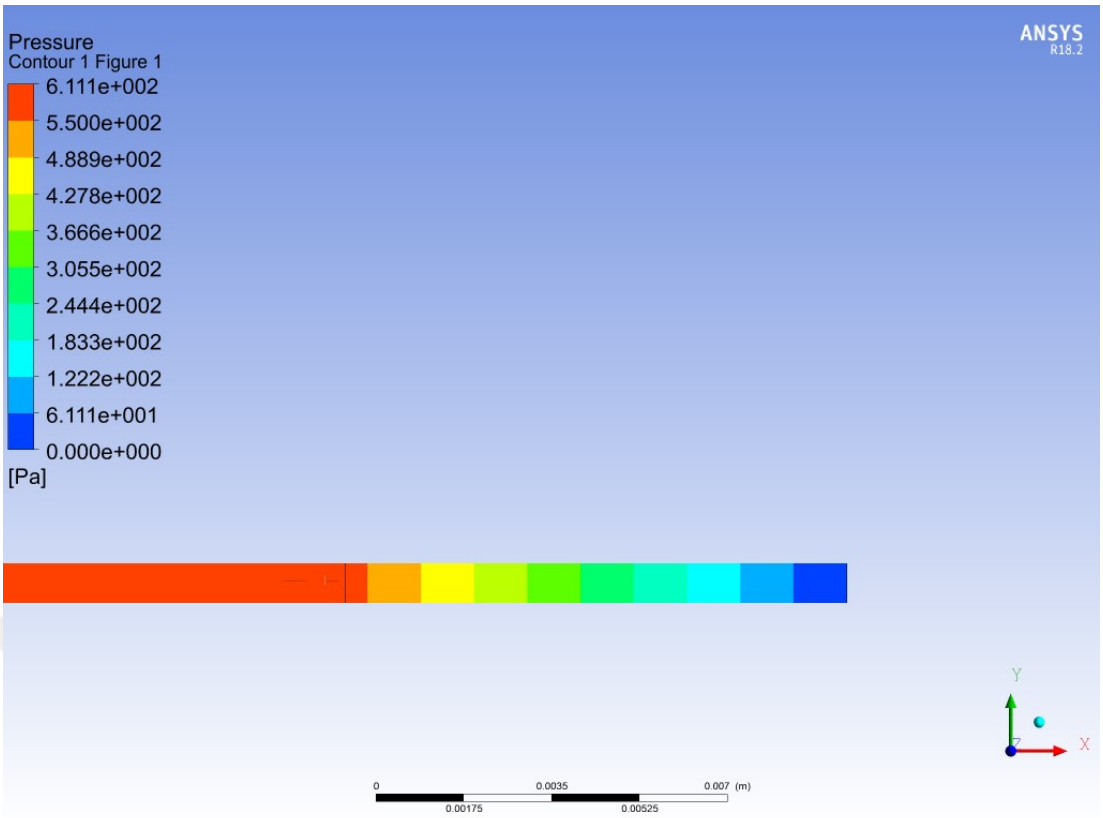

Figure C.15 Pressure drop of double plate Molteno device at 20 µl/min.

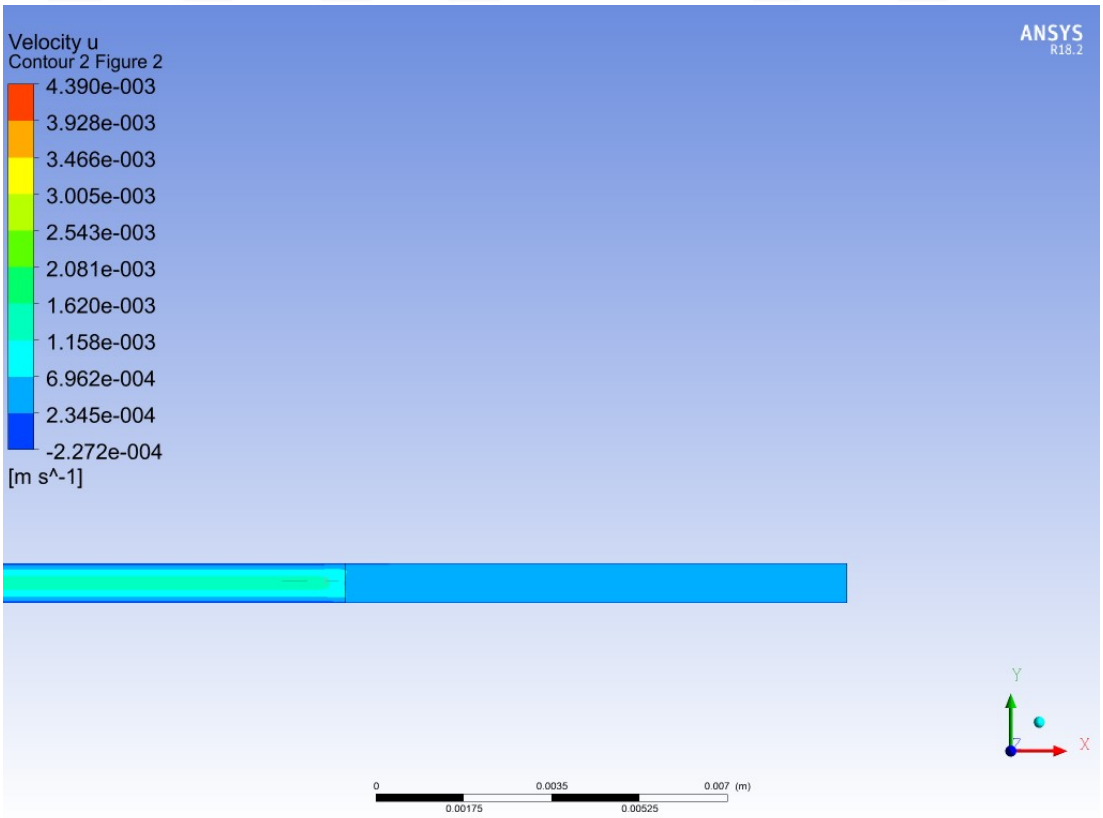

Figure C.16 Velocity contours of double plate Molteno device at 20 µl/min.

25 µl/min

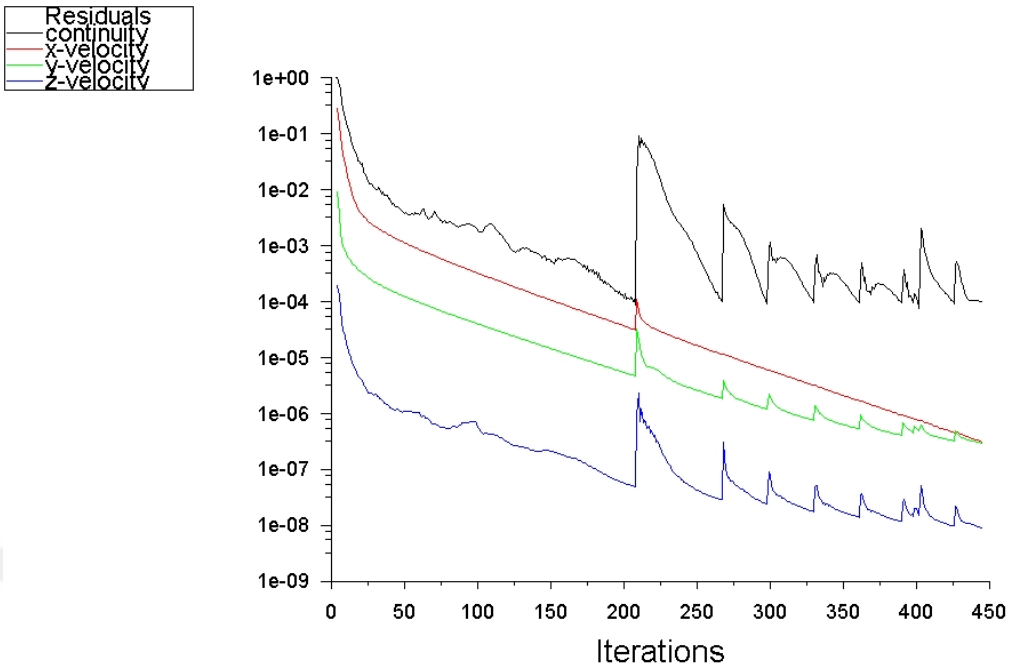

Figure C.17 Convergence results of double plate Molteno device at 25 µl/min.

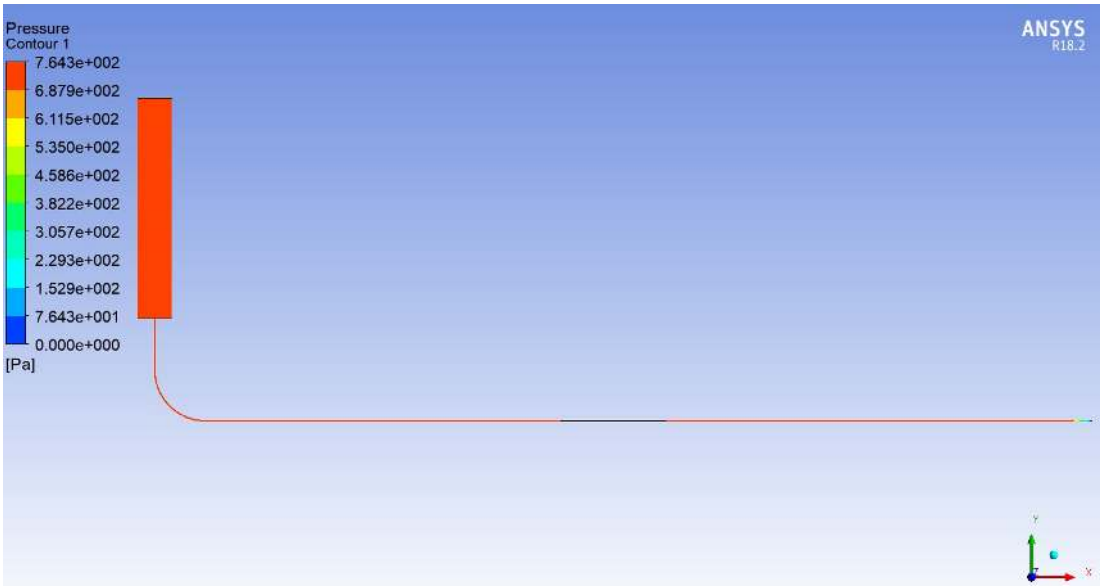

Figure C.18 Pressure drop of experimental setup at 25 µl/min

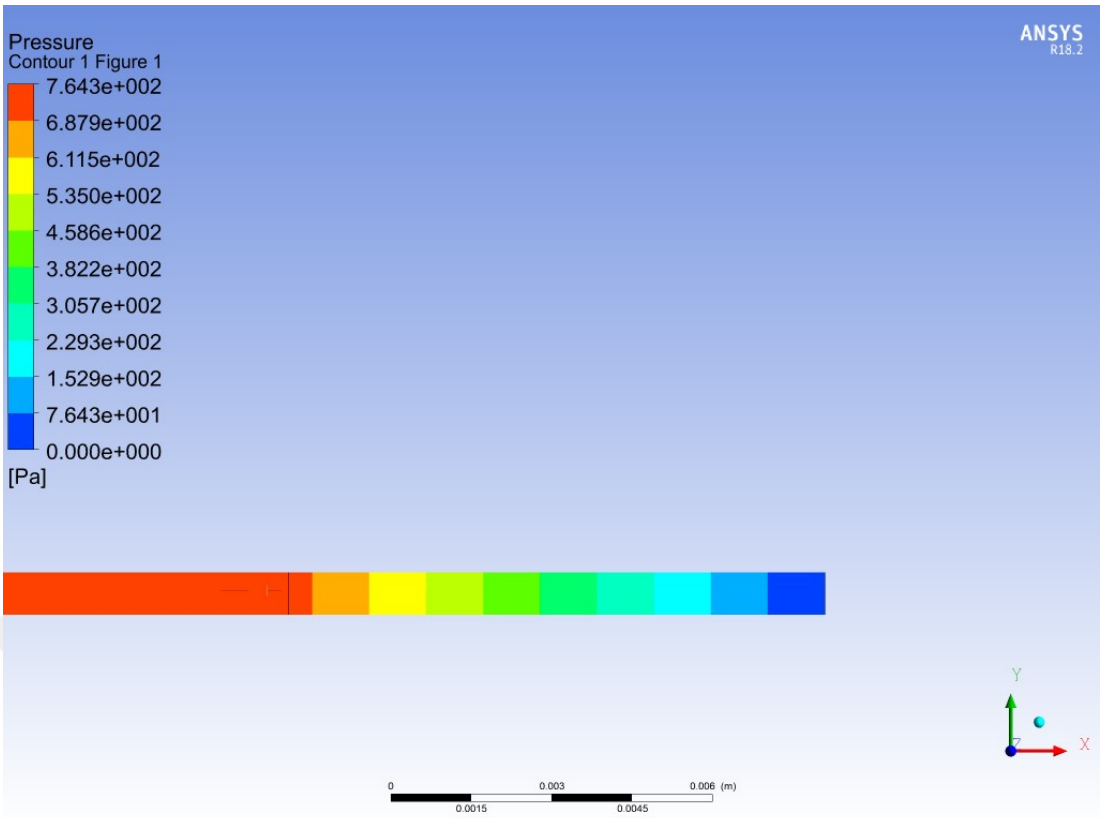

Figure C.19 Pressure drop of double plate Molteno device at 25 µl/min.

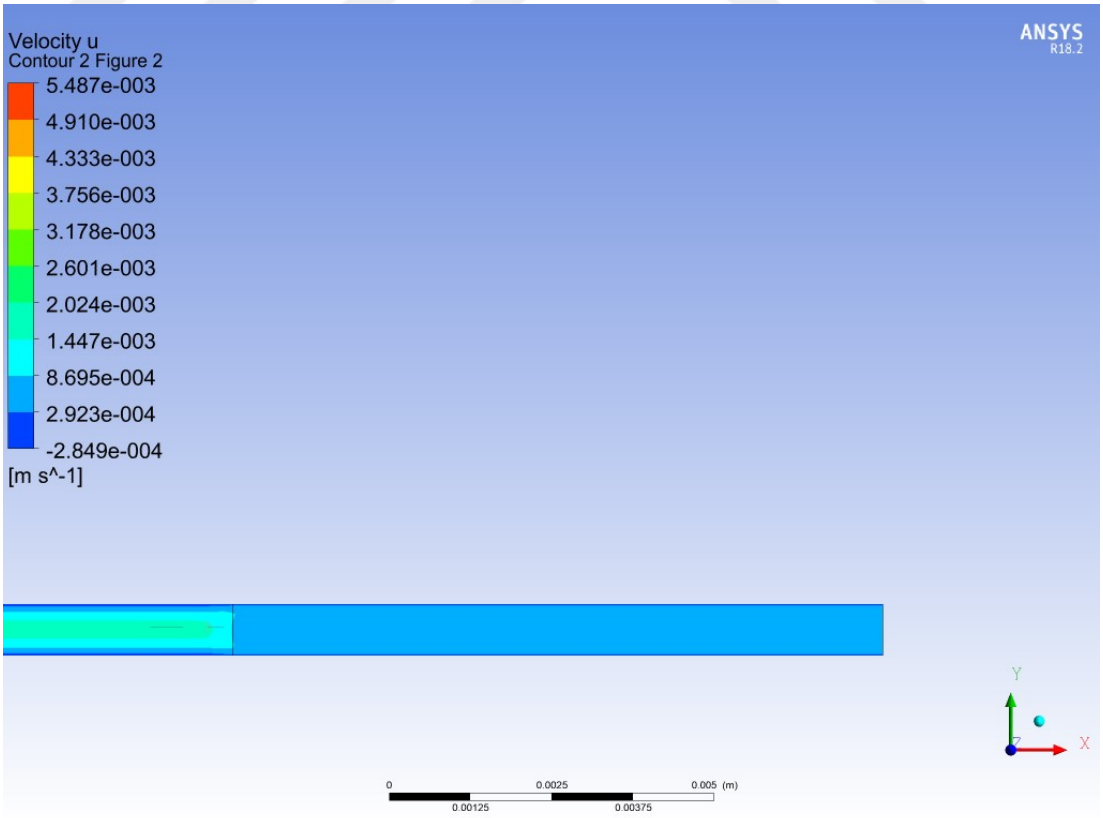

Figure C.20 Velocity contours of double plate Molteno device at 25 µl/min.

APPENDIX D

POSTPROCESSING OF XEN IMPLANT

At Physiological Flow Rate

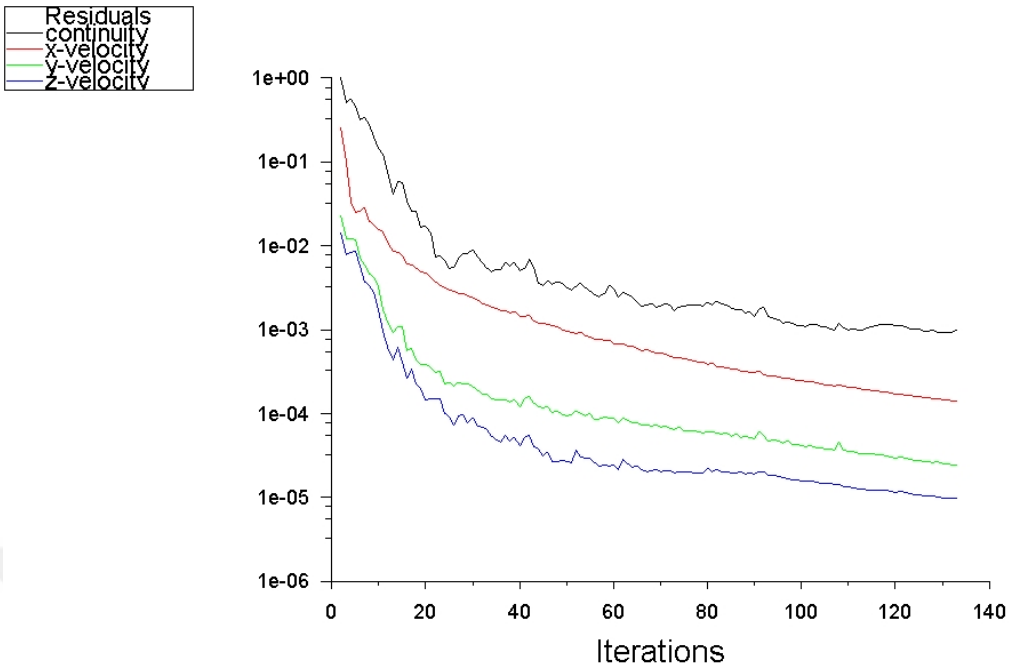

Figure D.1 Convergence results of XEN implant at 2.5 µl/min.

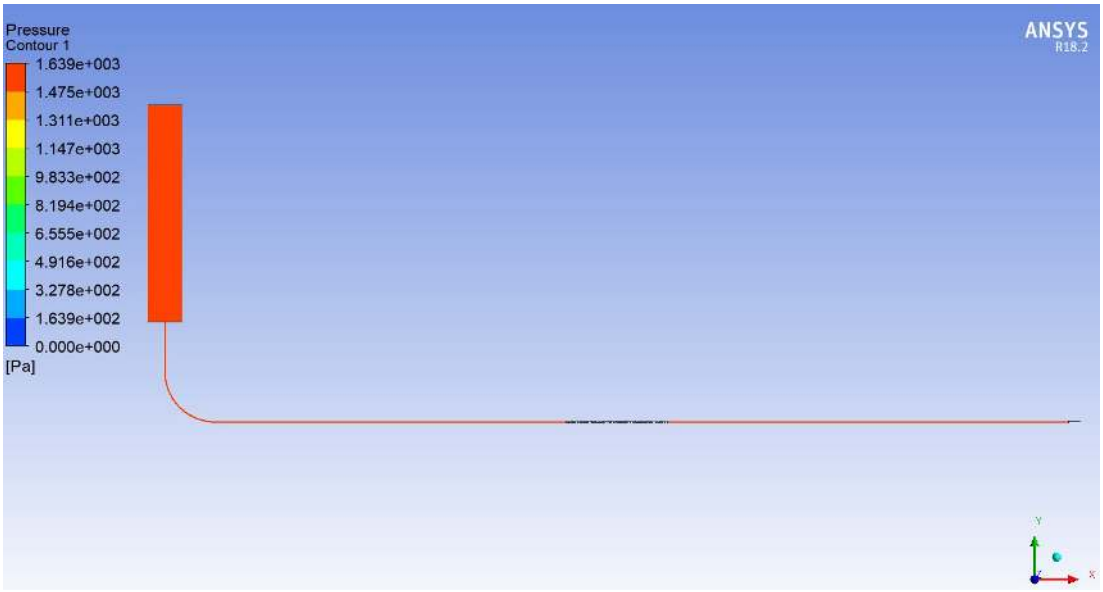

Figure D.2 Pressure drop of experimental setup at 2.5 µl/min.

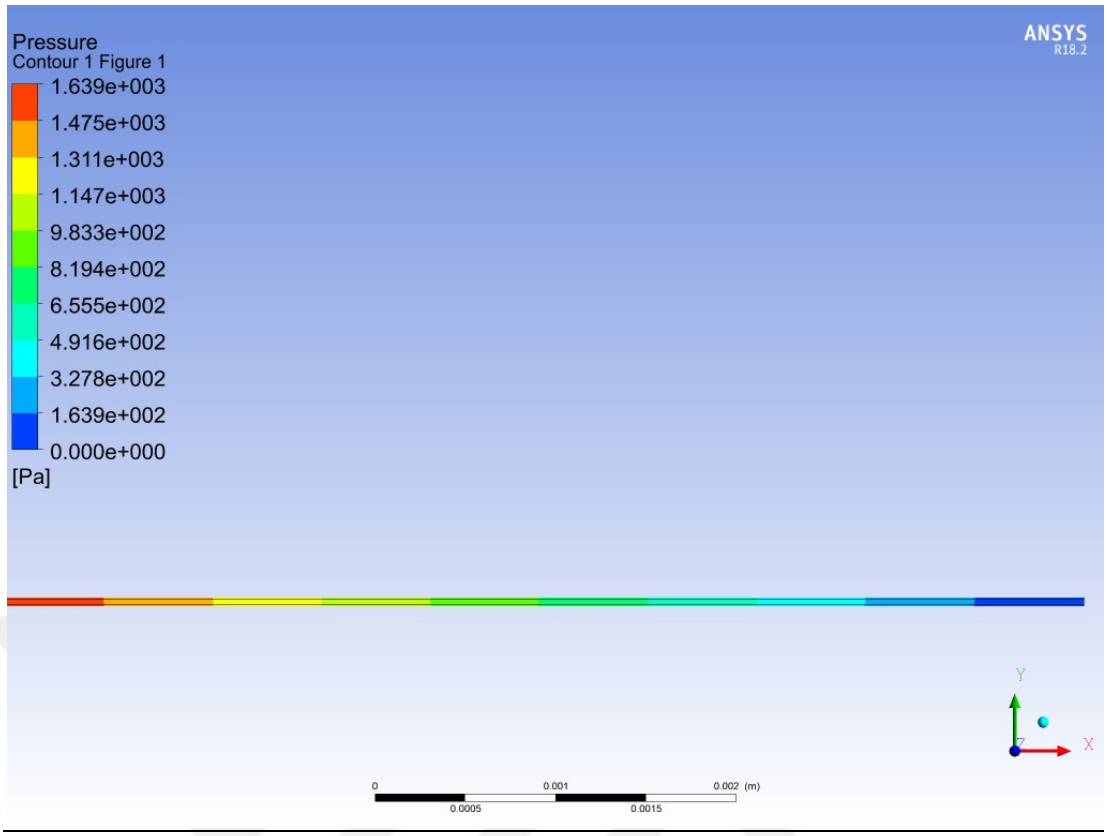

Figure D.3 Pressure drop of XEN implant at 2.5 µl/min.

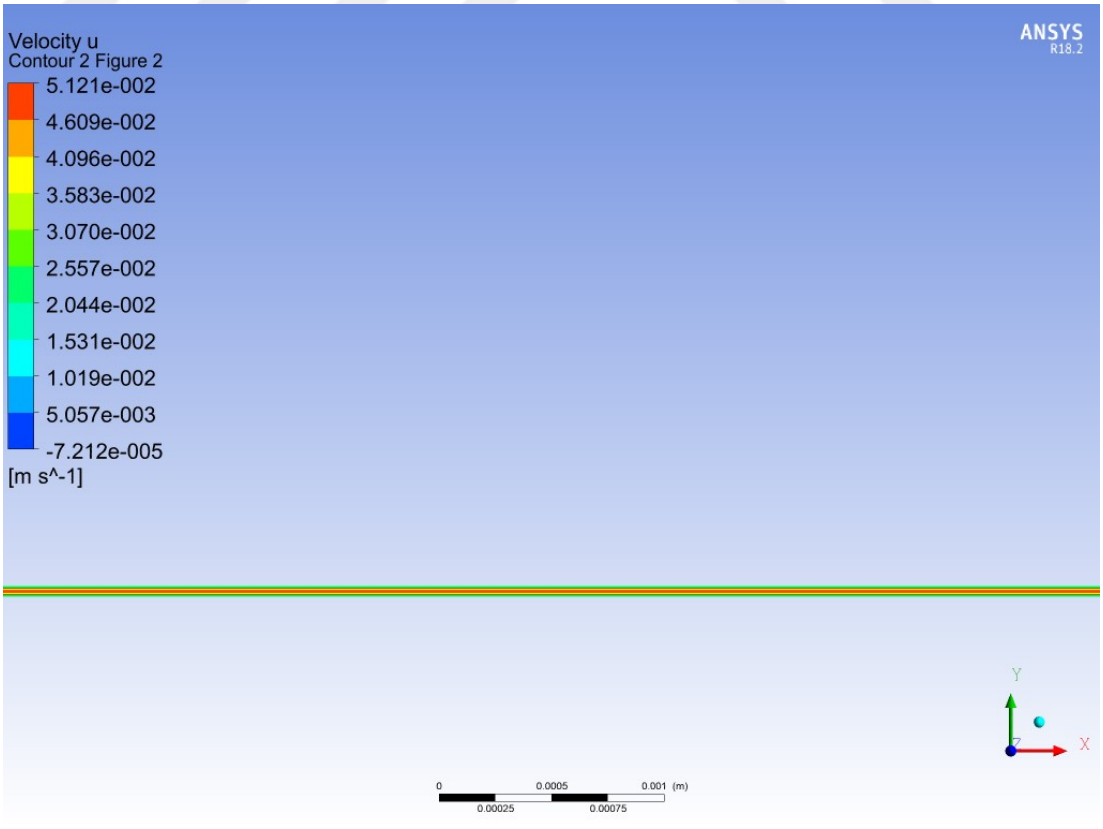

Figure D.4 Velocity contours of XEN implant at 2.5 µl/min.

APPENDIX E

POSTPROCESSING OF EXPRESS IMPLANT

5 mmHg

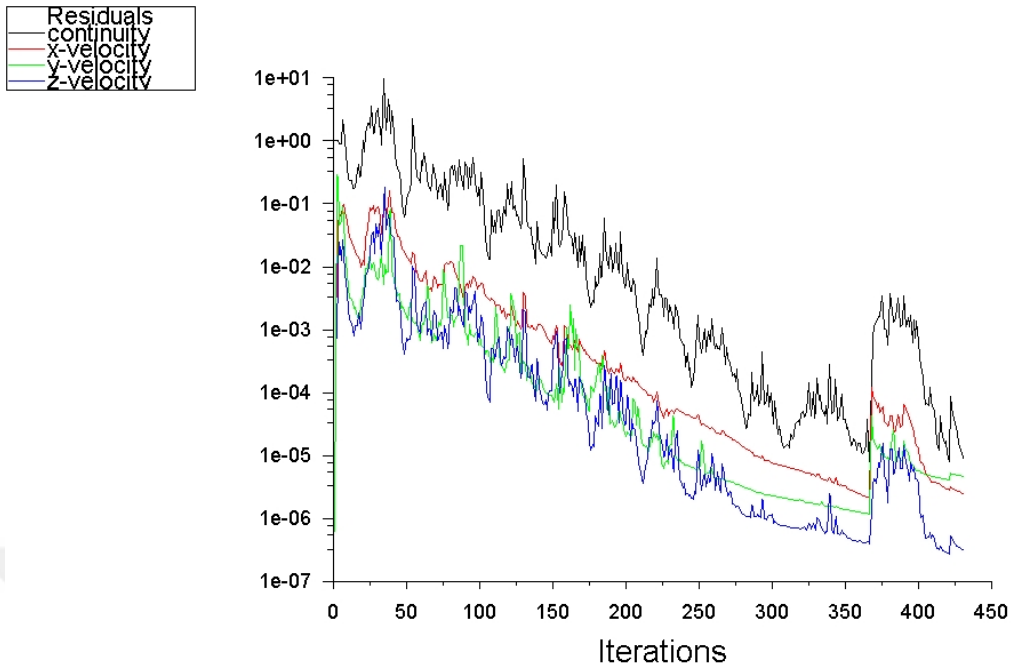

Figure E.1 Convergence results of ExPress implant at 5 mmHg.

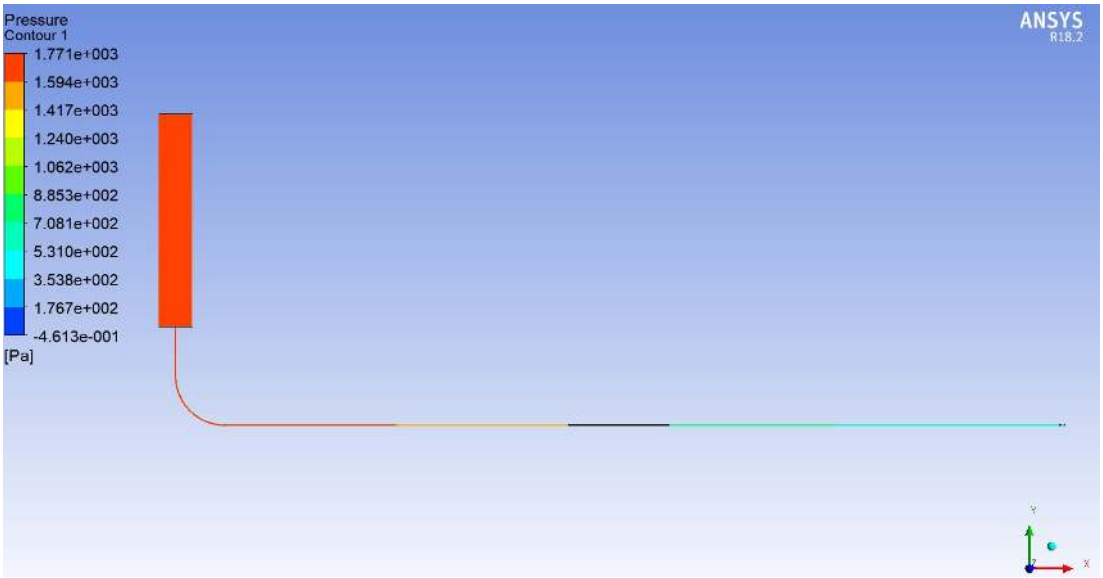

Figure E.2 Pressure drop of experimental setup at 5 mmHg.

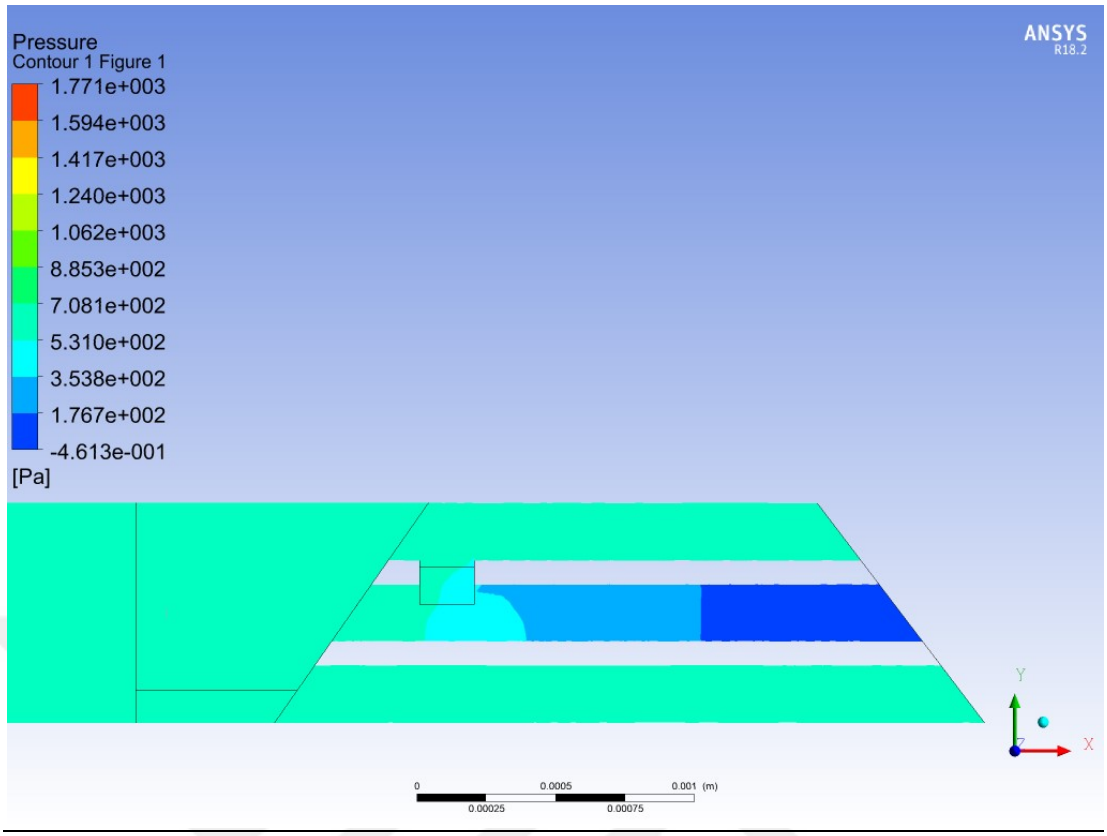

Figure E.3 Pressure drop of ExPress implant at 5 mmHg.

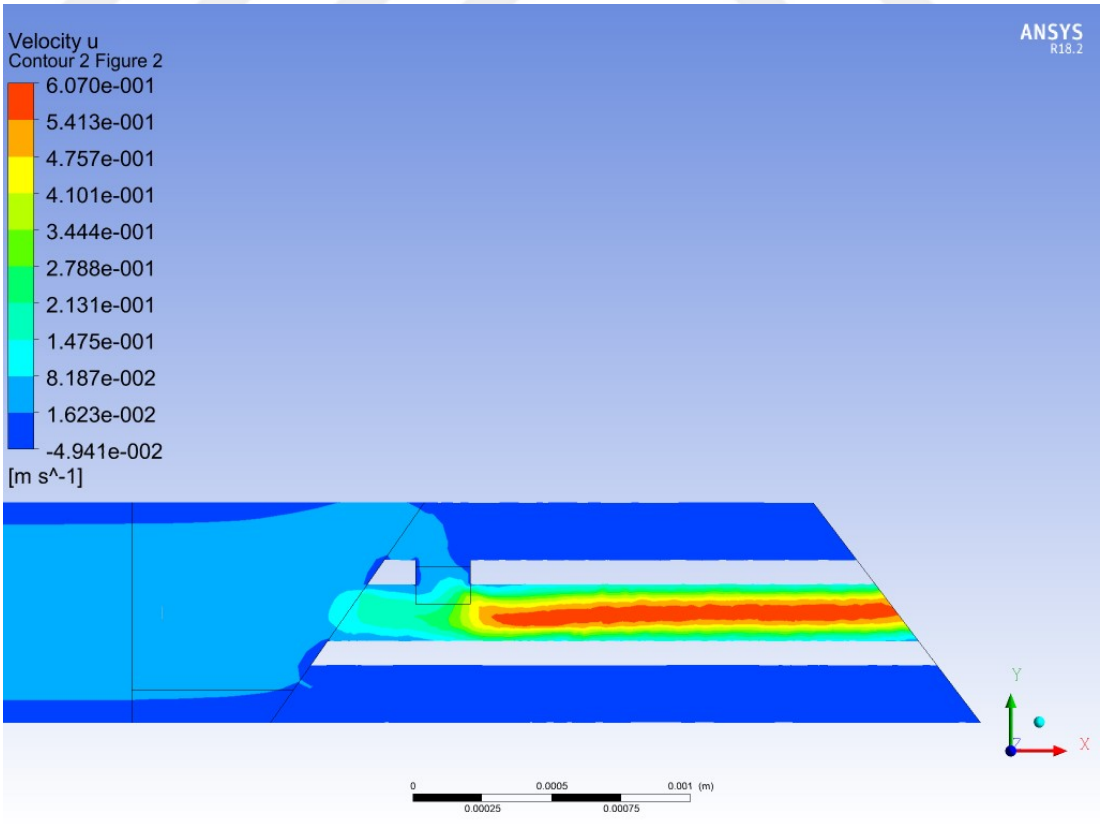

Figure E.4 Velocity contours of ExPress implant at 5 mmHg.

10 mmHg

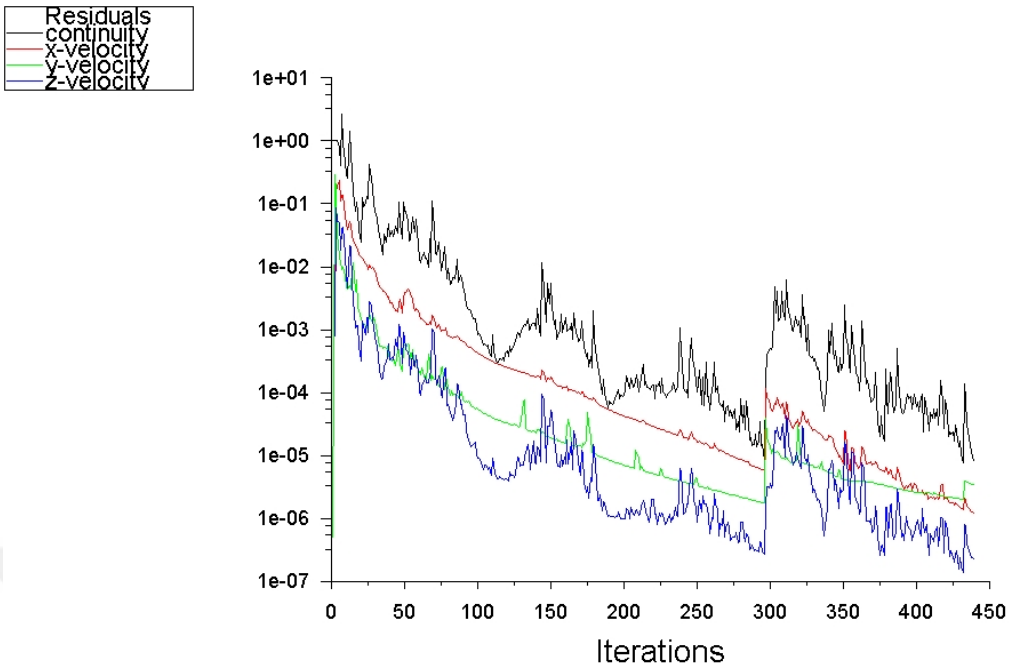

Figure E.5 Convergence results of ExPress implant at 10 mmHg.

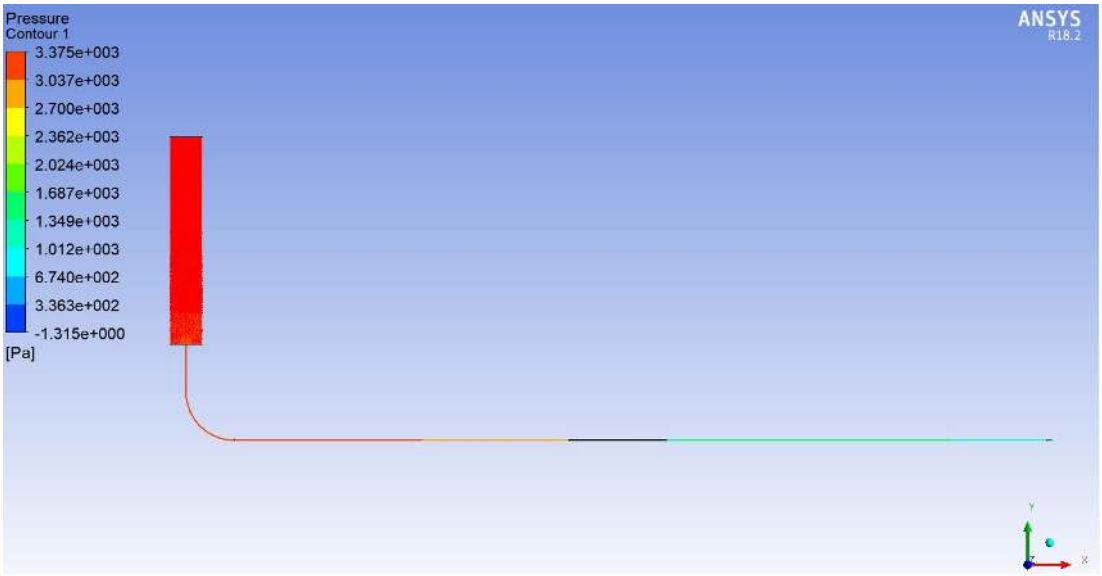

Figure E.6 Pressure drop of experimental setup at 10 mmHg.

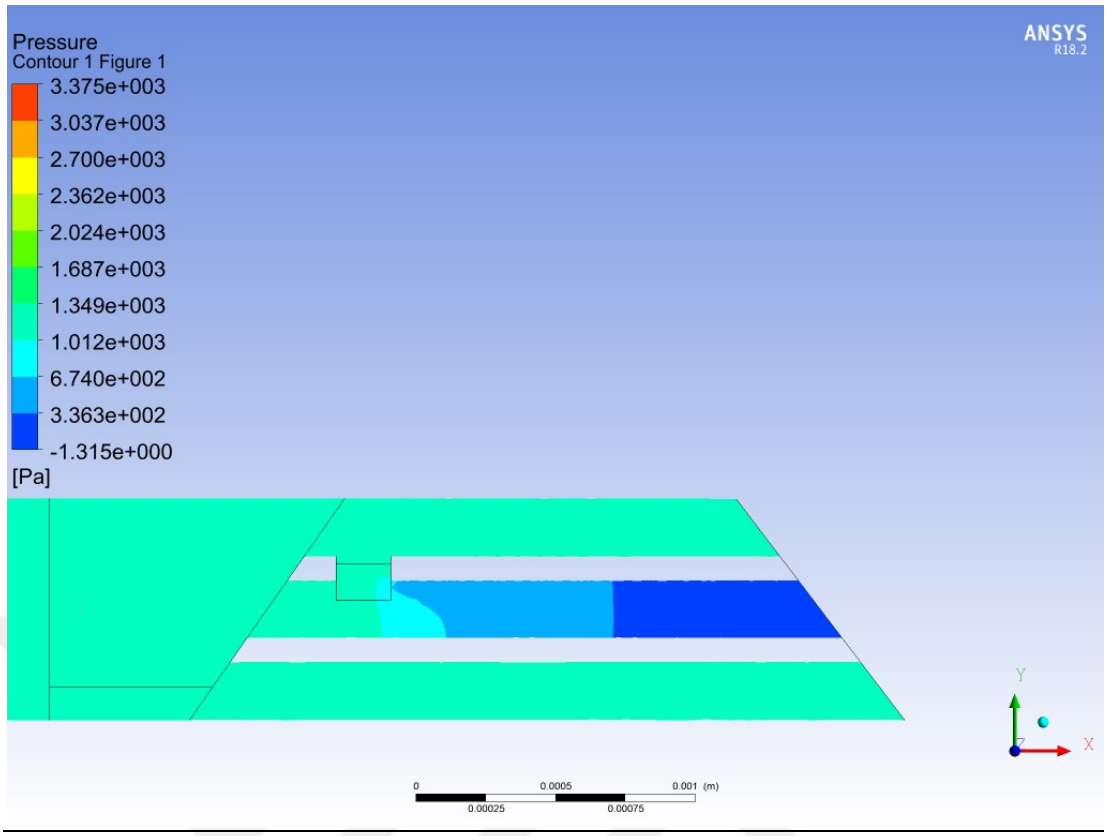

Figure E.7 Pressure drop of ExPress implant at 10 mmHg.

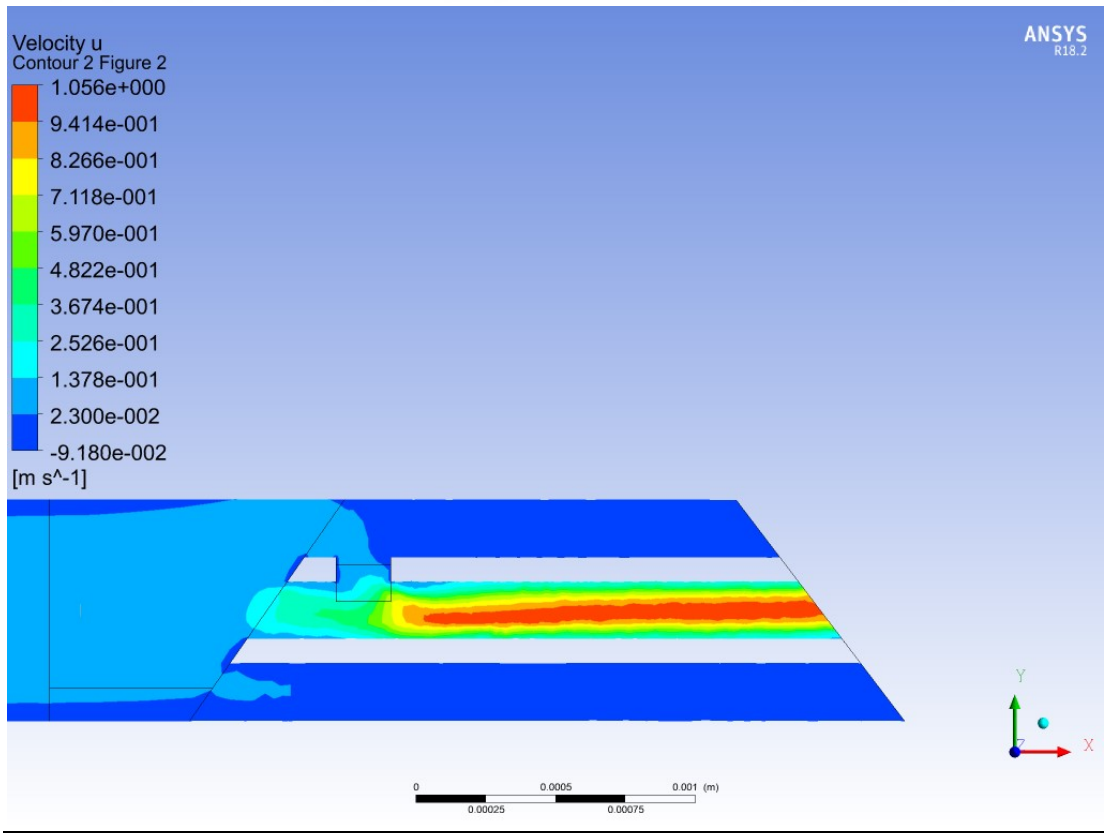

Figure E.8 Velocity contours of ExPress implant at 10 mmHg.

15 mmHg

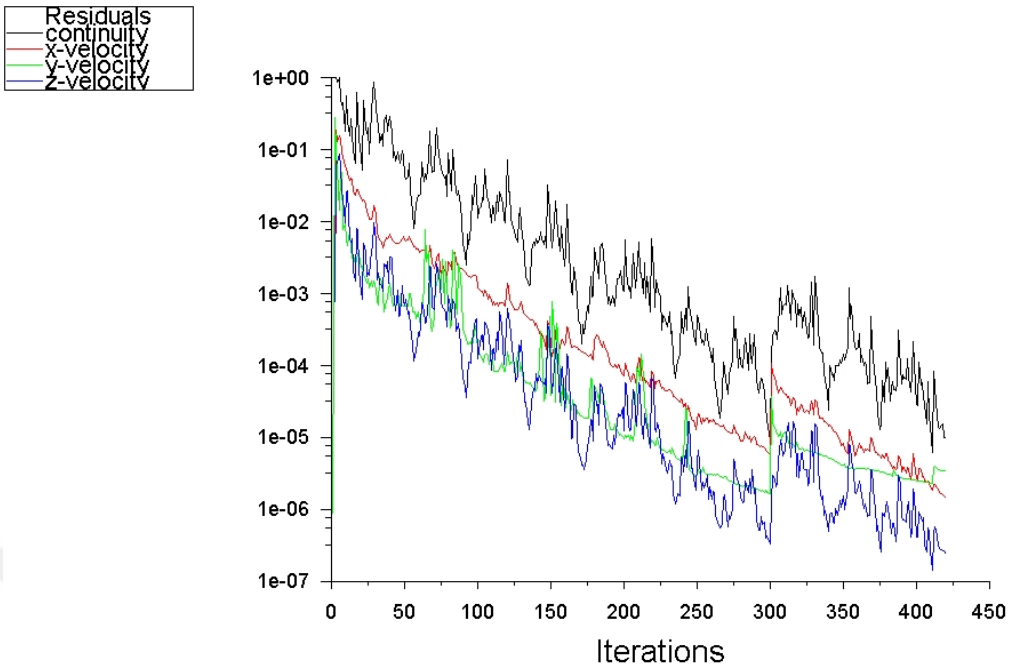

Figure E.9 Convergence results of ExPress implant at 15 mmHg.

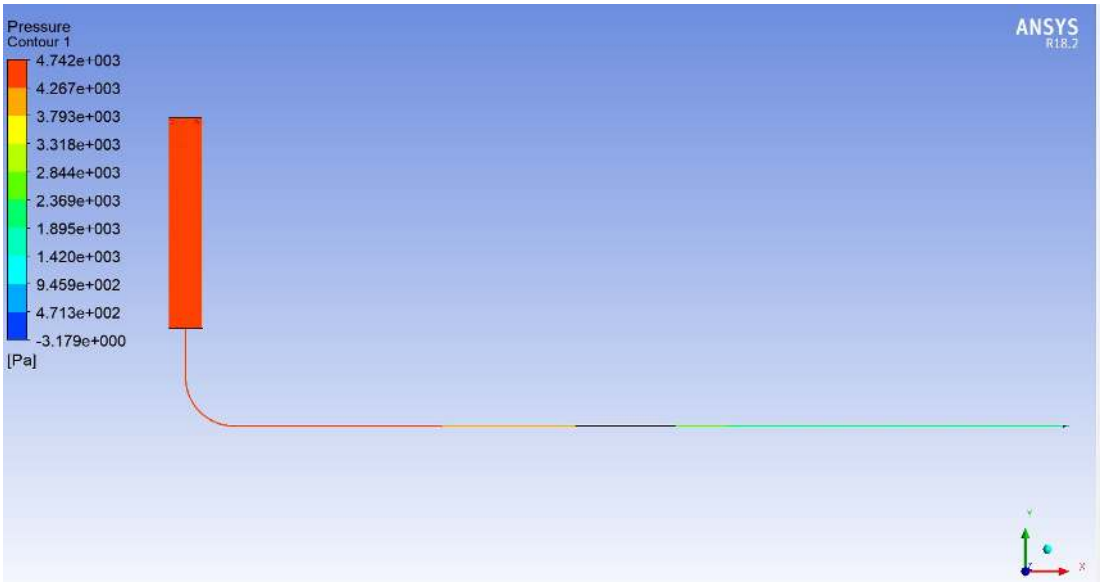

Figure E.10 Pressure drop of experimental setup at 15 mmHg.

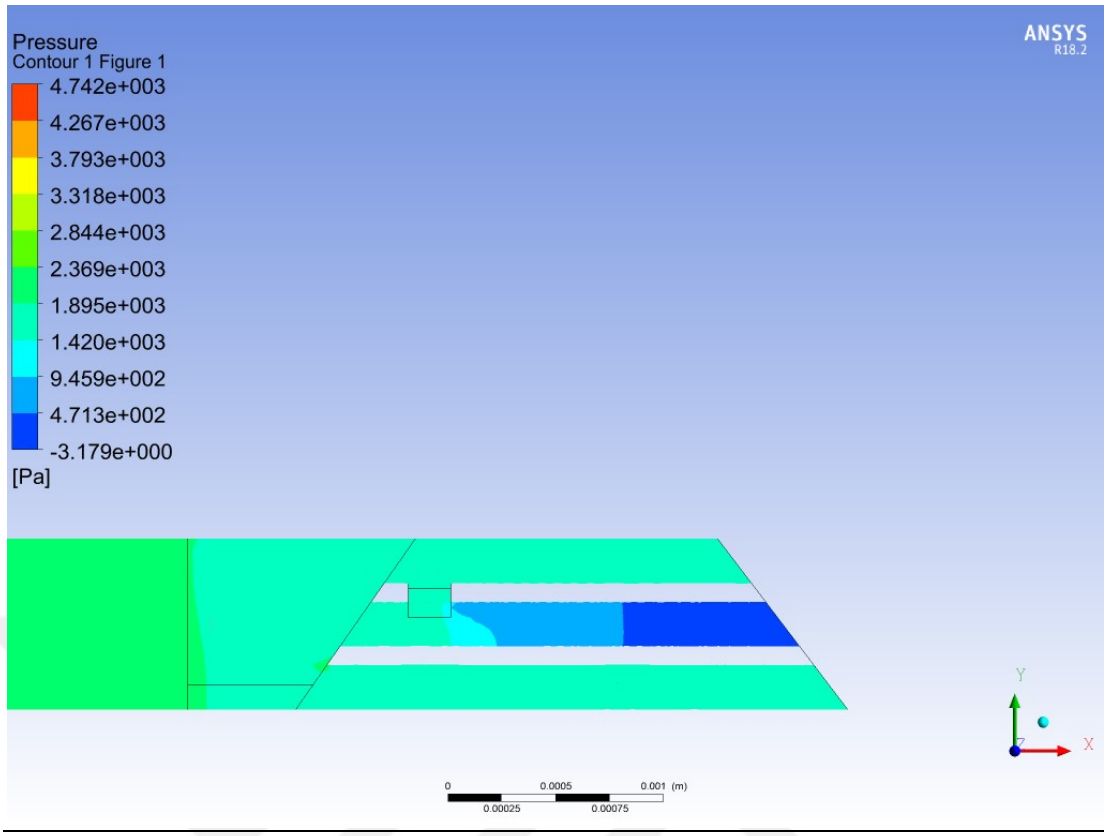

Figure E.11 Pressure drop of ExPress implant at 15 mmHg.

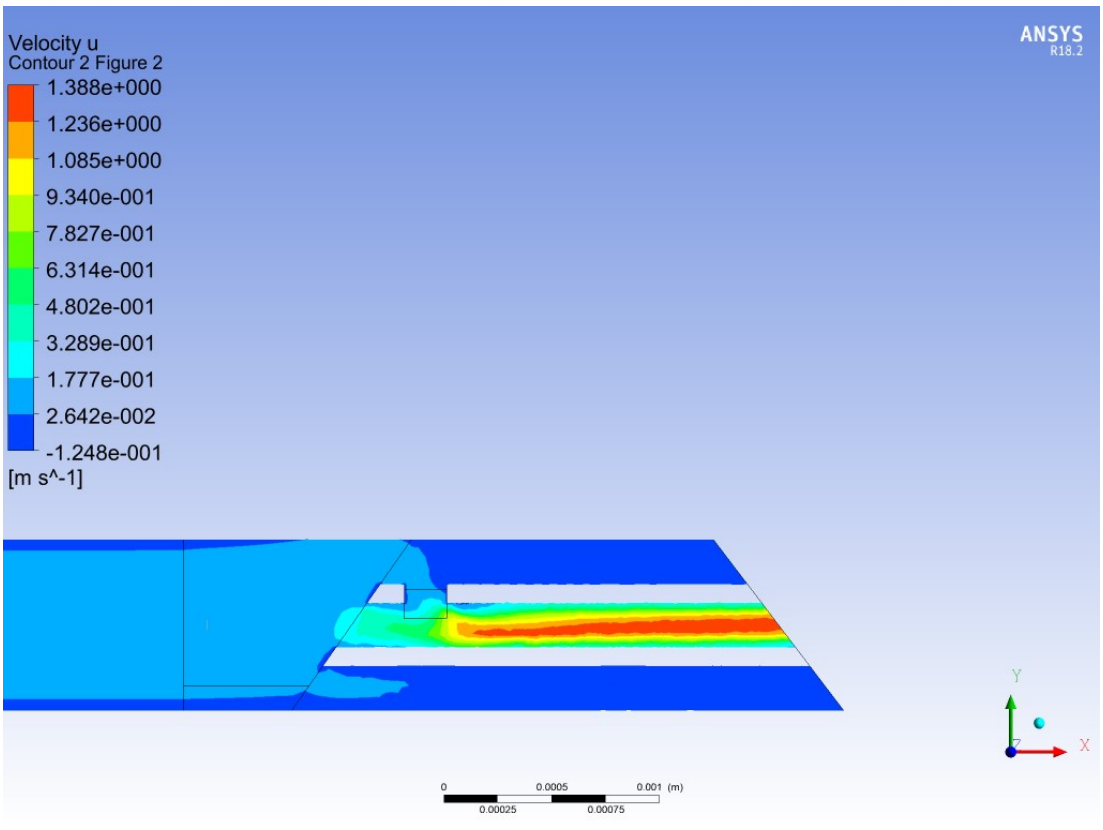

Figure E.12 Velocity contours of ExPress implant at 15 mmHg.

20 mmHg

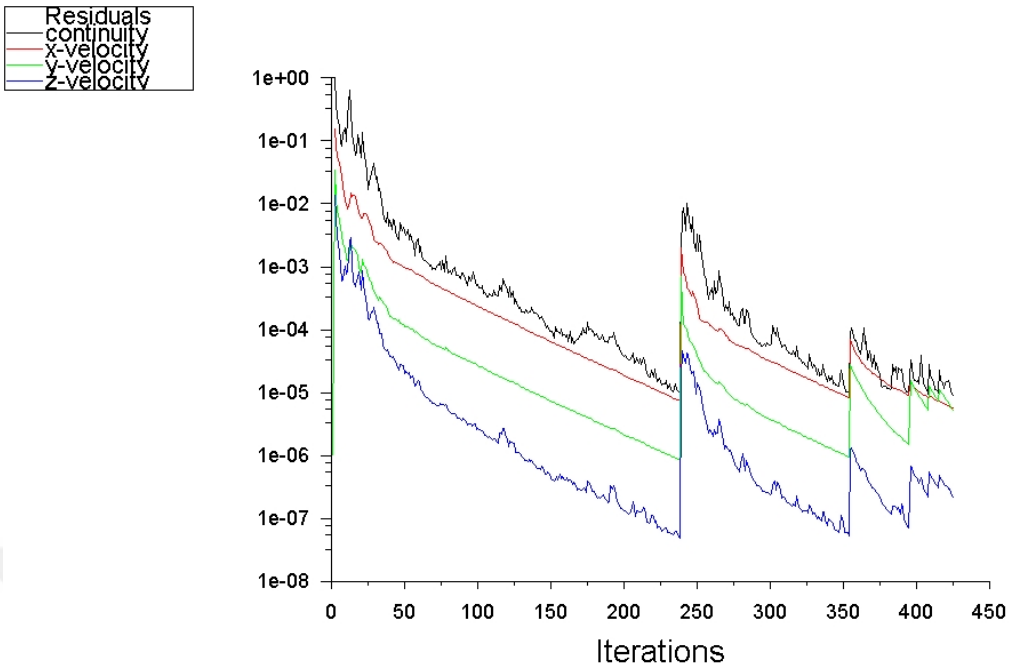

Figure E.13 Convergence results of ExPress implant at 20 mmHg.

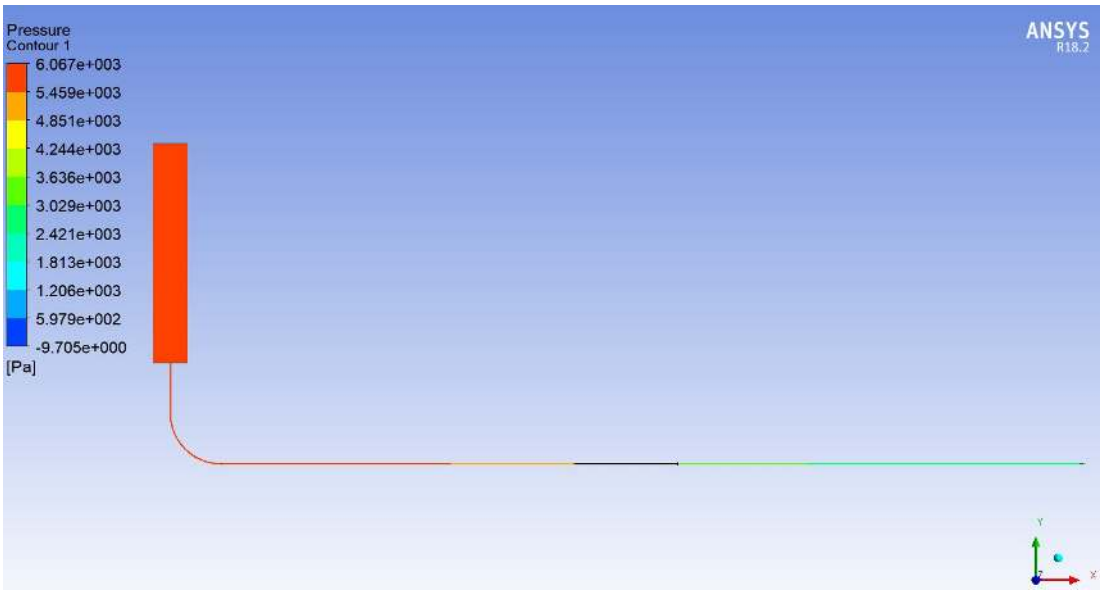

Figure E.14 Pressure drop of experimental setup at 20 mmHg.

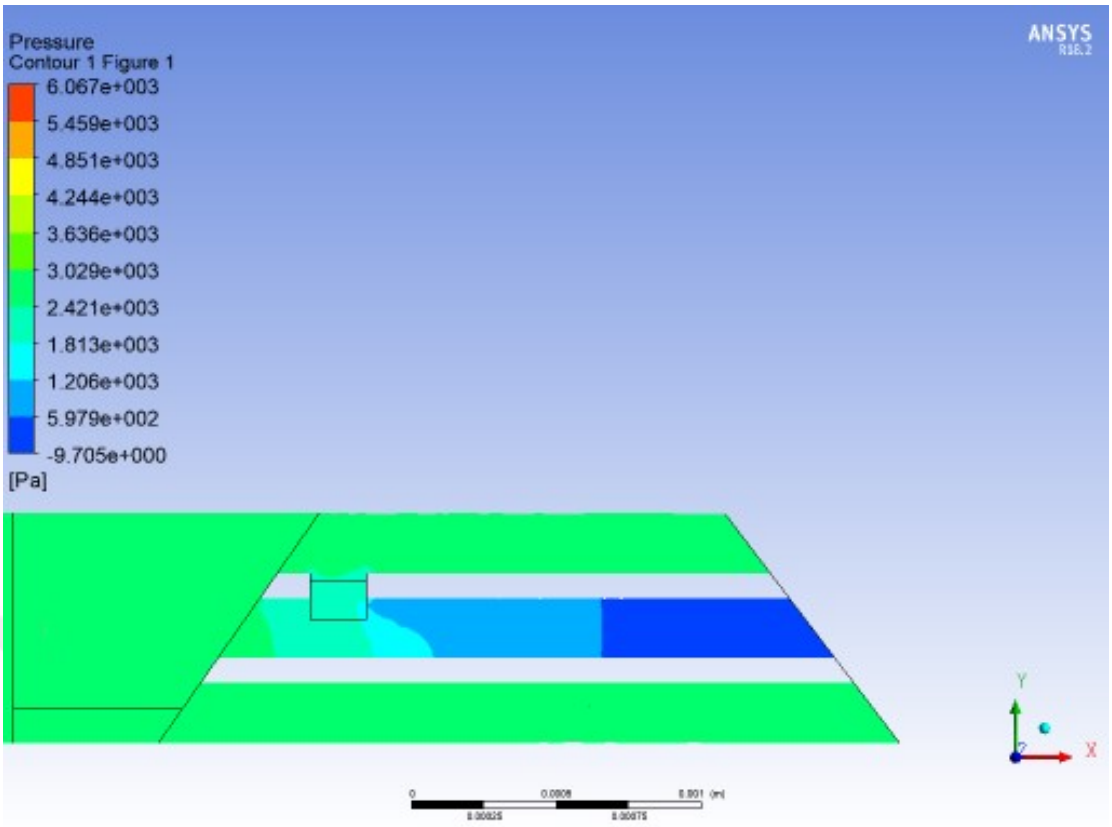

Figure E.15 Pressure drop of ExPress implant at 20 mmHg.

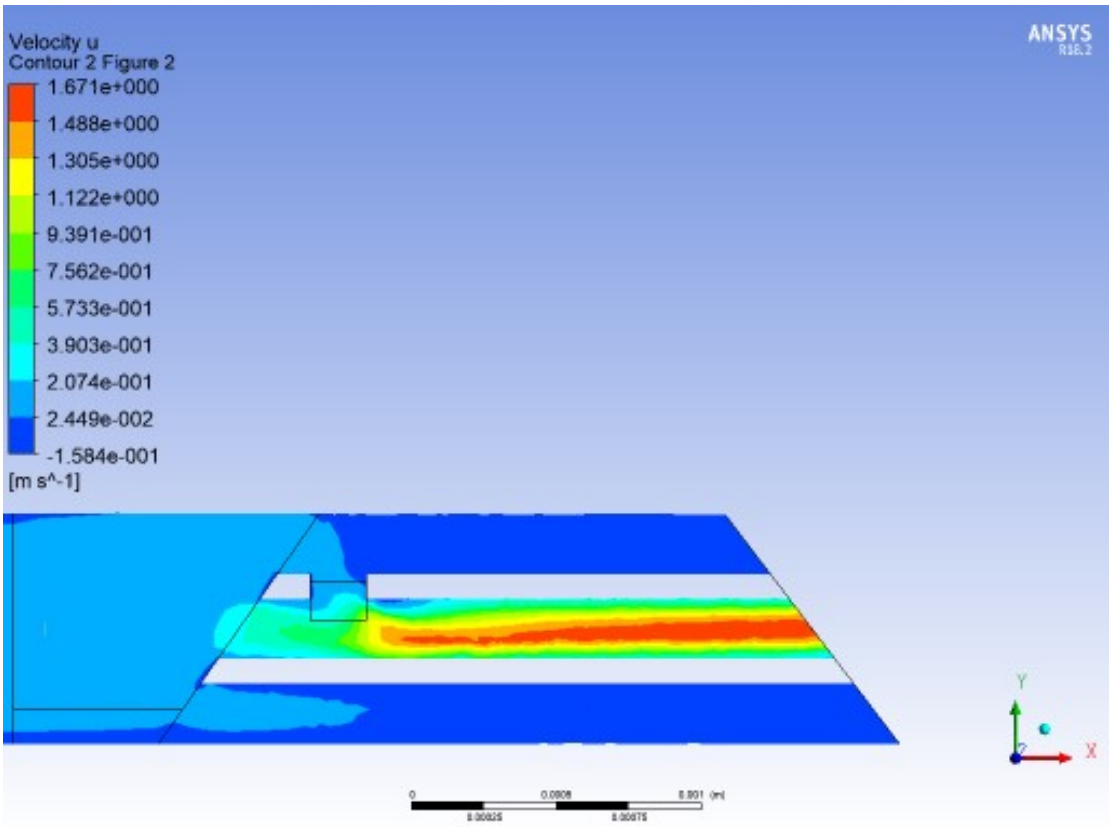

Figure E.16 Velocity contours of ExPress implant at 20 mmHg.

25 mmHg

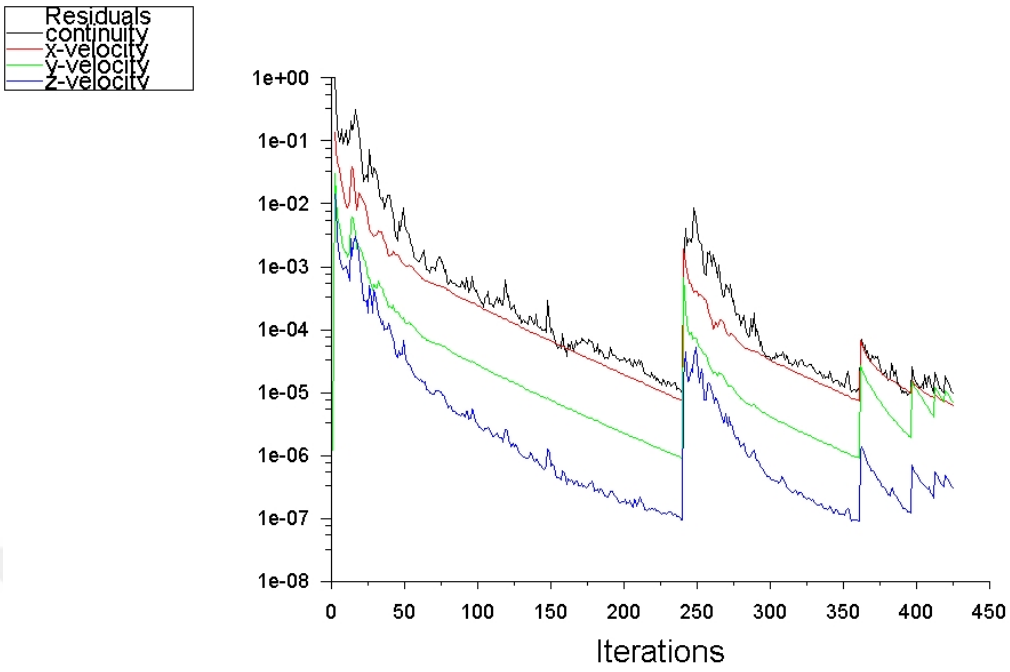

Figure E.17 Convergence results of ExPress implant at 25 mmHg**.**

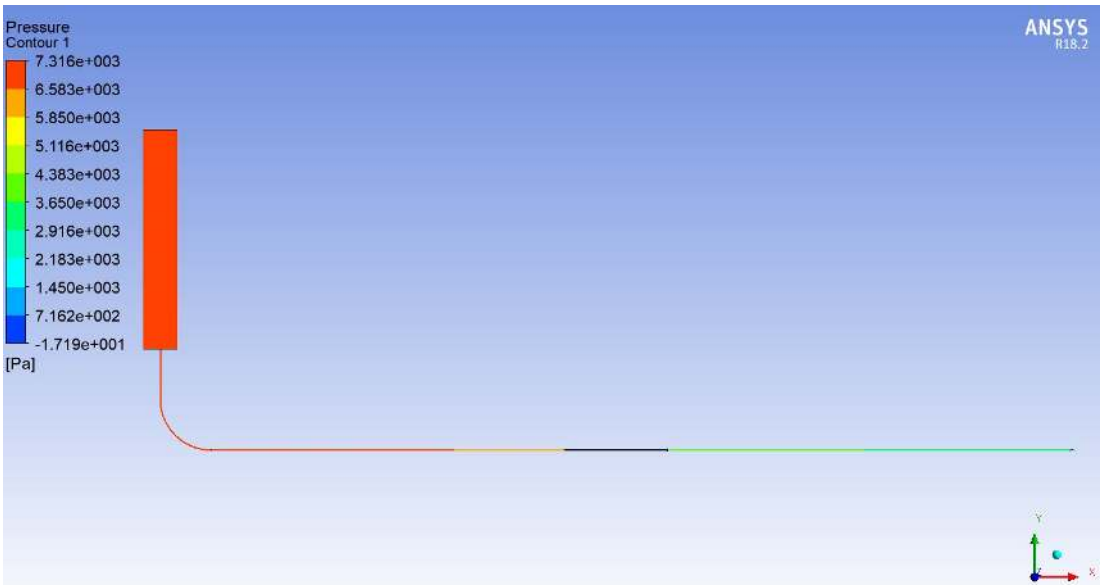

Figure E.18 Pressure drop of experimental setup at 25 mmHg.

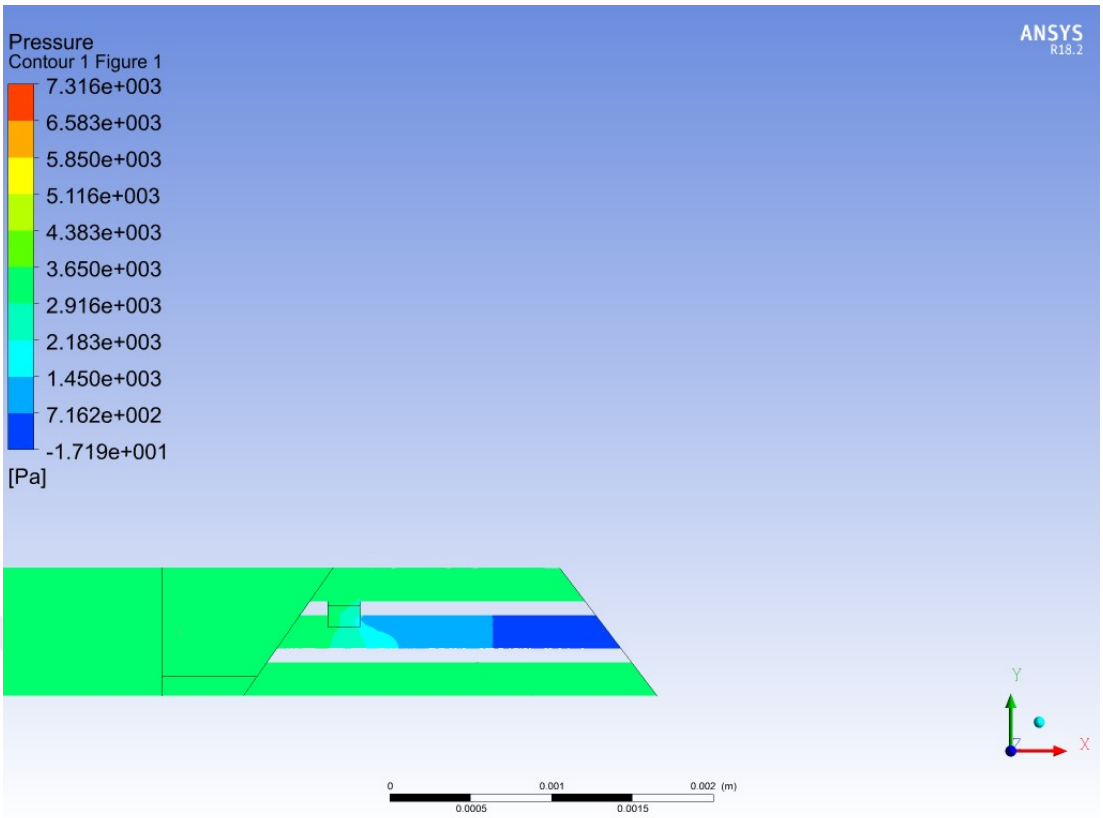

Figure E.19 Pressure drop of ExPress implant at 25 mmHg.

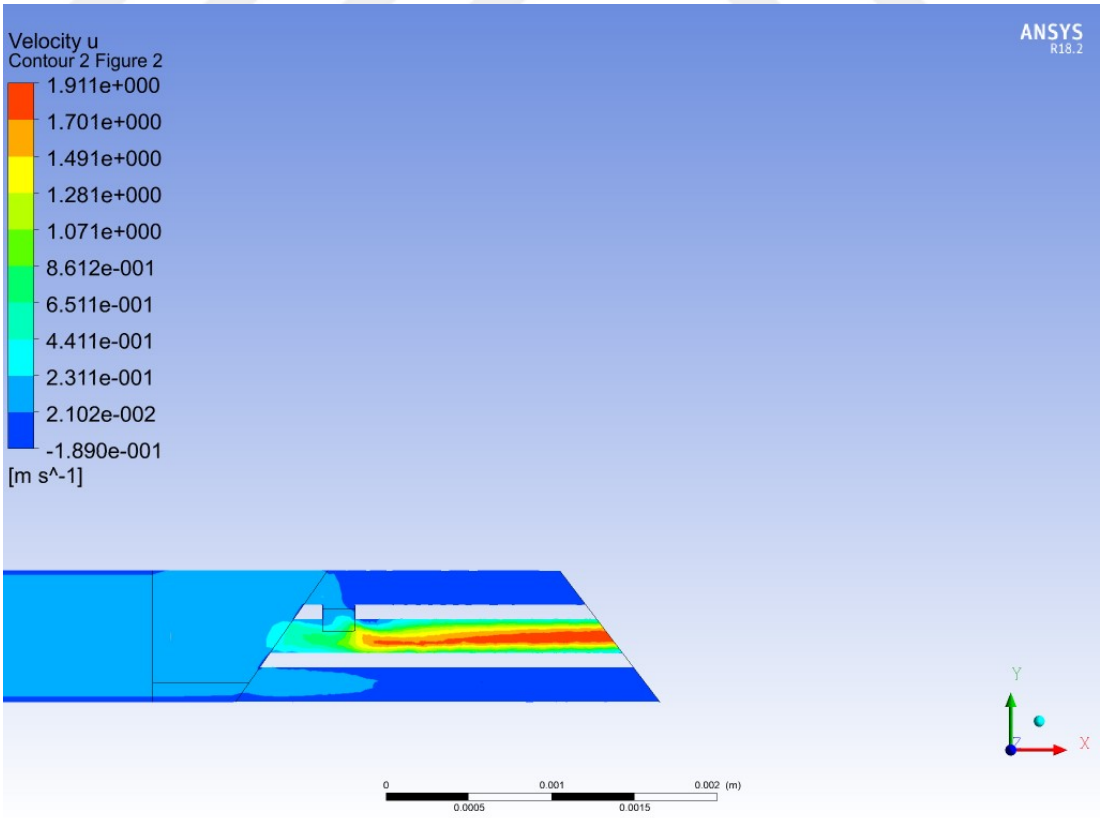

Figure E.20 Velocity contours of ExPress implant at 25 mmHg.